Numerical Strategy for Uncertainty Quantification in Low Enthalpy Geothermal Projects

By

Sannidi Nagaraj Shetty
Student ID: 4511883

in partial fulfilment of the requirements for the degree of

Master of Science
in Applied Earth Sciences
at the Delft University of Technology,
to be defended publicly on Monday November 27, 2017 at 16:00 PM.

Supervisor	Dr. Denis Voskov	TU Delft
Co-supervisor	Prof. David Bruhn	TU Delft
Thesis committee	Prof. David Bruhn	TU Delft
	Dr. Denis Voskov	TU Delft
	Dr. Joep Storms	TU Delft

TUDelft

Author

Sannidi Nagaraj Shetty   MSc Student, Petroleum Engineering & Geosciences
s.n.shetty@student.tudelft.nl   Department of Geosciences and Engineering
                                      Delft University of Technology

Title

Numerical Strategy for Uncertainty Quantification in Low Enthalpy Geothermal Projects

Advisor

Dr. Denis Vaskov   Associate Professor
D.V.Voskov@tudelft.nl   Department of Geosciences and Engineering
                                     Delft University of Technology

Co-advisor

Prof. David Bruhn   Part-time Professor of Geothermal Engineering
D.F.Bruhn@tudelft.nl   Department of Geosciences and Engineering
                                     Delft University of Technology

Committee Member

Dr. Joep Storms   Associate Professor
JEAStorms@tudelft.nl   Department of Geosciences and Engineering
                                     Delft University of Technology

An electronic version of this thesis is available at http://repository.tudelft.nl/.

Abstract

In the recent years, geothermal technology has received substantial attention as an alternative source of energy. However, the lack of detailed information about subsurface formations of interest often introduces significant uncertainties to the technological and economic planning of geothermal projects. As the result, some important technological parameters, affecting geothermal projects, cannot be predicted with enough certainty. One of the most important technological characteristics in low enthalpy geothermal projects is the time when cold fluid from the injection well breaks into the production well. The large variation in thermal breakthrough time against the exact location of the well doublet was identified. These variations can largely impact the lifetime of the low enthalpy geothermal project, thereby affecting the quantification of the projects economy.

In our study, we investigate the main factors responsible for the variation of breakthrough time by performing a sensitivity analysis of different hydraulic and thermal properties. A geometry/rule-based modeling software Flumy was used to generate a detailed fluvial facies distributed, similar to that observed in the West Netherlands Basin (Nieuwerkerk Formation). The models were then populated with various thermal and hydraulic properties, correlated with the facies map. Ensembles of models were run in ADGPRS (Automatic-Differentiation General Purpose Research Simulator) to perform a sensitivity analysis.

For a given technological characteristics (distance between doublet wells, injection and production rates, drainage area etc.), a difference of approximately 50% was observed in the lifetime of the project while relocating the doublets positions and keeping the same distance between the doublet pair. The major numerical and geological factors, contributing to the difference in breakthrough time, were identified in our study. In addition, the best simulation strategy and numerical parameters for uncertainty quantification in low enthalpy geothermal projects were suggested.

Acknowledgements

Table of Contents

Table of Contents

Table of Figures

Table of Figures

List of Tables

Nomenclature

Absolute Permeability	K
Accumulation	A
Darcy/superficial velocity	u
Depth	z
Enthalpy	H
Flow transmissibility	Γ_f
Gravitational constant	g
Internal energy	U
Mass density	ρ
Phase fraction of component	x
Porosity	φ
Pressure	p
Relative permeability	K_r
Residual	R
Saturation	S
Slope	m
Source / Sink flux	Q
Temperature	T
Thermal Conductivity	κ
Thermal transmissibility	Γ_c
Time	t
Viscosity	μ

Nomenclature

Subscript

Cell notation	(i, j)
Component/Phase	c/p
Rock	r
Phase	p
Water	w
Integral length	l

1

Introduction

This chapter briefly describes geothermal energy, its types, and requirements. Furthermore, it covers the description of thermal breakthrough time. It is then followed by research goal which includes the problem statement and previous related works. A brief introduction to the proposed solution is also done. The chapter concludes by introducing subsequent sections of the paper.

Based on Geothermal Energy Association (GEA), only 6.5 percent of the total global potential has been exploited so far. With geothermal energy production being one of the most minimal types of CO_2 generating energy sources, its growth and worldwide utilization play a significant role in reducing the worldwide CO_2 emission (1).In the recent years, geothermal energy has gotten significant consideration as an alternative source of energy. The type of application of the energy sources is dependent on the temperature of the formation water.

In the broad sense, geothermal energy is a type of energy contained in the form of heat inside the earth. A heat source such as the magma body in volcanic regions or the average temperature gradient of 30˚C/km in non-volcanic regions, heat the fluids in the subsurface. This hot water or steam is usually trapped in a porous formation having good permeability. The trapping of these fluids usually occurs due to the presence of an impermeable membrane above it. Throughout this paper, the formations where the hot fluids are trapped are termed as geothermal reservoirs or aquifers and the impermeable membrane above will be referred to as cap rocks.

Types of geothermal systems

 Based on the temperature ranges, geothermal systems can be classified as follows:

1. Low enthalpy systems (below 120˚C or 393.15 K)
2. High enthalpy systems (above 120˚C or 393.15 K)
3. Hot dry rock systems (which requires external circulation and production of heated fluid)

Low enthalpy systems are candidates for direct application and the fluid exists as a liquid in the reservoir. In low-temperature systems, the reservoir fluid is constantly brine, while in higher-temperature systems, steam can likewise be available. All geothermal reservoirs located to date can be divided into two types: liquid dominated and vapor-dominated depending on whether liquid or steam is the mobile phase. (2)

The reservoir models generated for our study have an initial temperature of 75˚C (348.15K), which makes it fall under the low-enthalpy geothermal resources. The well-known application of these resources is space heating. (3)

Introduction

Requirements for exploiting geothermal resources

There are four main requirements for geothermal resources to be exploitable
a. A heat source
b. Fluid which acts as a carrier of heat
c. The permeable bed which will transmit and enable the production of the hot fluid through wellbores.
d. Caprock which will confine the fluid convection in the reservoir.

Under actual circumstances, the mix of every one of these prerequisites isn't direct. The lack of information about the subsurface introduces the most significant uncertainties in the quantification of the economy for a particular project. The geological uncertainties and their effects on production have been studied extensively for oil and gas but to a lesser extent for geothermal exploitation. The success of a geothermal project strongly depends on an accurate estimation of all risks and uncertainties of the process.

Thermal Breakthrough Time and Lifetime

A geothermal reservoir is exploited with the help of well doublets. Doublet refers to a pair of wells drilled into the reservoir, where one of the wells serve as a production well while the other is used as an injection well. (In *Figure 1.1* A, B, C and D the injection well is represented with a blue dot while the production well with a red dot). With the aid of producers, hot water (348.15 K) is extracted from the reservoir for various applications like heating. Once all the heat from the water has been exploited, the temperature of the water drops. As water reaches a temperature of 308.15 K, it needs to be re-injected into the reservoir with the help of injectors. This is done because the cold water (308.15) can serve as an additional recharge to supplement natural recharge and to reduce the pressure decline. The other advantages of reinjection are to counteract surface subsidence and potentially associated seismicity. Reinjection will, therefore, in most cases increase the production capacity of geothermal reservoirs, which counteracts the inevitable increase in investment and operation costs associated with reinjection (4). As seen in *Figure 1.1*, during Injection, the cold water front propagates through the reservoir and reaches the production wells. Once the cold waterfront reaches the production wells the temperature of the produced water begins to decline. The time at which the cold waterfront reaches the production well and causes a decline in the temperature of the produced water is referred to as the thermal breakthrough (BT) time. In *Figure 1.1* E, the reservoir is observed to have a thermal breakthrough after 20 years. Please note that Figure 1E also indicates the lifetime of the reservoir at 340K. This is because the production of water at temperatures below 340K is not economically viable and hence all results and sensitive study were done only for the reservoirs lifetime. Please note that the temperature ranges mentioned above are illustrations of the values used in our case study and can vary in real life depending on use.
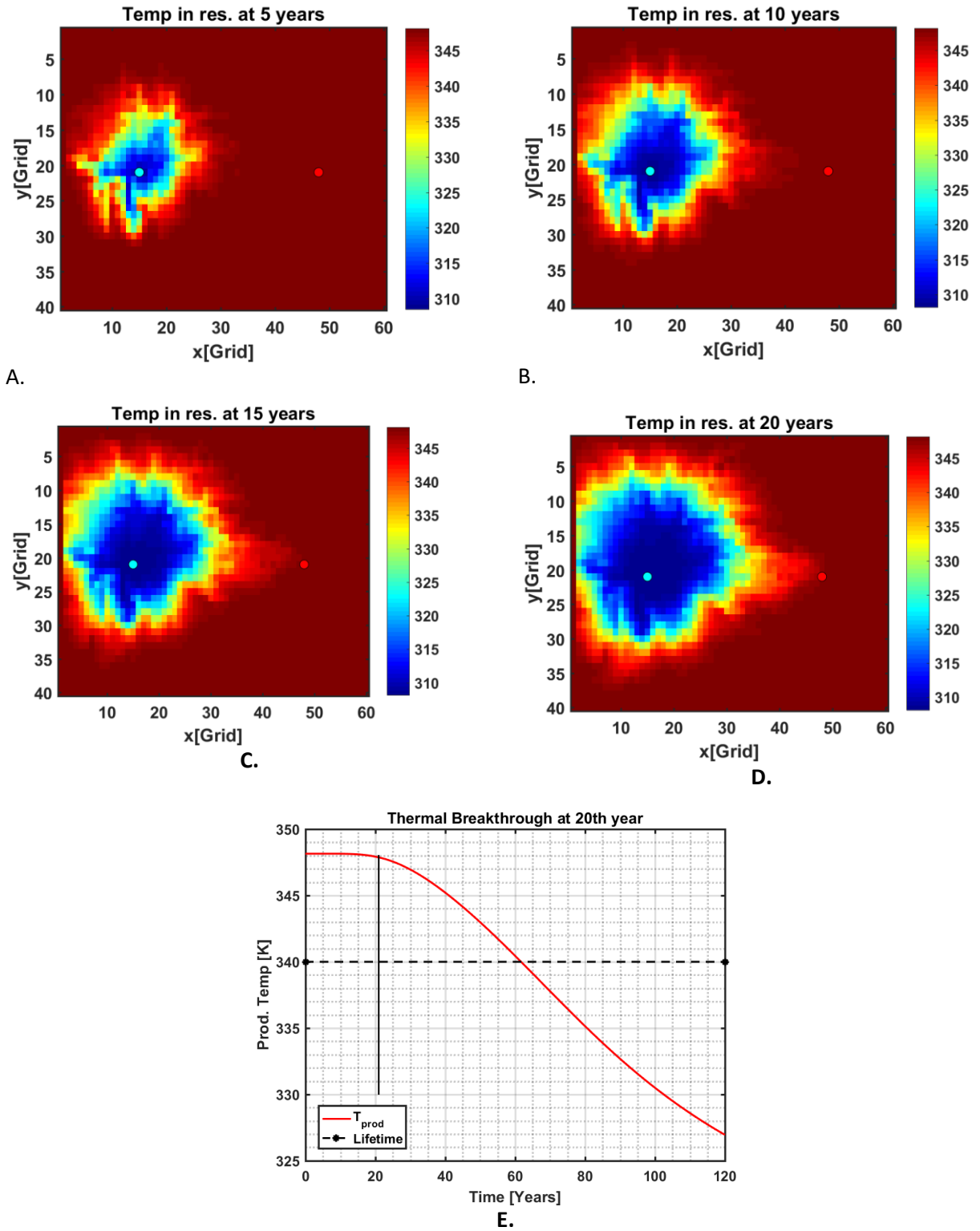
Figure 1.1: *A, B, C, D indicates the cold water plume over time from the injection well (cyan) to production well (red). In D it's evident that the cold water reaches the production well after which the temperature of the produced water will begin to decline. E. represents the corresponding breakthrough curve over 120 years.*

Introduction

Problem Statement

One of the major uncertainties in a geothermal project is the lifetime of the geothermal reservoir. The lifetime can be identified using the thermal breakthrough curves. Effects in the lifetime of the reservoir by placing the doublets parallel or perpendicular to the paleoflow direction of fluvial sandstone and their effect on pump energy losses have been studied by Cees Williams (5). It was observed that the lifetime of the aquifer was less when the doublets were placed perpendicular to the paleoflow than when they were placed parallel. In addition, pump energy losses were reduced to 10% if the doublet wells were placed parallel to the paleoflow trend (5). A lifetime of the reservoir can be sensitive to numerous factors. Several studies investigating factors influencing heat flow in geothermal reservoirs and their lifetime have been carried out. These include viscosity and density dependence on temperature (6; 7; 3), porosity and permeability (8; 9; 10), geothermal fluid salinity (11), flow rate (12), well spacing (13), injection temperature (14) and reservoir geometry (15). But these variations haven't been tested on the influence of the spread between breakthrough curves obtained by changing the location of the doublets. A detailed explanation of spread in breakthrough curves can be found in chapter *3* under the section *3.4*.

In our work, we observed that the lifetime of the reservoir varied hugely just by relocating the doublets from their original grid location to the surrounding grids few tens of meters away. A difference of 25-35 years was observed when the doublets were placed at the neighboring locations. It's is important to accurately evaluate the reason for such huge variations since they help us to predict the doublet performance. These predictions along with the high initial investment costs and low financial gain play a crucial role in deciding if an investment can be made on the project.

Research Goals

The primary objective of this paper is to address the main reason for the variations in the thermal breakthrough curves. To do so the research seeks to address the following questions:

- Which thermal and hydraulic properties contribute the most to the variation in thermal breakthrough?
- Can numerical scale of the model affect the breakthrough time?
- What kind of geological characteristics affect the breakthrough time?
- What is the best suitable numerical strategy for the model?

Proposed Strategy

In order to obtain breakthrough plots, the very first requirement is the regional geological model that describes the spatial distribution of a fluvial system. Delft Sandstone Member (DSSM) in the Lower Cretaceous Nieuwerkerk Formation present in the West Netherlands Basin (WNB) has been used as a case study. To obtain the breakthrough curves, a model was created using Flumy. Flumy helps to replicate the depositional heterogeneity which is the result of the sand-body continuity combined with the permeability trends within the sand body. It uses a combination of stochastic and geometry-based approach.

This model has been populated with reservoir parameters using a beta distribution in Matlab. In order to perform numerical simulations and modeling of geothermal reservoirs, ADGPRS (Automatic-Differentiation General Purpose Research Simulator) was used. It is a reservoir modeling platform developed and sustained by the SUPRI-B research group in the Energy Resources Engineering Department at Stanford University (16). Previous studies on geothermal reservoir simulations were performed in COMSOL (17; 3; 5). To verify the implementation, a comparison study was conducted using test cases that were performed on COMSOL, in ADGPRS by Khait and Voskov (18). It was observed that the results obtained from ADGPRS validate that of COMSOL using the same set of the input parameter. In addition, ADGPRS served to be more efficient in terms of the time taken to run simulation.

To reduce uncertainties in parameter estimation, a sensitivity study of various parameters (such as porosity, permeability, heat conduction, heat capacity) was performed on the generated model. In addition, the effect of over and under burden layers and the thickness of the reservoir were looked at. They were then followed by identifying the well performance and investigation of flow paths using streamlines. Subsequently, the connectivity analysis and thermal recharge gained limelight. Finally, several upscaling strategies were implemented to compare results between fine and coarse models.

Thesis Outline

The overall structure of the study takes the form of eight chapters, including this introductory chapter.

Chapter 2 begins by laying out the regional geology of the WNB and concludes by mentioning the employed model parameters used based on the available literature.

The *3rd Chapter* is concerned with the modeling approach used for this study. An explanation for the choice of overburden and under burden has also been established. Furthermore, the idea of well placements and the spread in the breakthrough curves are explained.

The *4th section* covers the mathematical and numerical formulations involved in governing equation and an explanation of how streamlines are calculated in a Cartesian system

Chapter 5 presents the findings of the research and focusing mainly on the sensitivities of individual parameter alongside well performance and streamlines

The *6th chapter* aims to provide an understanding of the concept of connectivity and thermal recharge

Chapter 7 analyses the results of various upscaling strategies and provides a brief discussion

Chapter 8, being the final chapter gives a brief summary and discusses the findings.

<div align="right">

2

</div>

Literature Review

2.1   West Netherlands Basin (WNB)

The West Netherlands Basin (WNB) is a 60-km-wide basin in the southwest of the Netherlands (19) *(Figure 2.1).* WNB stands as an example for a promising aquifer region in the Netherlands. The knowledge of the aquifers in the WNB was obtained from the hydrocarbon exploitations carried out between 1950-1990's (20). Sandstone-rich fluvial successions of the Nieuwerkerk Formation are the main targets for heat exploitation in the WNB. Nine geothermal wells have been drilled until 2016 for direct use applications. And approximately two doublets are released each year. Furthermore, WNB also accounts for 70% of all doublets in the Netherlands. Currently, the main target for Delft Aardwarmte Project (DAP), is the fluvial Delft Sandstone Member (DSSM), part of the Lower Cretaceous Nieuwerkerk Formation (21; 22). Out of the nine doublet pairs, five of them in the WNB also target this sandstone member (23). DAP aims to use DSSM for the extraction of geothermal energy in order to generate sustainable natural heating for TU Delft campus. DAP targets to drill a geothermal doublet in the TU Delft premises with an aim to obtain a reasonable lifetime of 30 years. In addition, DSSM is the main reservoir layer in the Moerkapelle field, located 12 km northeast of Delft, which serves as an additional advantage in obtaining a good understanding of DSSM (22).

2.2   Regional Geology of Nieuwerkerk Formation

The formations were formed during the Late Jurrasic until the Early Cretaceous (*Figure 2.2*) and were characterized as syn-rift and post-rift fluvial units. The Nieuwerkerk Formation consists almost entirely of fluvial, non-marine sediments deposited by rivers flowing northwestward along the basin axis. Numerous pieces of evidence corroborated the fluvial origin of the formation; one such example was from core samples that showed a large number of stacked, fining-upward channels overlaid by flood-plain silts and ponds. (24; 25) But due to strong tectonic deformations and a large degree of facies heterogeneity, understanding the reservoir and seal distribution has always been an issue (25) .

The subdivision of Nieuwerkerk Formation is based on two hypotheses. The first hypothesis suggests that Delft Sandstone is a continuous stacked channel deposit, occurring throughout most of the WNB. (26) . The second hypothesis states that the Delft Sandstone is not a separate member due to stacked channel complexities occurring throughout (24). The Doublet systems in the WNB detected DSSM to have reservoir thicknesses of 150m and were amongst the deepest reservoir (hence warmest) at depth intervals of 2-3km in the WNB, which makes it an important reservoir (20).
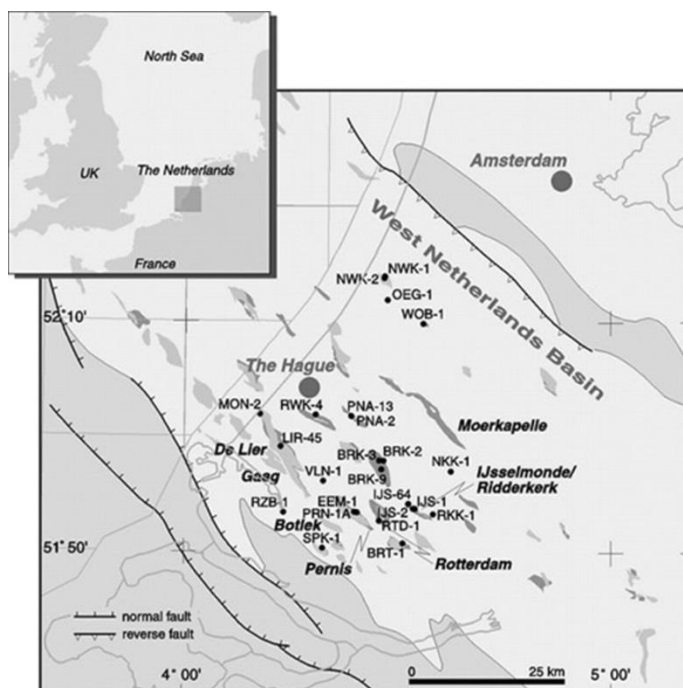
Figure 2.1: Location of the West Netherlands Basin in southwestern Netherlands from Devault and Jeremiah (2002) Ref: (24)
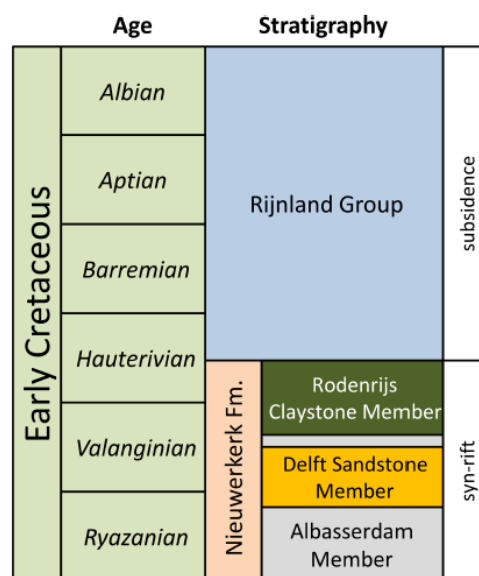
Figure 2.2: Stratigraphic Column for the Early(Lower) Cretaceous section in WNB from Ref (27)

The sequence stratigraphic framework in the Nieuwerkerk Formation aquifers has been studied extensively by Cees Williams and is explained in detail in his work (27). Based on his findings using core descriptions and gamma-ray logs, complemented with palynological data sets, we could infer that the fluvial interval was subdivided in a Late Ryazanian to Early Valanginian succession and a Valanginian succession (***Figure 2.2***). The study helped to reduce the uncertainty of the fluvial aquifer exploitation.

2.3   Geological Data Set

A recent review of the literature on "*regional geology and geothermal potential of the delft sandstone member*" showed that the top of Delft Sandstone member (DSSM) was present at a depth of 2000-2300m.This was obtained with the help of a contour map derived from 3D seismic (19). Bottom-hole temperature readings from oil and gas wells in the region indicate that the geothermal gradient is approximately 3°C/100m (19). In the current doublets, 65-75˚C (338.15 -348.15 K) formation water is produced and 30-40˚C (303.15 -313.15 K) water is re-injected. The doublets were placed 1-2 km apart to obtain a lifetime of at least 30 years and prevent the risk of having an early cold water breakthrough (19). With an aim to maintain pressure support in the reservoir, the doublets targeted the same reservoir. Therefore, it is essential to have an understanding of the reservoir connectivity between the production and the injection well in the reservoir. The flow rates in these doublets were at a range of 100-200 m^3/hr (21).Based on core studies, approximately 75m of the core in MKP-11 and 25m of the core in Q13-09, five different facies were recognized namely floodplain fines, crevasse splays, single-storey channel bodies and amalgamated sandstone complexes (5) The thickness (depth) of individual sandstone bodies is approximately 4m. The point bar grows through lateral accretion and is characterized by a fining upward sequence. Based on the

maximum fining upward sequence, an estimate on the height of each channel deposition could be made. This was then related to the maximum height of the other channels. Using this information the thickness (depth) of individual sandstone bodies was observed to be approximately 4m. Based on the bank flow depth, the bank flow width was estimated at 40m (5). Crevasse splay thickness in the cores ranged between 0.2-0.6m.The gamma rays provided a range of net to gross ranging from 15% to 85% (5) In addition, porosity-permeability relationship were also obtained from the core data which was used during the reservoir property modeling mentioned in section **3.2**.

2.4   Model Parameters

Taking into account all the information from the literature review, several reservoir models were generated with varying N/G (net to gross ratio) ranging between 15%-85%. The reservoir model is located at 2300m depth with an initial temperature of 348.15K (75°C) and initial pressure of 200 bars. The distance between the doublets is 990m. Both the injection and production rate are specified at 200m^3/hr (4800m^3/day) to avoid the pressure decline in the reservoir. The injected water has a temperature of 308.15K (35°C). Although the DSSM has highly faulted structures, in order to reduce the complexity of the problem, the model does not include faults. Further details of the model parameters will be explained in the upcoming section. The inclusion of faults and fracture is out of the scope of this research but should be considered in future research.

Model Parameters	Value	Units
Reservoir Depth	2300	m
Initial Temperature of the reservoir	348.15	K
Initial pressure of the reservoir	200	Bar
Temperature of the water injected	308.15	K
Rate of water injection	4800	m^3/day
Rate of water production	4800	m^3/day
N/G variation range	15-85	%

Table 2-1: Model parameters based on the geological dataset

3

Modelling Approach

3.1   Geological / Static Modelling

The very first goal of this work was to create a geological model that describes the facies distribution which could then be used for flow simulations. The modeling technique is similar to the one used by Cees Williams, which is based on the subsurface dataset of the fluvial Nieuwerkerk Formation of the WNB (21). In general, facies modeling approach has an effect on connectivity analysis as it impacts both spatial distributions and the shape of the sand bodies (28). Here, the facies realizations were generated by geometry-based modeling software, Flumy. It is different from the object based and process-based model in the sense that it follows a set of behavioral rules (heuristic formulas) based on the input parameters which are entered into the software. These behavioral rules work together to give a consistent representation of the meandering fluvial system. In object-based modeling, the spatial distribution of the facies is more random (5). They rely on qualitative knowledge and hence results are subjective (29).In a process-based model, the underlying physics is taken into consideration and the model operates by itself. However a process-based model would take a much longer time to generate similar realizations and hence, due to time constraints, Flumy was considered to be a reasonable approach to obtain the static model.

Geological modeling of a fluvial reservoir is intricate as it comprises heterogeneity in sediment bodies. Fluvial reservoirs primarily comprise of impermeable floodplains and permeable sandstone bodies (21). In order to obtain a realistic geological model, geometry-based modeling software, Flumy was used. As it mirrors sedimentary processes this technique produces numerical blocks that are geologically consistent and realistic (30). Various fluvial deposits, such as point bars, crevasse splays, overbank alluvium, sand and mud plug are generated in the model as shown in *Figure 3.1* (30).
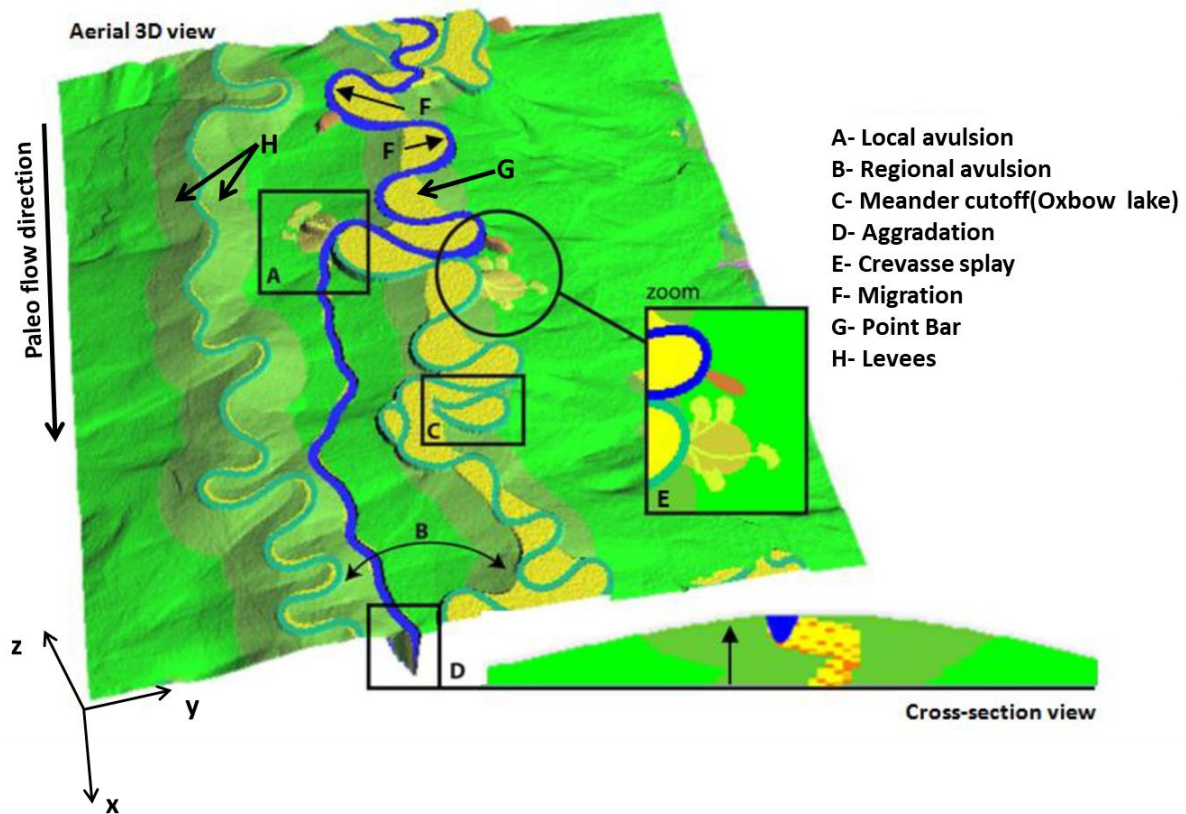
Figure 3.1: A still from Flumy to demonstrate the depositional trend (image sourced from Flumy manual and edited to requirements)

Based on the geological dataset (section 2.3) observed in the WNB, input parameters used in Flumy were:

a) Model Dimension and Paleo flow direction

The model domain of the geothermal reservoir considered in this report is of dimension 1800m x 1200m x 100m (L x W x H). Models were split into two categories: coarse scale models and fine scale models. The coarse grid models have a grid size of 30m x 30x 2.5m while the fine grid models have a grid size of 10m x 10m x 2.5m. What this means is that the 100m of thickness that Flumy generates is vertically averaged to 2.5m for each layer, thus creating fine scale and coarse scale models of 40 layers each along the z-direction. The paleocurrent flow direction was set along the longest side of the model which in our case is along the x-direction.

Parameters	Fine scale model	Coarse scale models
Reservoir Dimension	1.8km x 1.2km x 100m	1.8km x 1.2km x 100m
Number of grids	180 x 120 x 40	60 x 40 x 40
Size of each grid	10m x 10m x 2.5m	30m x 30m x 2.5m

Table 3-1: Grids sizes and dimension for fine and coarse scale models

b) Channel Depth and Width

The channel depth was set to 4m and the width to 40m. As mentioned in the above literature study, these data were derived from the core analysis.

c) The Avulsion Frequency

Flumy allows the user to control the frequency of both types of avulsions: regional and local avulsions. Due to insufficient information, this parameter was varied between 100-700 years for regional and 80-400 years for local avulsion. Based on simulation trend, it was observed that by reducing the avulsion frequency (i.e. from 360 years to 600 years for example) would result in a more meandering channel and hence resulting in more complex systems and also a wider sand body deposition often called the channel belt.

d) Overbank flow occurrence

Overbank flow floods the surfaces of the floodplains. They typically occur every few years (31). In the Netherlands, most of the channels have minor embankments that protect the floodplains from inundations and hence the expected overbank floods is about 6-7 years on an average, However, floodplains without minor embankments do experience floods about every year (32). An increase in the occurrence of flows would mean larger preservation of fine grain sediments and higher sedimentation rate. If sedimentation rate increases, then smaller grain sediments are preserved and therefore reduce the N/G. This was one of the primary parameters used to obtain realizations of different N/G. They were varied between 10-90 years in order to generate models with N/G ranging between 15-75%.
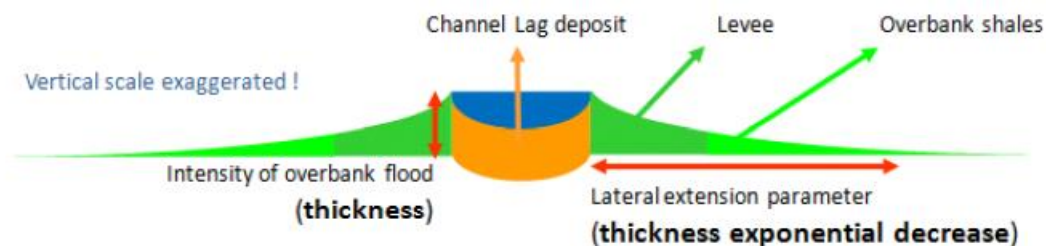
Figure 3.2: Image sourced from Flumy manual to demonstrate thickness exponential decrease and maximum thickness

e) Maximum Thickness

This parameter describes the maximum thickness deposited on levees during the overbank flow. This parameter was also used to obtain varying N/G values for the model. They were set to ranges between 0.2-0.6m thicknesses. The lower the value was set, lesser is the clay sediments on the floodplain and hence more sand which thereby increases the value of N/G of the model obtained.

f) Thickness exponential Decrease:

As we move further from the channel the thickness of the floodplain deposits decreases. This parameter was varied between 500-900m. When this parameter is set to a higher value, it increases the width and thickness of the floodplain deposit which in turn increases the aggradation rate and hence decreasing the N/G (net over gross) of the realization.

Modelling Approach

Since Flumy does not feature 3D visualization of the model, Petrel was used to visualize the model generated by Flumy. Both the fine and coarse scale model are generated as shown in **Figure 3.3** and **Figure 3.4**. Please note that Flumy is also restricted in recreating the same models between fine and coarse scales. Hence results between the two scales cannot be correlated.
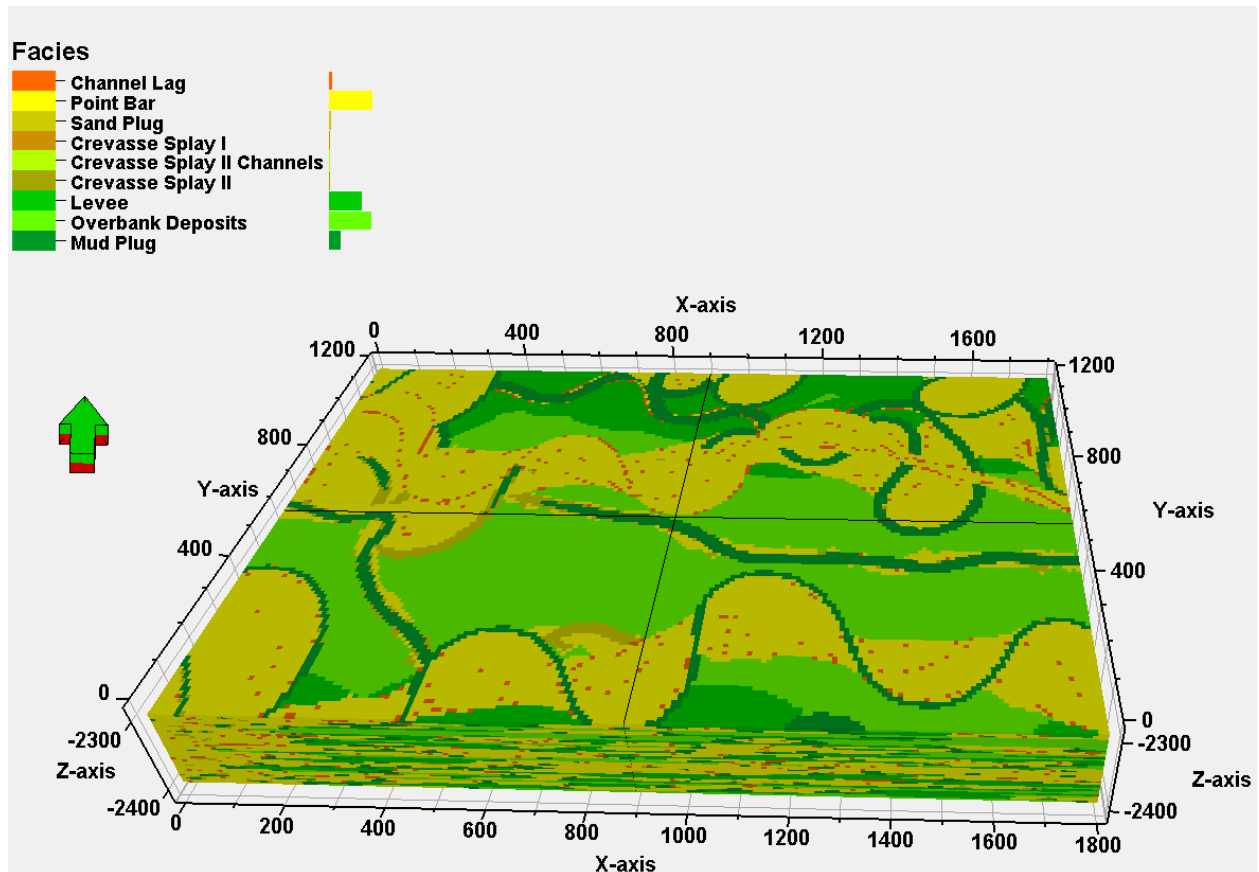
Figure 3.3: Visualization of fine scale model (180x120x40 grids) having N/G of 35%
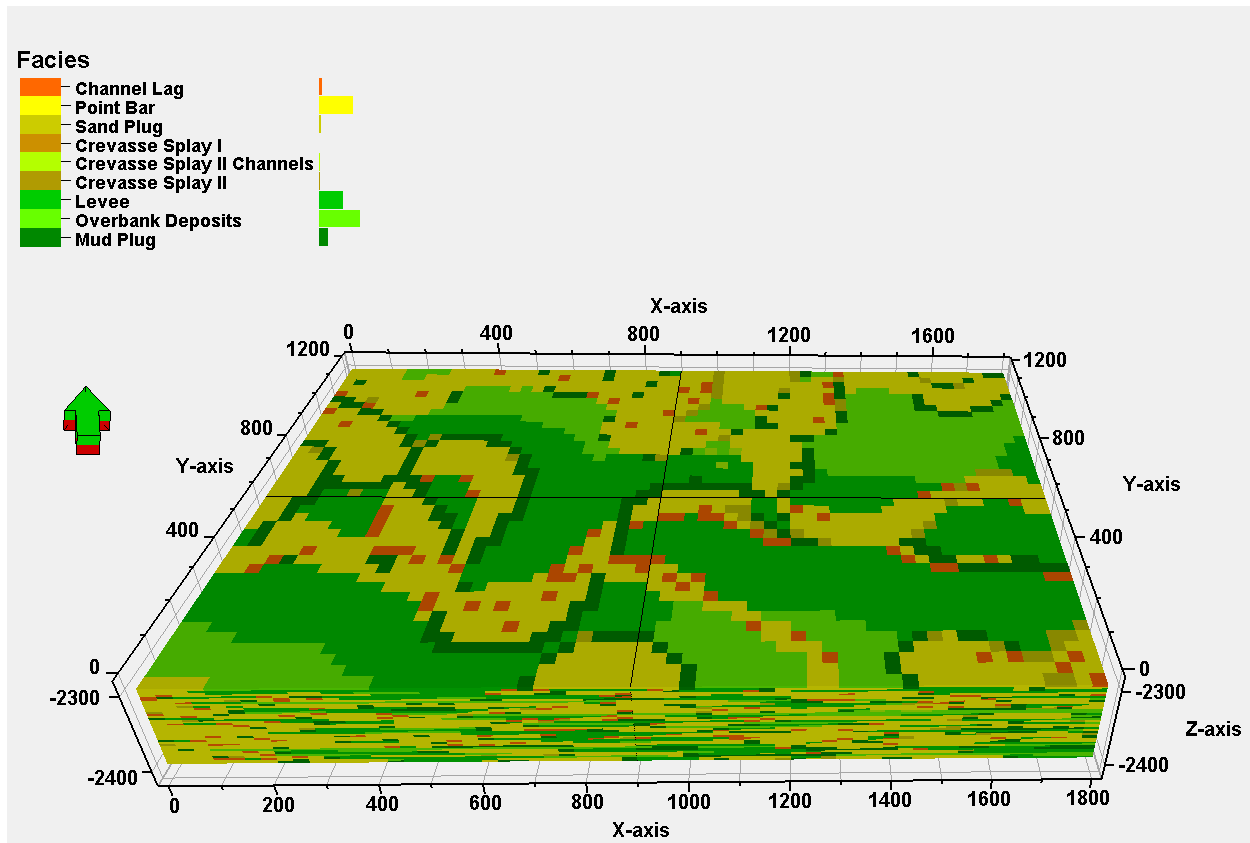
Figure 3.4: Visualization of coarse scale model (60x40x40 grids) having N/G of 35%

3.2   Property modeling of the reservoir

The model generated from Flumy has a wide range of facies distribution. Their distributions were simplified into two categories, reservoir, and non-reservoir units. Facies such as crevasse splays, overbank deposits, levees and mud plugs were considered as non-reservoir grid blocks and are identified as shale bodies. While the reservoir grid blocks consisted of point bars, sand plugs, and channel lags. These are identified as sandstone bodies. The visualization of this simplified model can be found in Appendix *A1. 1*. The shale bodies were assumed to be impermeable and homogenous with a permeability of 5mD and porosity of 10% (5). They were set to low values so that they don't affect the flow but would still have a presence of water which would contribute to the heat capacity and heat conductivity variations. For the reservoir units (sandstone bodies) a beta distribution correlation function was used to generate a heterogeneous porosity field based on the WNB core plug porosity measurements (5) . The beta distribution characteristics include mean, standard deviation, skew and kurtosis of 0.28, 0.075, 0.35 and 2.3 respectively (5). Once the porosities were distributed, the permeability was assigned to each grid. Using the petrophysical data of well MKP-11, a permeability-porosity relationship was obtained (5).

The porosity-permeability relationship is as follows:

$$K = 0.0633\ e^{(29.507\ \phi)} \qquad\qquad \textbf{\textit{3-1}}$$

Heat transfer doesn't vary drastically in models consisting heterogeneity of the thermal rock properties. (8) Hence, thermal properties such as heat conduction, heat capacity were considered to be homogeneous and isotropic. A specific value of heat capacity and conductivity were chosen for sands and shales respectively. Densities and thermal properties have been chosen among typical values for sedimentary deposits and are based on references (33; 23; 17; 3)

3.3   Inclusion of over and under burden (OB and UB) layers

Once the reservoir was distributed with thermal and fluid properties, an over and under burden layer was modeled above and below the reservoir respectively. Initially, the over and under burden layers were discretized into eight layers accounting for the temperature and pressure gradients along each layer. Results (***Figure 3.5***) showed a delay in the breakthrough plots; however, the trend of the curve remained the same as that when the layers were assumed as a single thick block. Hence the over and under burden layers were assumed to be a single thick block of 400m thickness each.
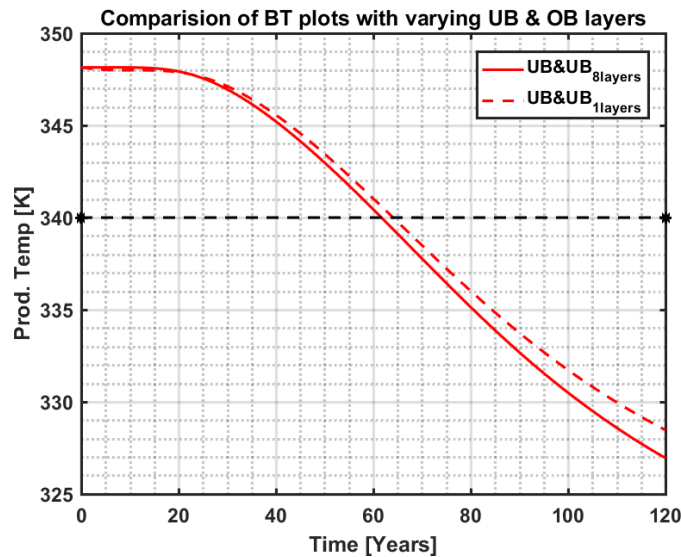
Figure 3.5: BT comparison when OB and UB layers were
discretized into 8 layers with a single OB and UB layer

 These layers were distributed with homogenous thermal and fluid properties. The porosity and permeability of these layers were set to a lower value of 5% and 0.1mD respectively. This was done to confine the fluid flow within the reservoir. Furthermore, both the underburden and overburden layers were only discretized horizontally, meaning that along the in the vertical axis, they were just a single section of 400m thick.

RESERVOIR PROPERTIES			
SANDSTONES			
Parameter	Symbol	Value	Unit
Permeability range	K	6-3000	mD
Porosity range	ϕ	15-38	%
Specific heat capacity	C	730	J/Kg-K
Volumetric heat capacity	s	1934.5	KJ/m^3-K
Thermal conductivity	κ	2.65	W/m-K
Volumetric thermal conductivity	κ	229	W/m-day-K
Density	ρ	2650	Kg/m^3
SHALES			
Parameter	Symbol	Value	Unit
Permeability	K	5	mD
Porosity	ϕ	10	%
Heat capacity	C	950	J/Kg-K
Volumetric heat capacity	s	2470	KJ/m^3-K
Thermal conductivity	κ	2	W/m-K
Volumetric thermal conductivity	κ	172.8	W/m-day-K
Density	ρ	2600	Kg/m^3
Overall thickness of the reservoir	thk	100	m

Table 3-2: Overall properties distributed to the reservoir model

GENERALIZED PROPERTIES			
Parameter	Symbol	Value	Unit
Reservoir depth	z	2300	m
Initial reservoir temperature	T_i	348.15	K
Reservoir lifetime temperature	$T_{lifetime}$	340	K
Initial reservoir pressure	p_i	200	Bars
Borehole diameter	d	0.2	m
Water injection and production rate	q_{inj}, q_{prod}	4800	m^3/day
N/G variation range	N/G	15-75	%
Distance between doublet pair	$\Delta_{doublet}$	990	m

Table 3-3: Generalized properties used in the models
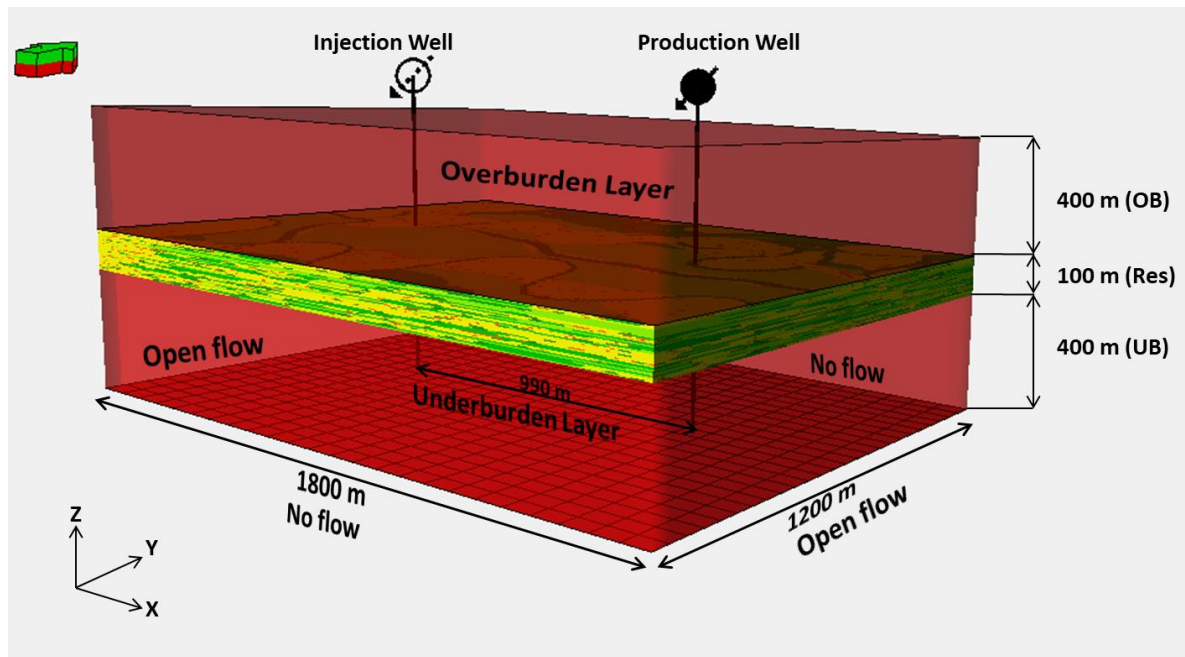
Figure 3.6: Inclusion of over and under burden impermeable layer to the reservoir model that confines the convective flow and serves only for thermal variations.

OVER AND UNDER BURDEN LAYERS			
Parameter	Symbol	Value	Unit
Permeability	K	0.1	mD
Porosity	ϕ	5	%
Heat capacity	C	950	J/Kg-K
Volumetric heat capacity	s	2470	KJ/m^3-K
Thermal conductivity	κ	2	W/m-K
Volumetric thermal conductivity	κ	172.8	W/m-day-K
Density	ρ	2600	Kg/m^3
Thickness of over burden layer	thk_{OB}	400	m
Thickness of under burden layer	thk_{UB}	400	m

Table 3-4: Properties distributed in over and under burden layer

3.4 Well placements and well identification

Once the model was populated with all the parameters during the dynamic and property modeling, the next step was to place injector and producer wells. The doublets were spaced 990m apart and are perforated through all the 40 layers of the reservoir. The placement of the wells was assumed to be perpendicular to the channel planes. In order to prevent influence of boundary conditions, the choice was made to place the doublets at the center of the model. *Figure 3.7* illustrates the placement of wells in the nine coordinates of the model. Please note that the grid dimensions in *Figure 3.7*, chosen for representation, are 90m x 75m which is much coarser compared to the actual grid sizes used for simulation. The actual grid sizes for fine and coarse models are mentioned in *Table 3-1* on page *12*.

Since large variations were observed in the thermal breakthrough while relocating the wells, eight neighboring coordinates surrounding the center (indicated as green in *Figure 3.7*) were selected as well locations to perform simulations. Please note that during every simulation, a single pair of wells was chosen. More importantly, only the location of the doublet was changed during the simulation, while the distance between the wells always remained the same. A pictorial representation of the same has been made to get a better insight. In *Figure 3.8* and *Figure 3.9*, the thermal breakthrough curves for doublets located at the center and southeast have been represented respectively. The placements of doublet at other locations are analogous to the ones seen in *Figure 3.8* and *Figure 3.9*. In this report, the spread in breakthrough refers to the difference in the lifetime of the reservoir *Figure 3.10.*
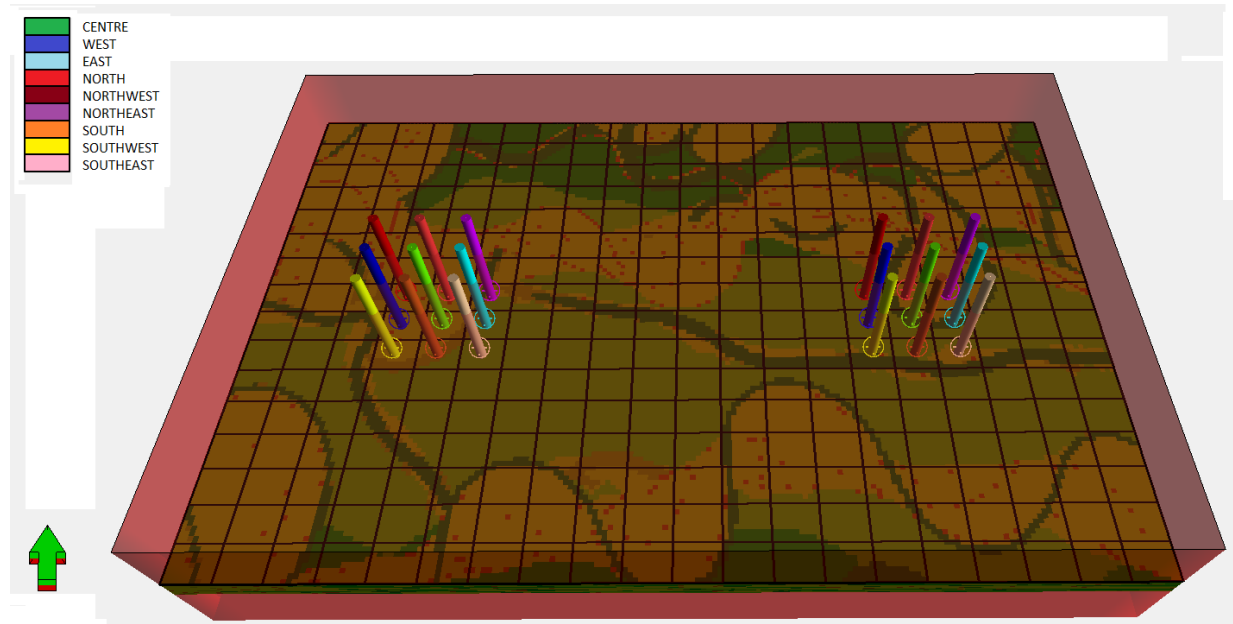
Figure 3.7: placement of wells with the center identified as green and the other doublets located at the neighboring grid cells (a fine scale model of N/G 35 was selected for representation).
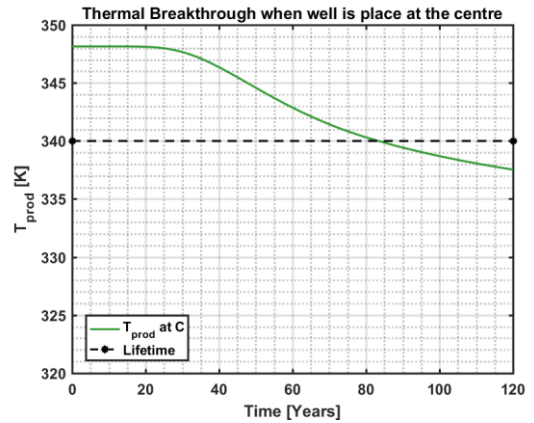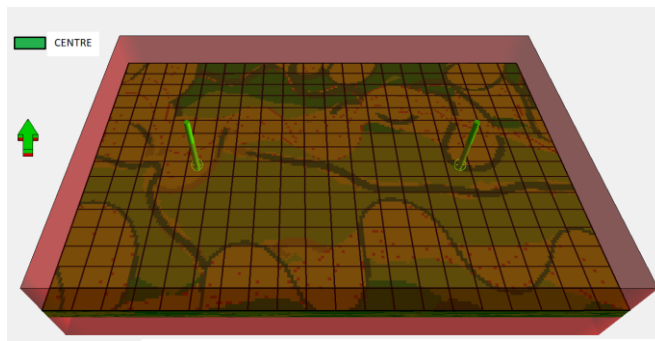
Figure 3.8: left figure represents the visualization of the doublet located at the center and the plot to the right indicates the corresponding breakthrough curve at injection and production rates of 4800m3/day
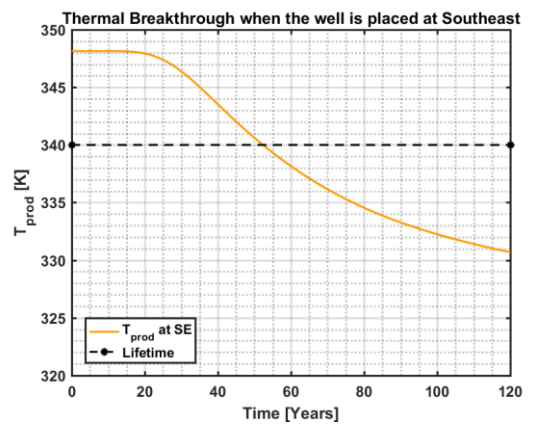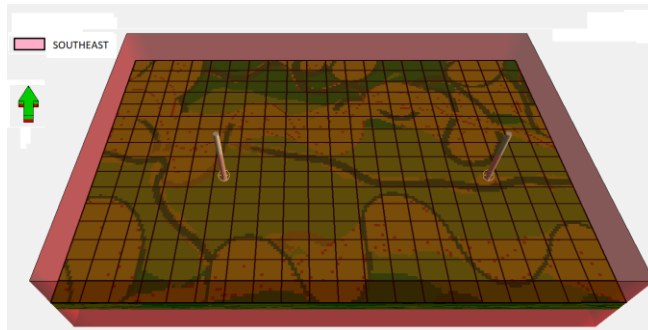
Figure 3.9: left figure represents the visualization of the doublet located at the southeast and the plot to the right indicates corresponding breakthrough curve at injection and production rates of 4800m3/day
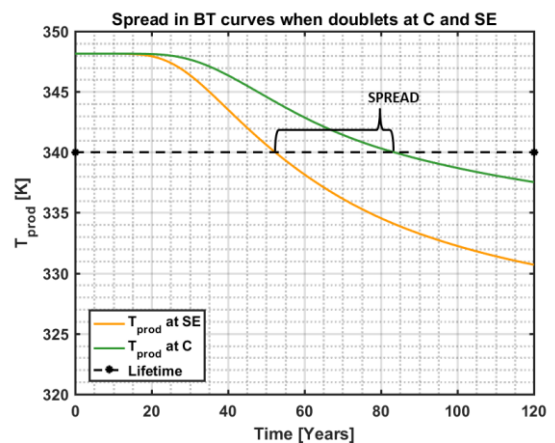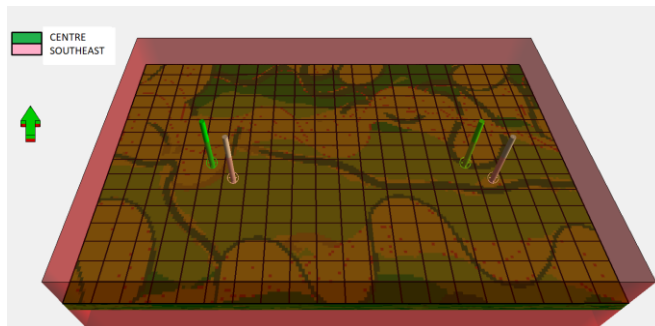
Figure 3.10: Left figure indicates the position of the doublets and the plot to the right describes the spread in the breakthrough curves just by relocating the doublet.

4

Mathematical Formulation and Methodology

4.1 Phase Diagram

The phase diagram is a chart that combines plots of pressure versus temperature to show conditions at which we can have thermodynamically distinct phases and conditions of equilibrium at which coexistence of multiple phases can exist. These diagrams are usually plotted with reference to pure water. Although geothermal wells contain impurities, many reservoirs are initially considered as pure water systems (34). Since our model has an initial temperature of 348.15K (75°C) and an initial pressure of 200 bars (20000Pa or 2900.75 psi), from the phase diagram of pure water *Figure 4.1,* we can observe that the formation fluid exists in the liquid phase. Hence our model ignores the presence of water in the gas phase and all the simulations were done assuming single phase single component water. (35).
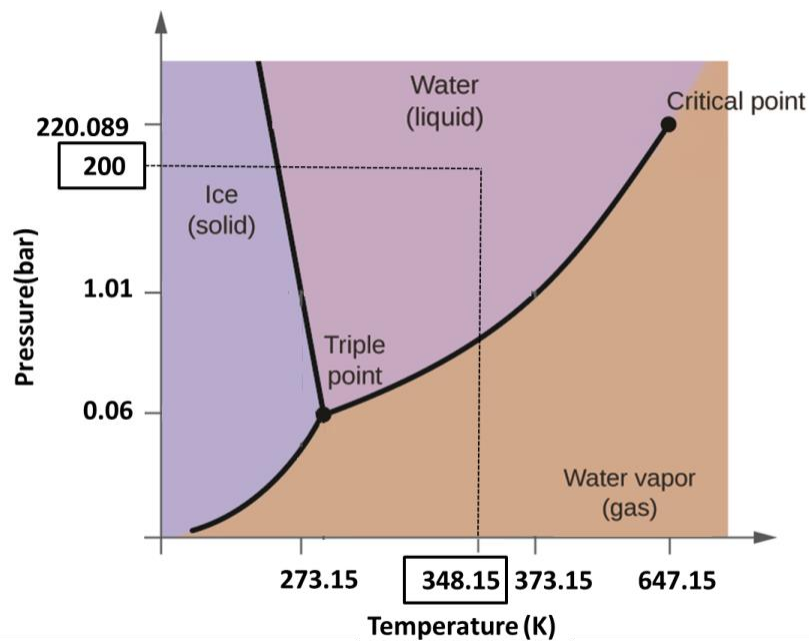
Figure 4.1: Temperature-pressure schematic phase diagram indicating the presence of single phase fluid.(plot sourced from web and edited to requirements)

4.2   Boundary Conditions

The two reservoir boundaries having the short edges (behind the well) were assigned to open flow conditions while the boundaries of the other were set to no flow boundary conditions. (as shown in *Figure 3.6* on page *18*). The goal of keeping open boundaries behind the wells is to allow the flow within the model domain, to leave the model domain without affecting the interior solution in a way that is not physically realistic. The longer edges of the boundaries were set to no flow conditions, in order to confine the reservoir within the sweep efficiency of the doublet. If the reservoirs are not bounded by sealing faults within this model dimension, then the sections outside this model boundary can be assumed as another reservoir model where a new pair of doublets can be drilled based on doublet deployment strategies (21).

4.3   Assumptions

Most of the applied assumptions are discussed in (34) and they hold for the models generated in this research as well. The following were the assumptions made:

- The reservoir fluid is single component single phase water based on the phase diagram.
- Capillary pressure effects are ignored since capillarity relates to phase pressures and in our models, we only indulge in a single phase.
- For rock, we assume constant density everywhere but for fluids, it can change because of the pressure. This introduces nonlinearity in the mass conservation equations
- No relative permeability exists since the fluid is only single phase water.
- Rock Density, reservoir thickness and intrinsic permeability are functions of space.
- Injection and production rates are kept constant at 4800m^3/day in order to maintain a constant pressure in the reservoir.
- Wells are perforated through all the layers of the reservoir section which means the over and under burden layers were not perforated.
- Since pure water is a Newtonian fluid, it is ideally viscous. Hence viscosity effects can be neglected.
- Temperature gradient along the layer is ignored.
- The pressure gradient is also ignored since the system reaches equilibrium quite quickly and hence their variations were ignored.

4.4   Governing Equations

The governing equations of fluid flow represent mathematical statements of the conservation laws of physics:

Conservation of mass: The mass of the fluid is conserved over time

Conservation of momentum: The rate of change of momentum is equal to the sum of the forces on a fluid particle. Here, Darcy's equations are used as simplified momentum balance

Conservation of energy: The rate of change of energy is equal to the sum of the rate of heat added to the fluid particle and the rate of work done on the fluid particle.

These governing equations describe the behavior of the fluid in terms of macroscopic properties such as velocity, pressure, density and temperature and their space and time derivatives. With the help of constitutive relationships, these balance equations are reduced to two nonlinear PDEs in terms of two dependent variables- pressure and temperature. (34)

Mass Conservation Equation

The standard mass conservation equation of a system having n_c components and np phases can be represented as:

$$\underbrace{\frac{\partial}{\partial t}\left[\phi \sum_{c/p=1}^{n_{c/P}} x_{cp}\rho_p S_p\right]}_{Accumulation} + \underbrace{\nabla.\left[\sum_{p=1}^{n_p} x_{cp}\rho_p u_p\right]}_{flux} + \underbrace{Q_M}_{\substack{Source/Sink \\ flux}} = 0 \qquad \textbf{\textit{4-1}}$$

Where: ϕ is the porosity of the rock, ρ_p is the mass density of phase p, S_p is the saturation of phase p, u_p is the Darcy/superficial velocity of phase p, Q_M is the source/sink term for mass conservation equation. The subscripts c/p refers to the components and phases respectively

In our study, single phase compressible pure water was considered. Hence the eq. 4-1 reduced to:

$$\frac{\partial}{\partial t}[\phi\rho_w] + \nabla.[\rho_w u_w] + Q_M = 0 \qquad \textbf{\textit{4-2}}$$

Momentum Balance

Darcy's equation was used as a simplified momentum balance equation. Darcy's Law is used to express fluid velocity in terms of pressure gradient:

$$u_p = -\underbrace{\frac{KK_{rp}}{\mu_p}}_{mobility\ term}\underbrace{[\nabla p_p + \rho_p g\nabla z]}_{potential\ term} \qquad \textbf{\textit{4-3}}$$

Where: u_p is the superficial velocity of phase p, K is the rock permeability, K_{rp} is the relative permeability for phase p, μ_p is the viscosity of phase p, p_p is the pressure of phase p, ρ_p is the mass

density for phase p, g is the gravitational constant, z is the downward depth along the vertical. Please note that the negative sign comes from the potential term.

In our model, the eq. 4-3 is reduced to

$$u = -\frac{K}{\mu}[\nabla p + \rho_w g \nabla z]$$
<div align="right">**4-4**</div>

Combining the two eq. 4-2 and 4-4 we have:

$$\frac{\partial}{\partial t}[\phi\rho] - \nabla.\left[\frac{\rho K}{\mu}[\nabla p + \rho g \nabla z]\right] + Q_M = 0$$
<div align="right">**4-5**</div>

The objective of the simulator (ADGPRS) is to compute pressures for each grid cell, such that the conservation of mass is fulfilled at any time. Please note that the equation is highly non-linear since quantities like density and viscosity are functions of pressure and temperature (36).

Energy Conservation Equation

For the heat transport, the transfer in porous matrix is governed by both conduction and convection and can be expressed as follows:

$$\underbrace{\frac{\partial}{\partial t}\left[(1-\phi)\rho_r U_r + \phi\sum_{c/p=1}^{n_{c/P}}\rho_p U_p S_p\right]}_{Accumulation} + \underbrace{\nabla.\left[\sum_{c/p=1}^{n_{c/p}}H_p\rho_p u_p\right]}_{\substack{heat\ transport \\ with\ fluid\ flux \\ (convection)}} + \underbrace{\nabla.(\kappa\nabla T)}_{\substack{heat\ flux \\ (conduction)}} + \underbrace{Q_E}_{\substack{Source/Sink \\ flux}} = 0$$
<div align="right">**4-6**</div>

Where: ϕ is the porosity of the rock, ρ_r is the mass density of rock, U_r is the internal energy of the rock, ρ_p is the mass density of phase p, U_r is the internal energy of phase p, S_p is the saturation of phase p, u_p is the Darcy/superficial velocity of phase p, H_p is the phase enthalpy of phase, Q_E is the source/sink term in energy conservation equation. The subscripts c/p refers to the components and phases respectively while r refers to rock and f refers to fluid.

In our model, the eq. 4-6 is reduced to

$$\frac{\partial}{\partial t}[(1-\phi)\rho_r U_r + \phi\rho_w U_w] + \nabla.[H_w\rho_w u_w + (\kappa\nabla T)] + Q_E = 0$$
<div align="right">**4-7**</div>

The objective of the simulator (ADGPRS) is to compute temperature for each grid cell, such that the conservation of energy is fulfilled at any time. Please note that the equation is also non-linear since quantities like internal energy and enthalpy are functions of pressure and temperature. (36)

4.5   **Discretization of Governing Equations**

Before linearizing, ADGPRS discretizes the nonlinear set of equations. A finite volume method with fully implicit approximation was implemented to discretize the governing equations. Standard two point flux approximation methods are used for spatial discretization (Δx) and backward Euler approximation was used for time discretization (Δt). All the unknowns are defined at the cell centers. But, in order to express the flux between two neighboring cells, transmissibilities (Γ) is calculated at the cell interface.

Discretized form of mass conservation eq. 4-2 along 'l'

$$V[(\phi\rho)^{n+1} - (\phi\rho)^n] + \Delta t \sum_l [\rho^l \Gamma_f^l \Delta\psi^l]^{n+1} + \Delta t. V[Q_M]^{n+1} = 0$$

4-8

Discretized form of energy conservation eq. 4-7 along 'l'

$$V\left[\left((1-\phi)\rho_r U_r + \phi\rho_w U_w\right)^{n+1} - \left((1-\phi)\rho_r U_r + \phi\rho_w U_w\right)^n\right]$$
$$+ \Delta t \sum_l [H_w^l \rho_w^l \Gamma^l \Delta\psi^l + \Gamma_c^l \Delta T^l]^{n+1} + V[Q_E]^{n+1} = 0$$

4-9

Where the superscript 'l' represents all quantities defined at the interface between the connected cells. All indices for grid cells are left out and are implied.

$V = V(x, y, z)$ is the cell volume

ρ- To obtain the values density equations of state are used {more details can be found in (37)}

$\Gamma_f^l = \Gamma \left[\frac{K^l}{\mu^l}\right]$ is the flow transmissibility along the interface l of the connected cells, here K^l/μ^l is the mobility ratio (λ) at the interface l obtained by harmonic averaging of the connected cells

$\Gamma = \Gamma(x, y, z)$ involves the geometry of the control volume

$\Delta\psi^l = (p^b - p^a) + \rho g(z^a - z^b)$, ψ^l is the potential term along the interface l, the superscript b and a for p is the pressure difference between the blocks b and a from right of the interface l to its left and superscript a and b for z is the change in depth between the blocks a and b from top of the interface l to its bottom.

$\Gamma_c^l = \Gamma\kappa$ Is the thermal transmissibility along the interface l of the connected cell

$U_r = C_r(T - T_{ref})$ and $U_f = C_f(T - T_{ref})$, C is the specific heat capacity and T_{ref} is the reference temperature, subscripts r and f refer to rock and fluid respectively.

$$H_f = U_f + \frac{p_f}{\rho_f}$$

$$\kappa = \phi\kappa_w + (1-\phi)\kappa_r$$

More detailed relationships for κ, U and H are mentioned in (37; 38)

4.6   Non-linear Formulations

Construction of Residual

The approach used in ADGPRS for constructing the residual and Jacobian arrays is a simple and convenient "connection based technique" wherein all the connections (nothing but thermal and flow transmissibilities at interfaces between the grid blocks) are tracked while computing the flux terms (39) (Please refer eq. 4-1 and 4-6 to identify the flux terms in mass and energy conservation equations respectively). The beauty of this approach is that it only requires the data structure identifying each pair of connected blocks and the corresponding geometric factors of each connection. In this approach, the no-flow boundaries and barriers (if any) are excluded due to the absence of a connection. A detailed understanding of this approach can be obtained by referring to (39).

Connection list (Mass Conservation Eq.)	Connection list (Energy Conservation Eq.)
$\{1,2: \Gamma_{f1}\}$	$\{1,2: \Gamma_{f1} \; \Gamma_{c1}\}$
$\{1,4: \Gamma_{f2}\}$	$\{1,4: \Gamma_{f2} \; \Gamma_{c2}\}$
$\{2,3: \Gamma_{f3}\}$	$\{2,3: \Gamma_{f3} \; \Gamma_{c3}\}$
$\{2,5: \Gamma_{f4}\}$	$\{2,5: \Gamma_{f4} \; \Gamma_{c4}\}$
$\{3,6: \Gamma_{f5}\}$	$\{3,6: \Gamma_{f5} \; \Gamma_{c5}\}$
$\{4,5: \Gamma_{f6}\}$	$\{4,5: \Gamma_{f6} \; \Gamma_{c6}\}$
$\{4,7: \Gamma_{f7}\}$	$\{4,7: \Gamma_{f7} \; \Gamma_{c7}\}$
$\{5,6: \Gamma_{f8}\}$	$\{5,6: \Gamma_{f8} \; \Gamma_{c8}\}$
$\{5,8: \Gamma_{f9}\}$	$\{5,8: \Gamma_{f9} \; \Gamma_{c9}\}$
$\{6,8: \Gamma_{f10}\}$	$\{6,8: \Gamma_{f10} \; \Gamma_{c10}\}$
$\{7,8: \Gamma_{f11}\}$	$\{7,8: \Gamma_{f11} \; \Gamma_{c11}\}$
$\{8,9: \Gamma_{f12}\}$	$\{8,9: \Gamma_{f12} \; \Gamma_{c12}\}$

Figure 4.2: Illustration of connection pairs(Red) for both mass and energy conservation equations, Notice that the boundaries are ignored since they do not have a neighboring cell to connect with.

In this connection based technique the following steps are performed to constrict the residual arrays:

Establishing a connection list
The first task in this approach is to establish all the possible connections pairs for a given model (in our case, it is the fluid transmissibilities $[\Gamma_f]$ for mass conservation equation and a combination of fluid and thermal transmissibility $[\Gamma_f \; \Gamma_c]$ for energy conservation equations)
As an example, ***Figure 4.1*** on page ***21*** illustrates the connection pairs in a 2D Cartesian system for both mass and energy conservation equations. It can be noticed that each type of connection comprises of only the two neighboring grid cells, the pair of connections are not repetitive and that the boundaries (no flow conditions) are ignored since they do not have a neighboring cell to connect with. The computation algorithm for 1D, 2D and 3D models for both structured and unstructured grids are analogous.

Computation of flux" Q_k" between two adjacent grids

Once the transmissibilities are obtained for each of the connection, the next step is to calculate the flux along all these connections. One has to pay close attention to the direction of flow since it plays a vital role in assigning signs to these fluxes, during the construction of the residual for each grid cell.

Let's now assume i and j to be an indication for all the left and right grid cells respectively along each corresponding interfaces. For instance, in **Figure 4.3** it is observed that the flux traverses from cell i to cell j, which implies a positive flux into cell j and a negative flux into cell i. This implies that while computing the mass and energy balance residual for cell i, the flux between them would have been computed and hence when computing the residual for cell j, the repetition of flux calculations can be avoided.
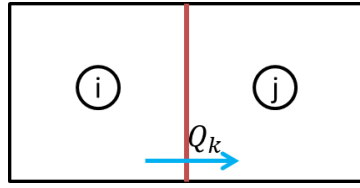
For mass conservation equation
$$Q_k = \Gamma_f(p_i - p_j)$$
For energy conservation equation
$$Q_k = \Gamma_f(p_i - p_j) + \Gamma_c(T_i - T_j)$$

Figure 4.3: Left- Illustration of flux transfer from left cel (i) to right cell (j); Right- flux for energy and mass conservation equations

Computation of Residual term for each grid block

The computation of residual for each grid block is performed in steps

Step 1: Initially the accumulation term and the source/sink term are evaluated for each cell. This is done separately since these terms are affected only by local properties of grid cell. This part of the residual term is the same for both mass and energy equations.
$$i: R_i = A_i^{n+1} - A_i^n + \Delta t \, W_i^{n+1}$$

Note that the accumulation part of the residual term for cell j is also the same and W is nothing but the fluxes Q_M and Q_E in the mass and energy equations respectively. They are also included in this part of the residual computation since they are affected by properties local to the grid cell.

Step2: This step involves the addition of the fluxes (Q_k) that were calculated for each connection, into the residual term. This is done in such a way that, for a particular connection, the left grid cell (i) would be assigned a negative flux while the right grid cell (j) would be assigned a positive flux. Doing this would result to the following residual terms in every i^{th} and j^{th} cells

$$k \to \{i, j\}: R_i = R_i - \Delta t Q_k^{n+1} \quad , \quad R_j = R_j + \Delta t Q_k^{n+1}$$

Notice that the term Q_k would be different for mass and energy equations. (Refer **Figure 4.3**)

Construction of Jacobian Matrix

The residual equation is now the sum of all the residual terms for all cells as a function of all of the unknowns (in our case being pressure and temperature). Using this residual equation, ADGPRS constructs the Jacobian used by the nonlinear solver. This is done by implementing an automatic-differentiation library that forms the analytical Jacobian automatically based on the residual formulation. (38) It allows the flexible treatment of all non-linear physics or formulations through

the automatic differentiation framework in the simulator. (38) The Jacobian matrix consists of the derivatives of all the residual equations with respect to nonlinear unknowns (38).

Newton Raphson's Method

The above-mentioned system of equations is highly non-linear. The linearization of it is performed using Newton Raphson's technique. Newton's method is an approximation technique for finding roots of the nonlinear equation. It offers a possibility of much faster convergence and can be used for solving system of equations. The Newton's method solves the linear system based on the residual at each nonlinear iteration. This iterative process follows a set guideline to approximate one root, considering its function, its derivative, and an initial guess.

For mass conservation equation: in our case, the initial guess is taken as x_n where x_n are the unknowns at current time step to solve for unknowns at the next time step x.

$$non\ linear\ solver \begin{cases} x^0 = x_n; \quad J(x^0)(x^1 - x^0) = -R(x^0) \quad \xrightarrow{linear\ iterations} \quad A_0 y_0 = b_0 \\ x^1 = x^0 + y_0; \quad J(x^1)(x^2 - x^1) = -R(x^1) \xrightarrow{linear\ iterations} \quad A_1 y_1 = b_1 \end{cases}$$

These iterations are repeated until the residual form converges to a prescribed tolerance.

$$\|R(x^k)\| < \varepsilon_1 \ and \ \|y_k\| < \varepsilon_2$$

$$p^{n+1} = x^k \Longrightarrow t = t + \Delta t, p^n = p^{n+1}, new\ time\ step\ is\ strated$$

The unknowns for our equations are pressure and temperature.

Time Step

For a non-linear solver, it's important to choose time steps wisely. This requires a balance between choosing a time step that is small enough such that the nonlinear solver would still converge in a reasonable number of nonlinear iterations and large enough such that the simulation computes in a reasonable time frame. During convergence issues, usually, computations are repeated with a smaller time step size(Δt). If the nonlinear solver converges after a specified time step, the subsequent time step size is increased by a fixed multiplier. If the nonlinear solver does not converge, the time step size is reduced by dividing it by a fixed constant. If the time step reaches a minimum size, the simulation would stop. (38)

4.7 Streamlines

In a lot of publications in the petroleum engineering literature authors use the concept of streamlines, as early as Muskat and Wycoff's 1934 paper (40). It has received repeated attention as a way to numerically predict the movement of fluid, even after the start of finite difference methods in the early 1960s. In cell-based simulation techniques like finite difference or finite elements, the phase saturation and components are transported from cell to cell, whereas the streamline simulations follow a flow based grid technique along which the transport of fluid occurs. (41)

Streamline is a path traced by a massless particle moving with the flow. Streamlines are tangential to the velocity of the moving fluid. Streamlines are generally used in reservoir simulation to visualize the flow field that defines the capture zones of the well. It can also be used to estimate sweep efficiency and check accuracy in upscaling techniques, evaluate the efficiency of injectors and producers (42).

Mathematics of the streamline method

To compute streamlines, initially, the nonlinear solution of coupled conservation for mass and energy is solved. Once the pressures are obtained at the nodes of the grid cell, it is possible to compute velocity at every interface of all the grid cells by applying Darcy's law
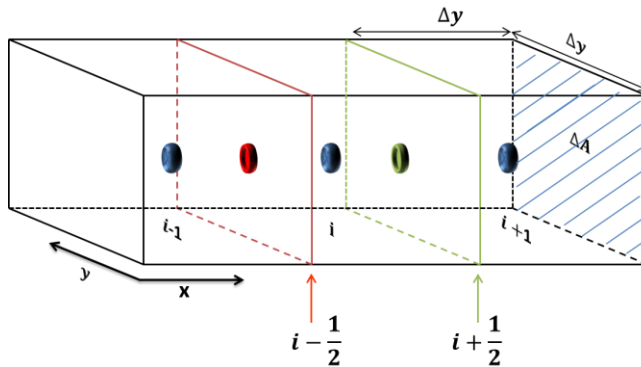
$$u_{i+\frac{1}{2}} = -\Gamma_{i+\frac{1}{2}}[(\mathrm{p}_{i+1} - p_i) + \rho_w g \Delta z]$$

"Δz" is only applicable along the z-axis and hence can be ignored while computing velocity along x and y directions.

The Γ at the interface has already been described under section **4.5**.

Figure 4.4: Representation of grid centers and grid interfaces with respect to cell i.

Once the velocities are computed for each grid cell the streamlines can be traced from injection to production wells.

Tracing of streamline

For tracing streamlines, initial assumptions are made that the velocity field varies linearly in each coordinate direction within a grid block and that they are independent of velocities in other direction. (43).

Using the above-mentioned assumption, the velocity u_x can be written in point-slope form as

$$u_x = u_{x_o} + m_x(x - x_o) \qquad \textbf{\textit{4-10}}$$

Here, m_x is the velocity gradient and is defined as

$$m_x = (u_{x_{\Delta x}} - u_{x_o})/\Delta x \qquad \textbf{\textit{4-11}}$$

Δx is the length of the grid block in the x direction.

w.k.t $\quad u_x = \dfrac{dx}{dt}$, hence eq. 4-10 can be integrated to obtain the exit times Δt out of each face given an arbitrary entry point (x_i, y_i, z_i)

$$\Delta t_{e,x} = \frac{1}{m_x} \ln \left[\frac{u_{x,o} + m_x(x_e - x_0)}{u_{x,o} + m_x(x_i - x_0)} \right] \qquad \textbf{\textit{4-12}}$$

$$\Delta t_{e,y} = \frac{1}{m_y} \ln \left[\frac{u_{y,o} + m_y(y_e - y_0)}{u_{y,o} + m_y(y_i - y_0)} \right] \qquad \textbf{\textit{4-13}}$$

$$\Delta t_{e,z} = \frac{1}{m_z} \ln \left[\frac{u_{z,o} + m_z(z_e - z_0)}{u_{z,o} + m_z(z_i - z_0)} \right] \qquad \textbf{\textit{4-14}}$$

Figure 4.5: There streamline traced in a Cartesian cell. Given an arbitrary entry/inlet point, the time to exit as well as the exit point can be analytically determined. Image replicated from (42)

Where $(x, y, z)_e$ are the exit coordinates. The streamline will now exit from the face having the smallest exit time value Δt_m. Finally the exit position can be calculated by substituting Δt_e into eq. **4-12, 4-13, 4-14** and solving for x_e, y_e, z_e as follows

$$x_e = \frac{1}{m_x} \left[u_{x,i} \exp(m_x \, \Delta t_m) - u_{x,o} \right] + x_0 \qquad \textbf{\textit{4-15}}$$

$$y_e = \frac{1}{m_y} \left[u_{y,i} \exp(m_y \, \Delta t_m) - u_{y,o} \right] + y_0 \qquad \textbf{\textit{4-16}}$$

$$z_e = \frac{1}{m_z} \left[u_{x,i} \exp(m_z \, \Delta t_m) - u_{z,o} \right] + z_0 \qquad \textbf{\textit{4-17}}$$

For more details on streamlines, one can always refer to (44; 43).

5

Results and Discussion

5.1   Validation of ADGPRS geothermal framework and model

As stated in the introduction, the workflow implemented during the course of the thesis was similar to the approach used by Willems et al (21). However, the simulation results generated by Willems et al (21)   were obtained using COMSOL. Unlike ADGPRS, which is based on a finite-volume discretization, COMSOL follows a finite element approach. Hence it was important to validate the simulation results obtained between these approaches. The validation of the conventional geothermal formulation in the ADGRPS framework was performed by Khait and Voskov (18). The paper describes the comparison of simulation results using ADGPRS to that of the original COMSOL model used by Willems et al (45). These results provide confirmatory evidence that both ADGRPS and COMSOL yield very similar results for up to 50 years, which comprises a major part of a reservoirs lifetime (*Figure 5.1*).
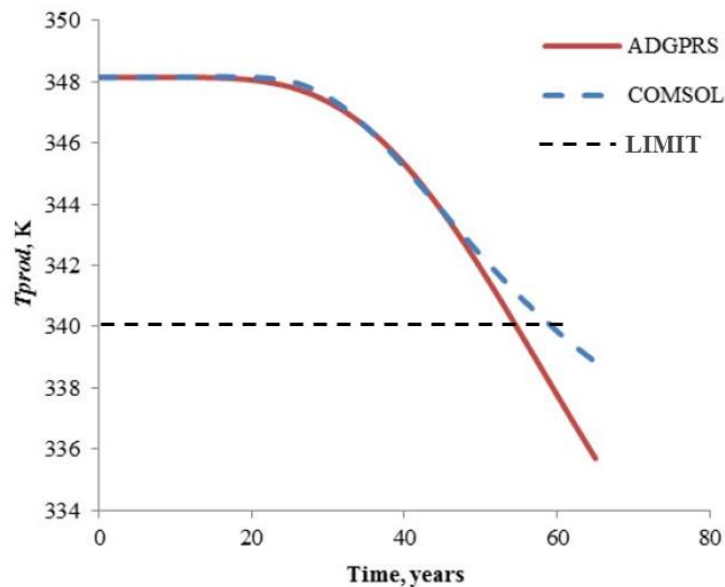
*Figure 5.1: Comparison between ADGPRS and COMSOL for the
same geological model*

Results and Discussion

Please note that in this section, the model used for reference to validate the ADGRPS with COMSOL frameworks is termed as the "original model". The original model was then tested with our input parameters.

As mentioned by Khait and Voskov (18), the original model used for the comparison between ADGPRS and COMSOL framework, has a reservoir dimension of 2km x 1km x 50m with 100 x 50 x 20 grid blocks. The injection and production rates were kept constant at $q = 2400m^3/day$. The doublets were placed 990m apart and were perforated through all the layers of the reservoir. By consuming energy from the reservoir, the production well produces hot water at $T_{prod} = 348\,K$, while the injection well returns cold water into the reservoir at $T_{inj} = 308\,K$ (18). The model generated in this report has fairly similar characteristics with subtle variations in the dimensions. The boundary conditions were similar to the ones mentioned in section *4.2* (page*22)*. Also in our model the depth of each layer varies with thickness, while in the original model the depth was assumed to be the same. These variations were implemented in the test model and the thermal breakthrough was computed. The results of the same are represented in *Figure 5.2* . A detailed description of the modifications can be found in appendix *A1. 2*.
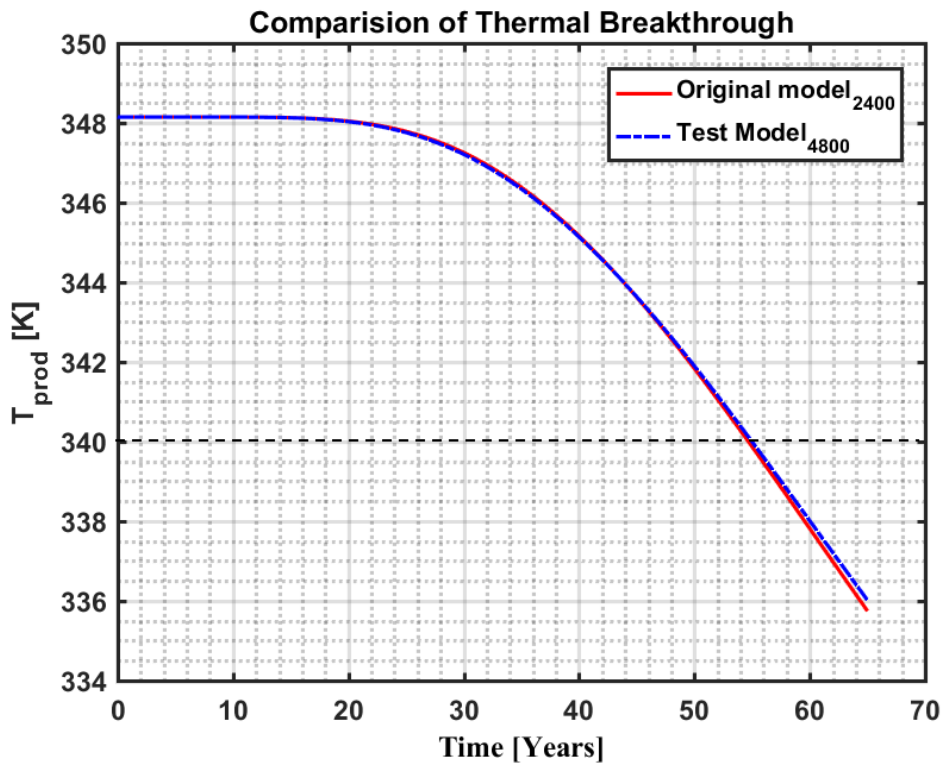
Figure 5.2: Comparison between original and test model

5.2   **Base Case Model**

Once the test model was validated, the input parameters of the test model were used in the geological models generated using Flumy. The range of parameters used for generating static geological models is described in section **3.1**. Using these ranges in input parameters, several coarse scale models having wide channel deposits were generated having N/G between 15%-75%. These models were populated with hydraulic and thermal properties as described in section **3.2** for both the reservoir and the under and overburden layers and then simulated using ADGPRS simulator. Please note that the base case model always has under and over burden layers unless mentioned otherwise, **Figure 5.3** is just a representation of the locations of the wells. Amongst the wide range of models, N/G 35% was observed to have a significant difference in the lifetime of the reservoir when the doublets were placed at different locations. The **Figure 5.4** on page **34** represents the variation in the breakthrough curves when the model (N/G 35%) was simulated each time for doublets placed at the center(C), west(W), east(E), northwest(NW), north(N), northeast(NE), south(S), southwest (SW) and southeast (SE) respectively. From **Figure 5.5**, it can be observed that the system has a lifetime of 34 years when the well was located in the West and a lifetime of 62 years when the well was relocated to the North. It is evident that the North and West have the maximum lifetime difference of 28 years. Since the aim of the thesis was to investigate the root cause of this spread/variation in the lifetime, the two extreme cases, one being the north (N) and the other being the west (W), was chosen to represent the sensitivity study. In the upcoming sections, various sensitivity analyses were carried out in the two extreme cases.
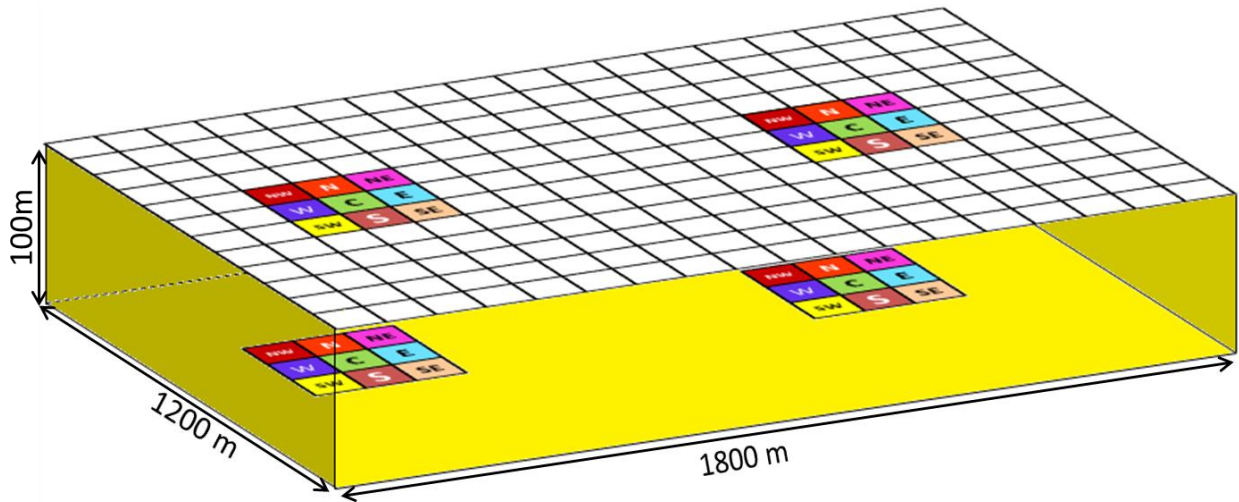
Figure 5.3: Illustrates the locations at which the doublet was placed. A difference of 30 years was observed in the lifetime of the reservoir when the doublets was relocated from the west to the north in a coarse model having 60 x 40 x 40 grids and 30m x 30m x 2.
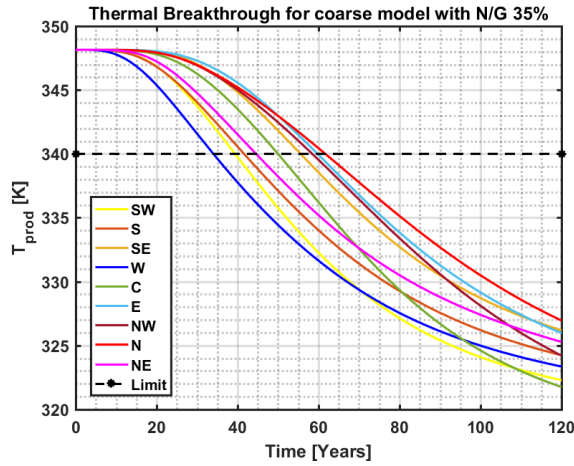
Figure 5.4: BT curves for all the nine coordinates for a coarse model with N/G 35%
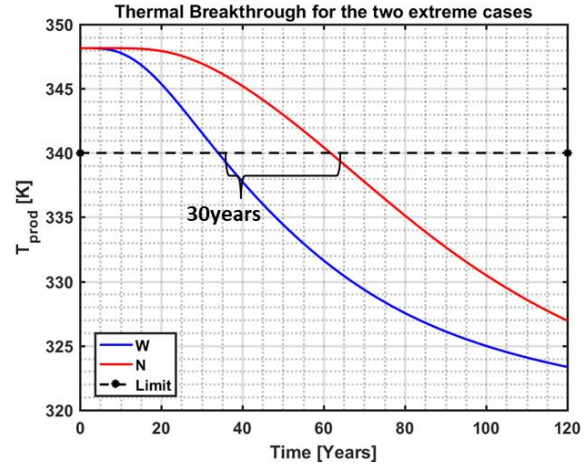
Figure 5.5: BT curves for the two doublet locations that showed a significant difference of 30 years in the reservoir lifetime.

5.3   Sensitivity analysis on base case model

Ignoring Thermal Rock Heat Conductivity

Heat transfer in a geothermal system mostly occurs by convection and to a lesser extent by conduction. This is because most of the flow simulations are generally representative of a braided system where the flow is generally straight and has minimum hindrance from the rock as shown in *Figure 5.6*. However, since we deal with the meandering systems, there is a lot more interaction between the fluids and rocks and hence thermal conductivity also does play a role.   Compared to water, rocks are better conductors of heat since their molecules are tightly packed. Hence rock conduction is a process by which heat energy is transferred from the rock to the surrounding water molecules.
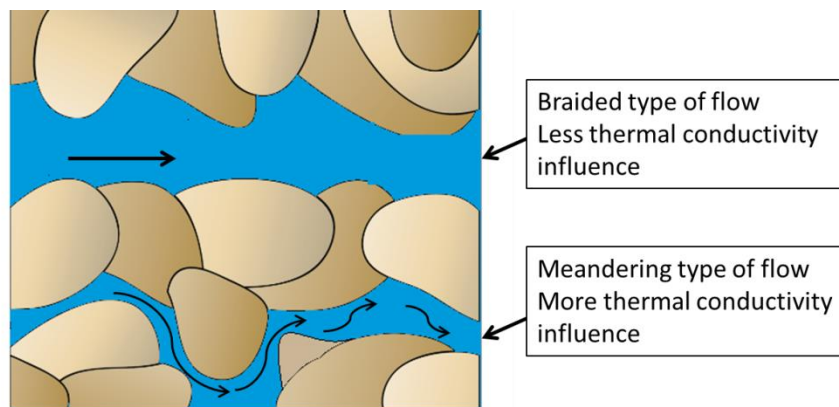
Figure 5.6: Illustration of hindrance in flow faced by meandering rivers compared to that of a braided type

In *Figure 5.7*, the solid lines represent the base case model which includes the presence of rock heat conductivity while the dotted curves indicate the breakthrough curves when the heat conductivity is completely ignored.

In our base case simulations, the cold water that is being injected into the reservoir comes in contact with the rocks. Since rocks have a higher conductivity compared to water, the heat energy is transferred from the rocks to the cold water thereby increasing the temperature of the injected cold water. Over time, as the portion of injected cold water propagates through the reservoir, the energy from the rocks makes the water warm. Hence the cold waterfront is now delayed, thereby resulting in a delay in the breakthrough time.

By ignoring the rock conductivity, there is no thermal recharge taking place between the cold water and its surrounding rocks. Hence, due to the absence of heat flux, an early breakthrough can be observed.
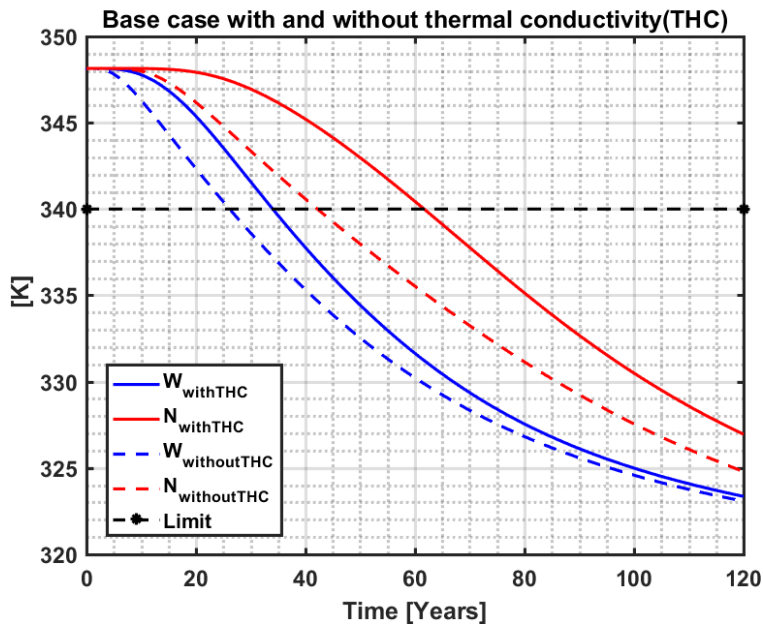
Figure 5.7: Plot shows the variation in the BT trajectories from the base case while ignoring the heat conductivity of the rock. No significant influence in the spread is observed.

Base case [κ- KJ/m-day-K]	
Sandstones	228.96
Shale	172.8
Water	57.88

Ignoring Rock Heat Conductivity [κ- KJ/m-day-K]	
Sandstone	0
Shale	0
Water	57.88

Base case [Years]	
Spread	28

Ignoring Rock Heat Conductivity [Years]	
Spread	16

Table 5-1: Comparison of the base case with the simulation results from ignoring rock heat conductivity

However, our main aim was to identify if this parameter contributes to a change in the spread of the breakthrough curves between the North and West location. It was observed that it does not play a significant role.

Reducing Rock Heat Capacity to a constant value

Specific heat capacity is defined as the amount of thermal energy required to raise the temperature of a unit of the mass of a substance by 1K. In *Figure 5.8,* the solid lines (base case) represent the breakthrough curves when the rocks have a specific heat capacity of approximately 2000 kJ/m^3-K while the dotted lines represent the breakthrough curves when the rocks have a specific heat capacity of approximately 1000 kJ/m^3-K. The higher the specific heat, the longer is the ability of the rock to retain heat. Since in, the base case, rocks can retain heat for a greater duration, there is a greater thermal recharge of water which thereby delays the thermal breakthrough of the cold waterfront.
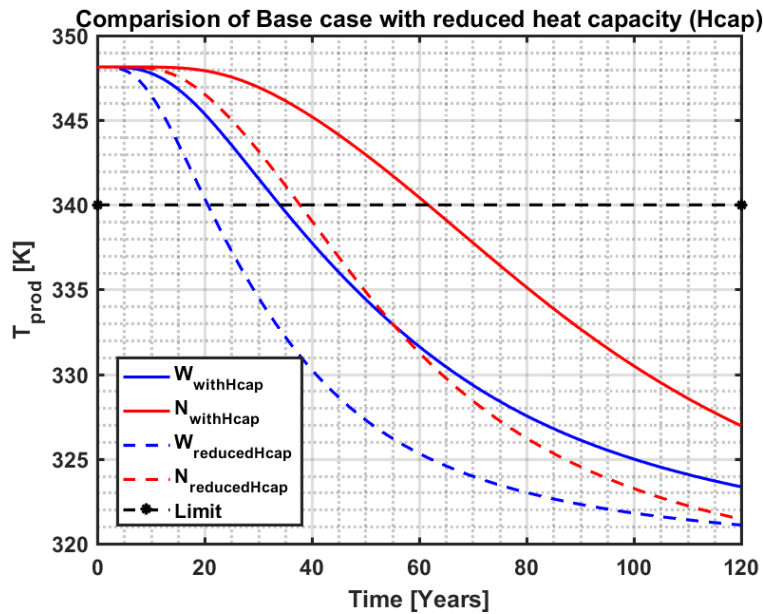
Figure 5.8: Plot shows the variation in the BT trajectories from the base case while reducing the heat capacity of the rock. No significant influence in the spread is observed.

Base case [cp- KJ/m^3-K]	
Sandstones	1934.5
Shale	2470
Water	4187

Ignoring Rock Heat Capacity [cp- KJ/m^3-K]	
Sandstone	1000
Shale	1000
Water	4187

Base case [Years]	
Spread	28

Ignoring Rock Heat Capacity [Years]	
Spread	16

Table 5-2: Comparison of the base case with the simulation results from reducing rock heat capacity.

However, it's also evident from the plots that reducing the rock specific heat capacity does not significantly influence the variation in the spread between the breakthrough curves.

Reducing Reservoir thickness

The base case simulations were performed on a reservoir with a thickness of 100m discretized into 40 layers. Here, an attempt was made to identify the sensitivity in the thickness of the reservoir. In this analysis, all the 40 layers of the model were taken into consideration however, the vertical size of each layer was now considered 1.25m apart, while in the base case every layer was 2.5m apart. This goes to say that the reservoir is currently 50m thick which is half of what it was used in the base case (100m thick). To account for the reduced volume, the injection rates were also reduced to half.
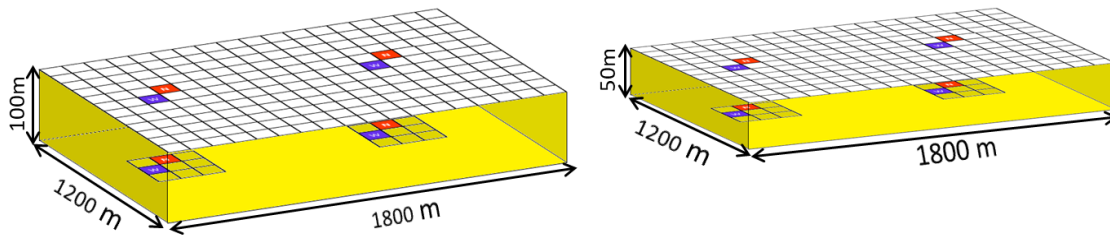
Figure 5.9: left demonstrates the base model with 100m thickness and 40 layers(2.5m each), right demonstrates the reduced thickness model with 50m thickness and 40 layers(1.25m each)
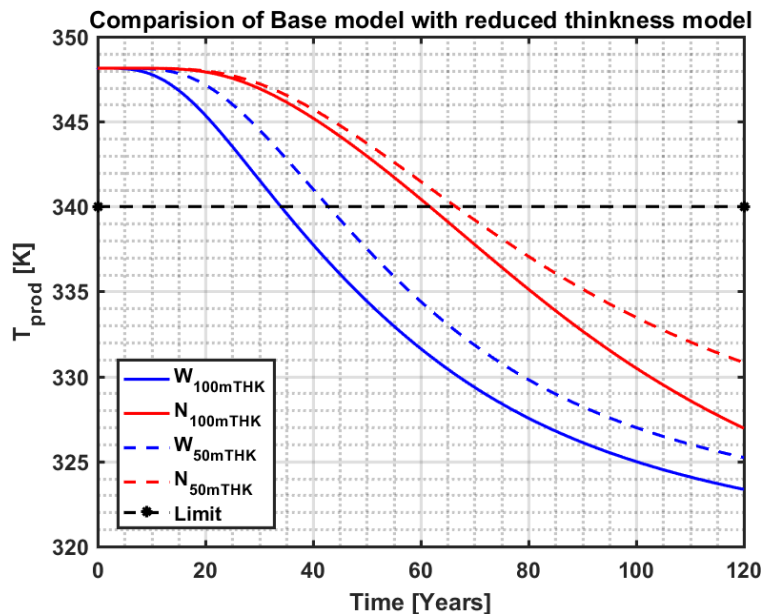
Figure 5.10: Plot shows the variation in the BT trajectories from the base case while reducing the heat capacity of the rock. No significant influence in the spread is observed.

Base case [thickness - m]	
Reservoir	100
No. of layers	40
Each layer	2.5
Rates	4800 m^3/day

Reduced thickness model [m]	
Reservoir	50
No. of layers	40
Each layer	1.25
Rates	2400 m^3/day

Base case [Years]	
Spread	28

Reduced thickness model [Years]	
Spread	23.7

Table 5-3: Comparison of the base case with the simulation results from reducing reservoir thickness.

Despite reducing the thickness of the reservoir, the results from the **Figure 5.10** still offer compelling evidence for the spread of the breakthrough curves. Hence, it could be inferred that the thickness of the reservoir also does not play a contributing factor for these huge spreads.

Ignoring overburden and under burden (OB and UB) layers

Here an analysis of the effect of over and under burden layers was performed. The overburden and under burden layers were assumed to be impermeable zones and only contributed to thermal conduction of the fluids. By comparing the plots of the base case and the model without over and under burden layers, it could be observed that the role of the over and under burden layers wasn't significant enough for huge thermal variations.

The effect of the over and underlain layers can be correlated to three parameters: one is the thickness of the reservoir and the other being the rate of injection of the cold water and lastly the layer which has the earliest breakthrough. An attempt was made to identify its sensitivity on models that were reduced to half the size of the base case model. Results showed that the presence of over and under burden layers did not contribute to a significant change in the lifetime of the reservoir. One such result has been attached to the appendix **A1. 3.** Nevertheless, the effect of over and under burden layers would be more influential depending on the layer where we observe the earliest breakthrough. If the layers having the earliest breakthrough are somewhere in the middle section of the reservoir then the over and under burden layers would have less influence than if the layers with the earlier breakthrough are close to over and under burden layers.

Base case [thickness - m]	
Over burden	400
Underburden	400
Rates	4800 m^3/day

Ignoring OB UB model [m]	
Over burden	400
Underburden	400
Rates	4800 m^3/day

Base case [Years]	
Spread	28

Ignoring OB UB model [Years]	
Spread	26.3
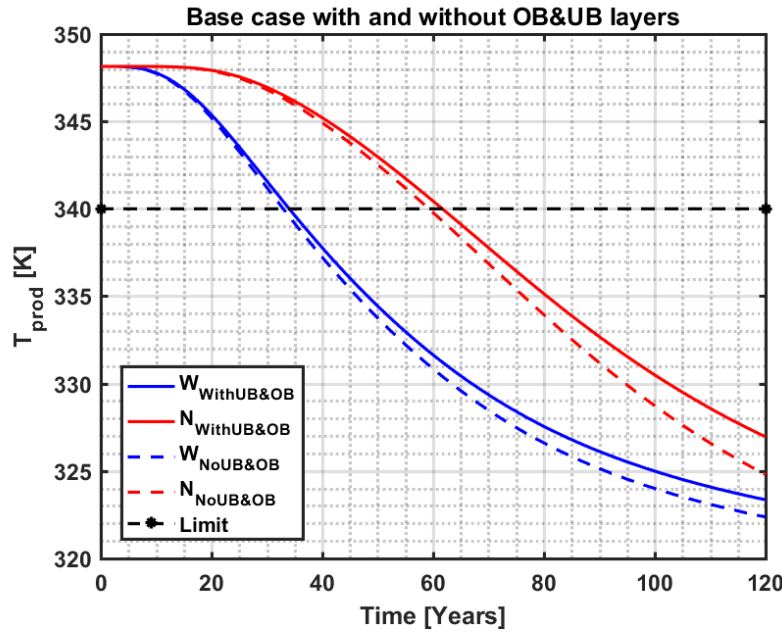
Figure 5.11: Plot shows the variation in the BT trajectories from the base case while ignoring over and under burden layers(OB and UB). No significant influence in the spread is observed.

Table 5-4: Comparison of the base case with the simulation results from ignoring OB and UB layers.

Furthermore, we could also conclude that the presence or absence of the under and overlain layers was not influential to the spread of the breakthrough.

Reducing Porosity and Permeability Ranges

As mentioned in the property modeling of the reservoir, available in section *3.2*, a beta distribution was used in order to populate the porosities. Using an empirical relationship obtained from the petrophysical analysis of core plugs **(eq.*3-1),*** the corresponding value of permeability was introduced. The **Figure 5.12** (A and B) shows the range of distribution of porosities within the sandstone members and the resulting permeabilities respectively. The porosities were observed to be ranging from 16% to 37% with almost 40% of the sand bodies having porosity values above 35%. Ideally, these ranges of porosities represent loosely consolidated sands and are very unlikely to be observed in a reservoir that is 2.3km deep. Hence the porosities were reduced to values ranging from 11% to 28% as shown in **Figure 5.12** (C). Due to the empirical relationship between the porosity and permeability, the range of the permeability also reduces significantly as observed in the **Figure 5.12** (D). Applying these changes to the base case, the model was simulated again. The results were almost analogous to the initial base case model with subtle variations in the breakthrough time. A possible explanation for these variations is the increase in pressures at the injection wells due to a reduction in the pore volumes (to maintain a constant rate of 4800m^3/day). This is evident from the pressure profiles of the base case model and the reduced porosity model **Figure 5.14**.
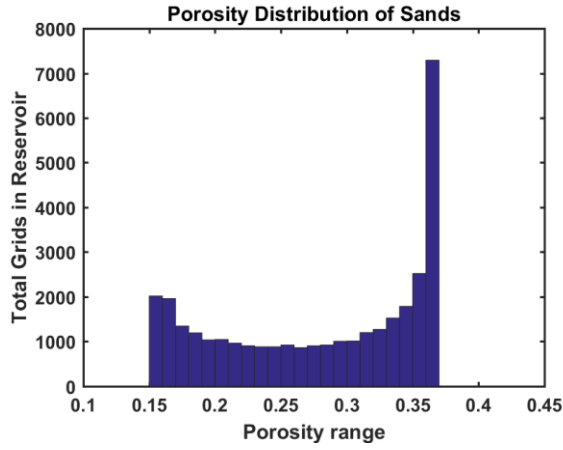
A. Base case porosity distribution in the reservoir
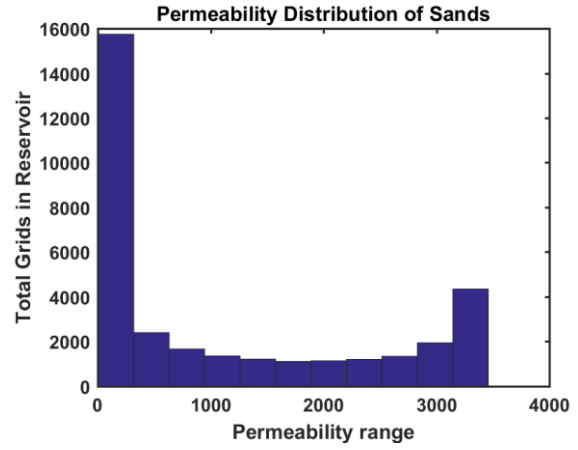
B. Base case permeability distribution in the reservoir
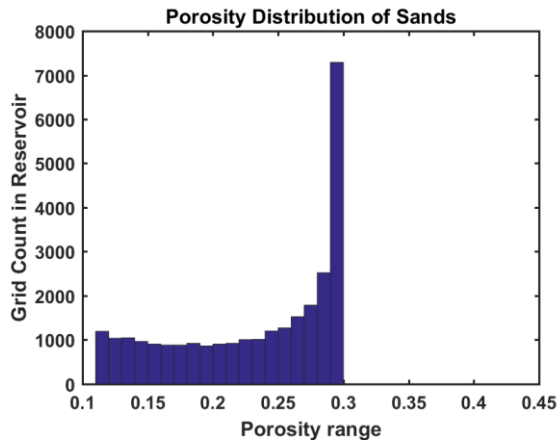
C. Porosity distribution In the reduced porosity model
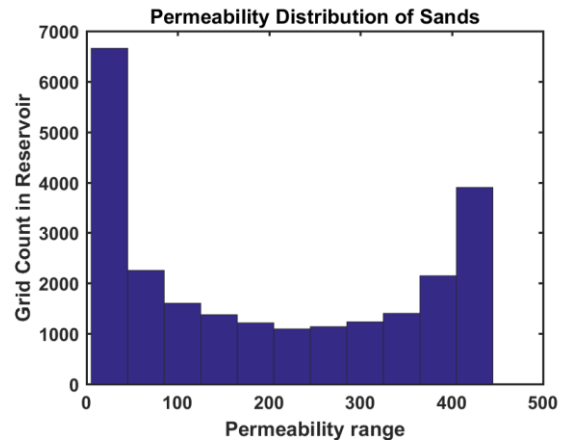
D. Permeability distribution in reduced porosity model

Figure 5.12: Reducing porosity distribution to a more realistic range
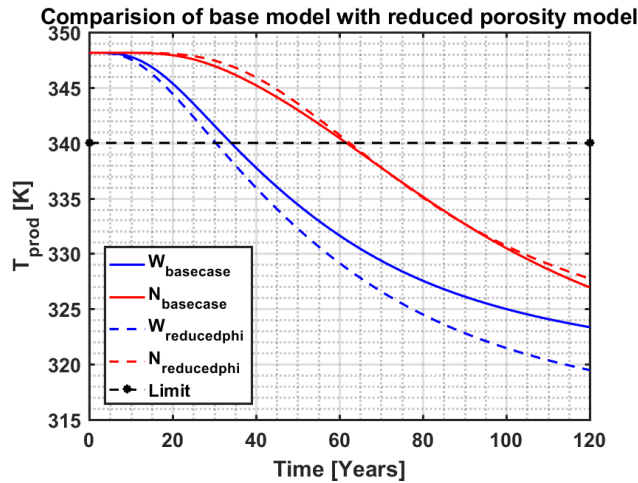
Figure 5.13: Plot shows the variation in the BT trajectories from the base case while reducing the porosity range
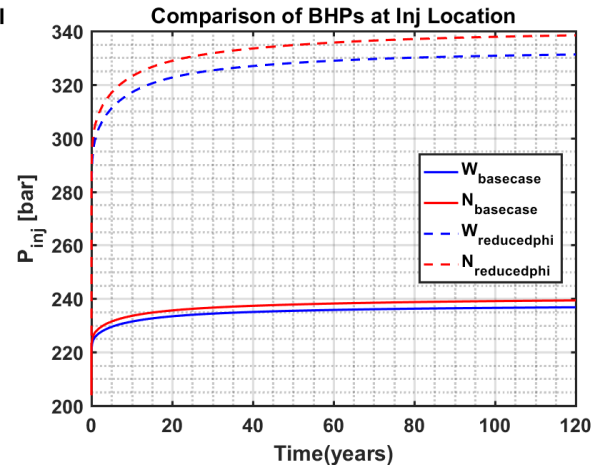
Figure 5.14: Plot shows a significant increase in the injection pressure profiles due to reduced porosity

Homogenous Sands and Shale

Base case [Permeability - mD]	
Sandstone	6-3500
Shale	5

Homogenous sands and shale model [mD]	
Sandstone	1600
Shale	5
Rates	4800 m³/day

Base case [Years]	
Spread	28

Homogenous sands and shale model [Years]	
Spread	34
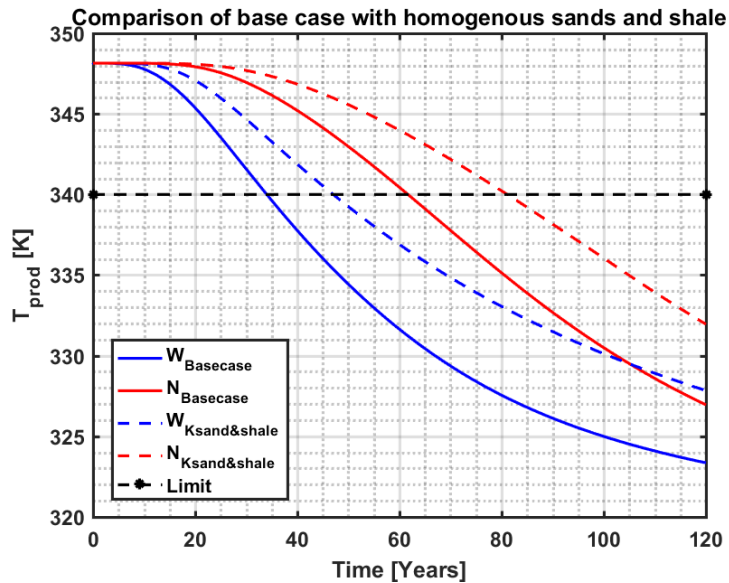
Figure 5.15: Plot shows the variation in the BT trajectories from the base case while constant permeabilities were assigned for sands and shale. No significant influence in the spread is observed

Table 5-5: Comparison of base case with the simulation results from assigning constant permeability for sands and shales

On the basis of the evidence currently available, it seems fair to suggest that none of the parameters presented so far have a dominant role in causing these large variations in the breakthrough time. In the present study, the issue under scrutiny is the effect of heterogeneity in the sandstone bodies. In the base model, sandstone bodies were highly heterogeneous. The heterogeneity of the sandstone bodies is now eliminated and a model with constant permeability for sands (1600mD) and another constant permeability value for shale (5mD) were generated. The results from the *Figure 5.15* provide confirmatory evidence that the heterogeneity of the sand bodies does not cause the large variations in the breakthrough time. However, the available evidence of having entirely different breakthrough times also suggests that the heterogeneous model is likely to travel a completely different flow path than the homogeneous model.

The easiest way to strengthen our argument that the spread in the breakthrough plots could likely be because of change in the flow path is to analyze the results of a completely homogenous model.

Assuming constant permeability for the entire reservoir

Comparison of base case with fully homogenous model

Base case [Permeability - mD]	
Sandstone	6-3500
Shale	5

Fully homogeneous model [m]	
Matrix	1600

Base case [Years]	
Spread	28

Fully homogeneous model [Years]	
Spread	0
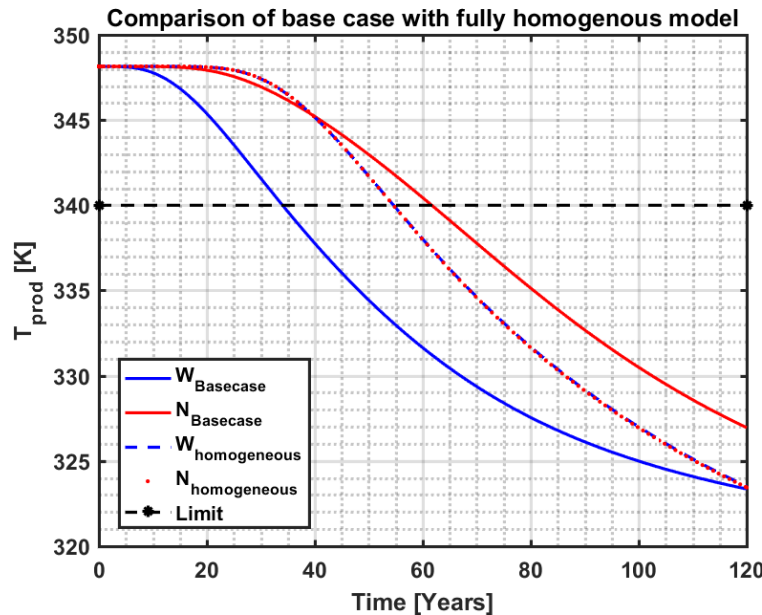
Figure 5.16: Plot shows the variation in the BT trajectories from the base case with the fully homogenous model. No spread was observed in a homogeneous model.

Table 5-6: Comparison of base case with the simulation results of a fully homogenous model

Here, a fully homogenous model was considered. In a fully homogenous model, the flow path would behave the same irrespective of the location of the well. Hence there would be no change in breakthrough time what so ever. Therefore in contradiction to the previous finding, the result obtained from a fully homogenous model bolsters the fact that the spread in the breakthrough curves is really dependent on the flow path of the fluid.

On these grounds, we can argue that a much more detailed analysis of the flow paths needs to be performed to really understand the concept of connectivity and thermal recharge.

5.4   Well performances and Streamlines

Well performance

The foregoing discussion implies the possible reasons for the spread in the breakthrough could be the variation in the flow path from each injection location. For this reason, a closer look into the flow path of the fluids was essential. In order to do so, initially, the well performances at each well location were analyzed. Before interpreting the results, we remind the reader that the reservoir model generated consists of 40 layers, each of which was perforated by both the injection and production wells. This enables us to gain information of the amount of water injected through each perforation of the injection well as well as the amount of water produced through each perforation of the production well. In this report, the measurements of the doublet's injection and production rates, at each perforated layer are termed as well performances.

Well performance at doublet locations north and west (N and W) of the base case model

Since the maximum differences in the reservoir's lifetime were observed when the doublet was relocated from the west to the north, the well performance at the two well locations was examined. These well performances were generated after a simulation time of 20 years. However since water is almost incompressible, we deal with pseudo-steady state conditions. Hence, the well performances were almost identical at every time step.
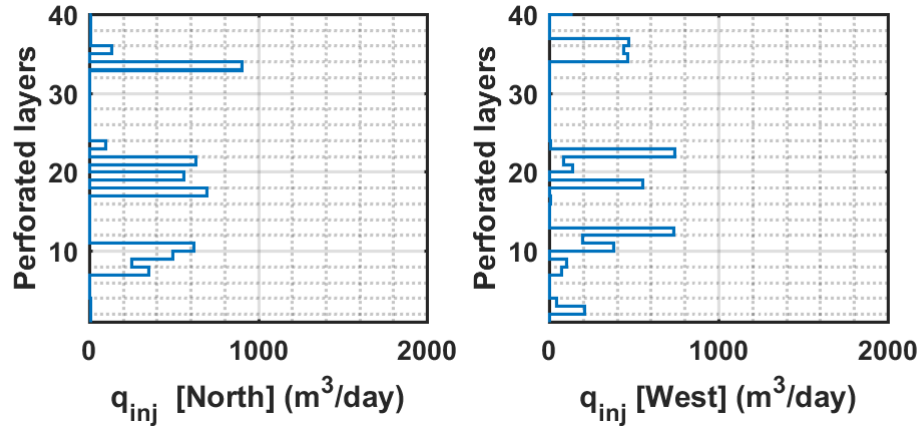
Figure 5.17: Well performances indicating the variation in the injection rates between well at north and west
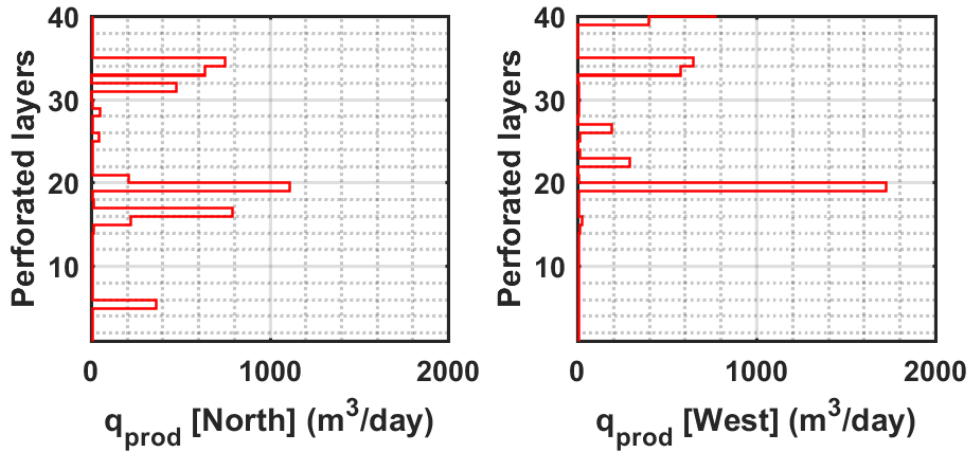
Figure 5.18: Well performances indicating the variation in the production rates between well at north and west

Figure 5.17 and **Figure 5.18** represent the comparison of the injection and production rates when the doublets were located at the north to when it was relocation to the east. The results show that the injection and production rates, along the perforations, for the two wells were vastly distinctive. It can be observed that the maximum injection rates for doublet located at the north is at layer 33 and layer 17 whereas the maximum injection rates for the doublet located at west was observed to be at layers 22 and 12. A possible explanation for this could be that the injection rates along each perforated layer would depend on the permeability of the perforated location. A high permeable location would allow greater injection and production rates and vice versa.

Relationship between permeability and well performance

In order to get a better insight, a comparison between the well performances and the associated permeability for each well was performed. *Figure 5.19* and *Figure 5.20* show the relationship between the injection and production well rates with the associated permeabilities when the well was located in the north. A comparison of the two results reveals a similar trend in the behavior of the rates with their associated permeabilities. For example, as was mentioned before, the maximum injection rates for well-N was at layer 33, this layer was also observed to have the maximum permeability of 3358mD.

These similarities put forward the view that the rate at which the flow takes place along each perforation really depends on their permeability. Similar comparison was made when the doublets were located at the west and the results were analogous (see appendix *A1. 4*, a detailed data set of the injection rates and permeability correlation for both the well locations are available in the appendix under section *A1. 5*). This means that just by relocating the doublets to the neighboring grid, the respective injection and production rates behave completely different due to the variations in the connected permeability.

Or in simpler terms, the injection rates are high when they are perforations are surrounded by high permeability region (sands) while the injection rates are low when they are surrounded by low permeability regions (shales).It is worth noticing that there is no direct correlation between the amplitude of the permeability and production for each perforation interval. It goes to show that there are various preferable paths between each of the injection and production wells which cause large sensitivity in the thermal breakthrough.
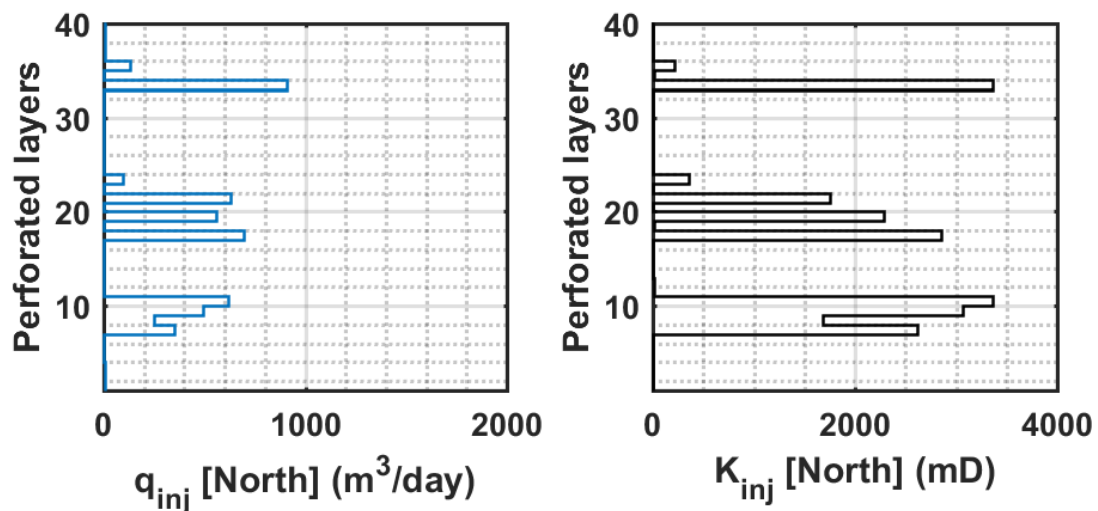
Figure 5.19: Illustration of similar characteristics between injection rates and associated permeabilities
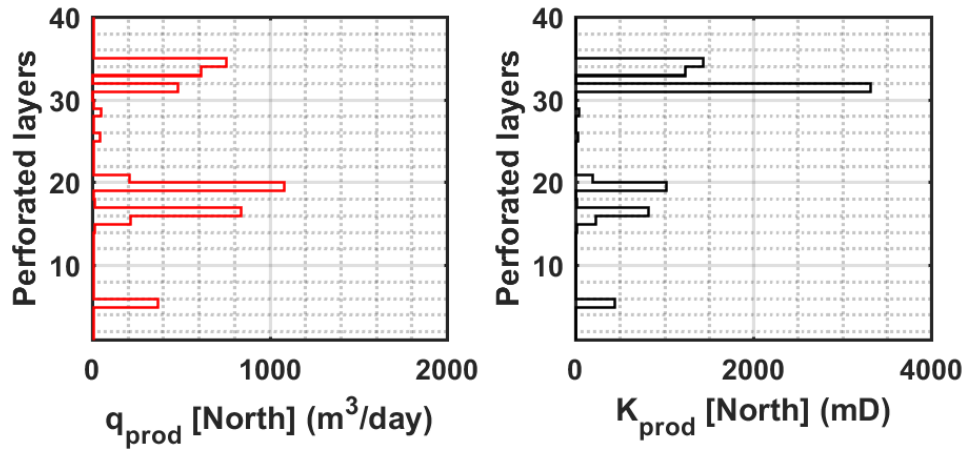
Figure 5.20: Illustration of similar characteristics between production rates and associated permeabilities

So far, it's only established that the injection and production rates were dependent on the associated permeabilities. Further research on the flow path between the wells can be done with the help of streamlines.

Streamlines

They are used to give us an intuitive understanding of the flow path. This, in turn, allows us to visualize the drainage regions associated with doublet wells.

Streamlines tend to connect paths that are tangential to the high velocities vectors in the model. A high velocity is mostly observed in locations that have high permeability and greater injection rates. This is because they are most likely the sandy regions. From the performances of both the injection wells (N and W), the layers which have the maximum rates were picked as shown in the table below. Streamlines were then generated and plotted for these layers. Each streamline was assumed to be representative of injection rates 200 m3/day. Thus the corresponding number of streamlines for each layer is distributed in *Table 5-7*.

West-Time 20years				North-Time 20years		
Perf. Layer (No.)	Inj. Rates (m3/day)	No. of Streamlines		Perf. Layer (No.)	Inj. Rates (m3/day)	No. of Streamlines
36	468	2		33	905	5
35	437	2		21	630	3
34	462	2		19	561	3
22	741	4		17	694	3
18	550	3		10	618	3
12	735	4		9	492	2
10	379	2		8	249	1
2	210	1		7	350	2

Table 5-7: Layers with maximum injection rates for well located in the north and west and their corresponding number of streamlines

Streamlines at 20 years at W location
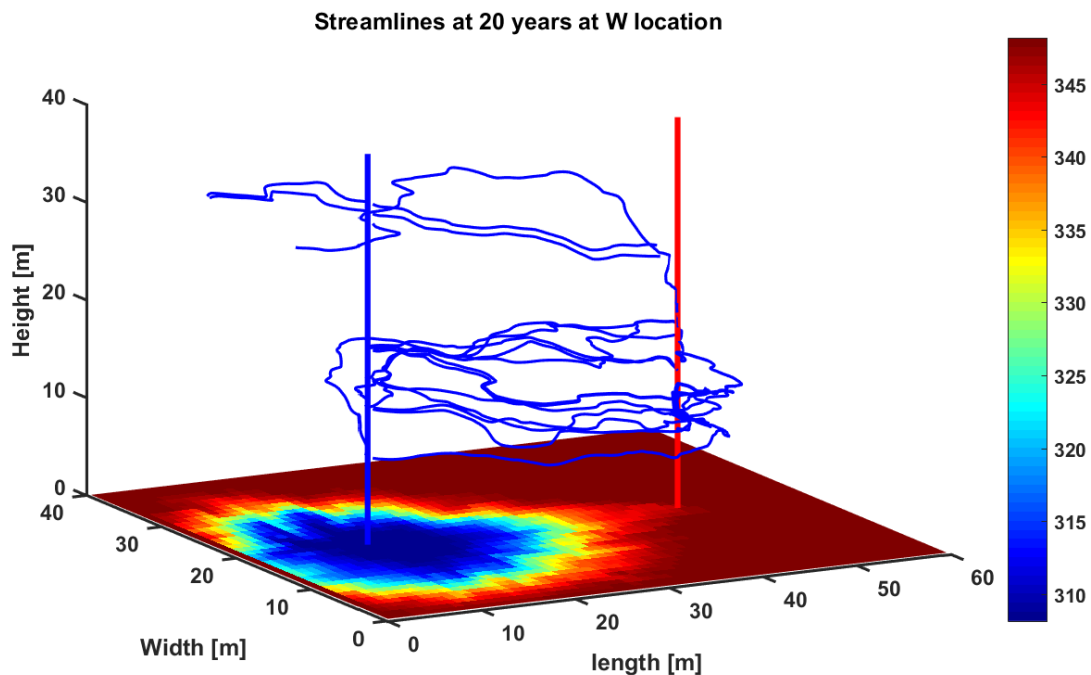
Figure 5.21: Illustration of flow path from the layers having high injection rates west location , at the base is the thermal front of the layer(22) that had the maximum injection rate.

Streamlines at 20 years at N location
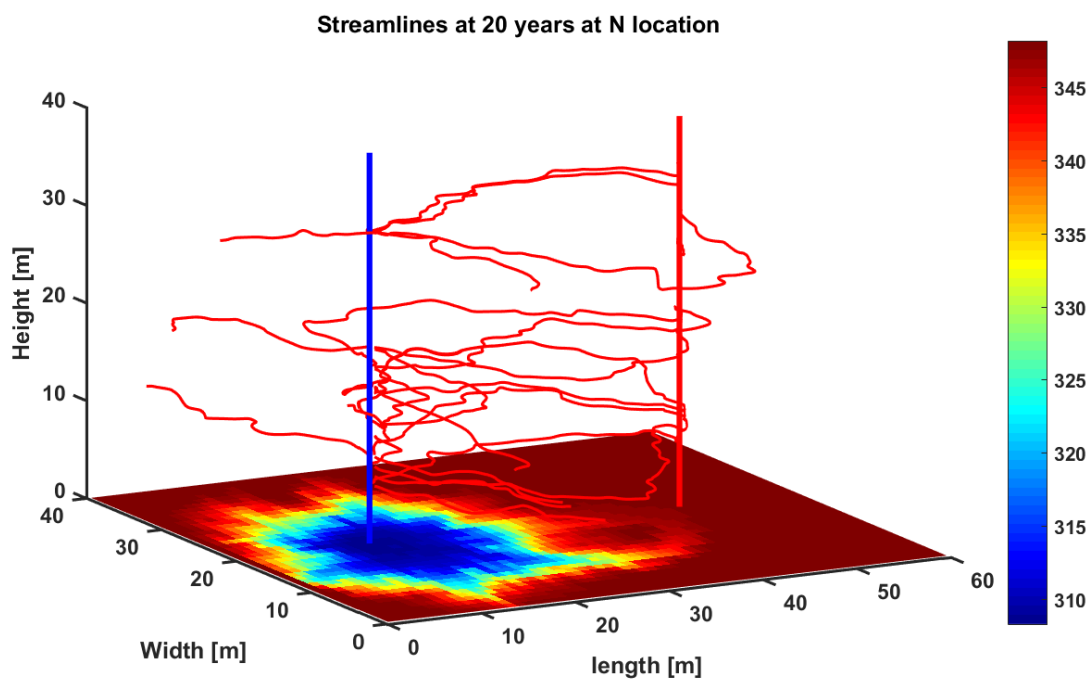
Figure 5.22: Illustration of the flow path from the layers having high injection rates north location, at the base is the thermal front of the layer(33) that had the maximum injection rate.

From the streamline *Figure 5.21* and *Figure 5.22*, it is clearly evident that the connectivity between the doublets for the two well locations (W and N) differs vastly. These findings lend support to the claim that just by relocating the wells a few meters away from each other, the wells communicate with the reservoir in completely different layers and have a very distinctive flow path.

A

B

C

D
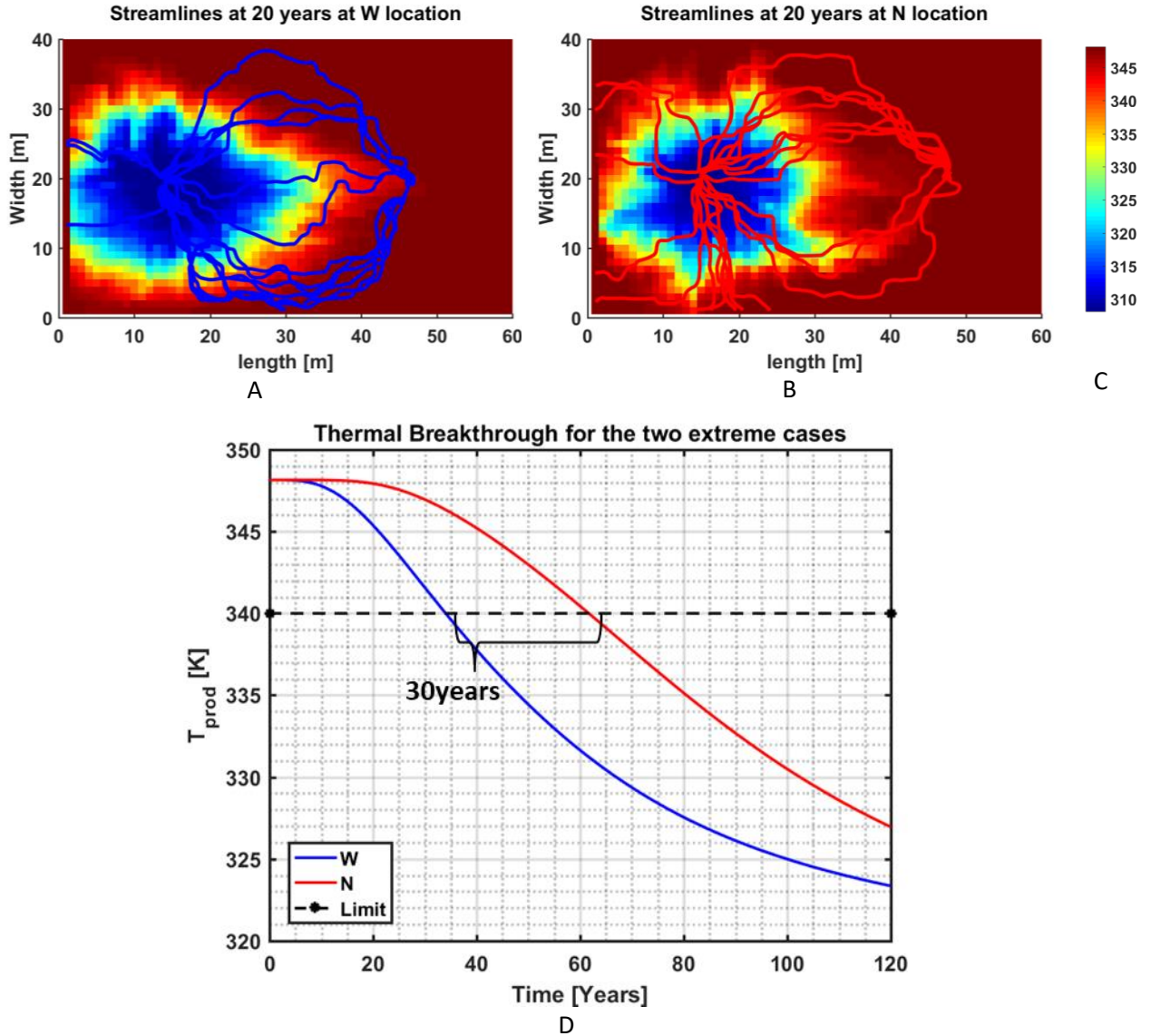
Figure 5.23: A,B are top views of the streamlined plot for wells W and N respectively. C represents the corresponding thermal breakthrough plots for both.

In *Figure 5.23*, a top view of the streamlines was plotted at both well locations. The base of the streamline plots represents the thermal front of the layer that had the maximum injection rates. It was observed that after 20 years of simulation time, the well located in the west has a more thermal front than the well located in the north. This is because when the doublet was located in the west, there is evidence of flow path taking shorter travel lengths while compared to the flow paths when the well was located to the north. Therefore we can expect an earlier breakthrough from the wells located in the west, while with the wells located in the north, the cold water would still require more

time to reach the production wells(as seen in the *Figure 5.23* A and B). Here we can conclude that it's not only the connectivity of the injection and production wells that play a vital role but also the connectivity within the reservoir that contribute significantly to the variation in the lifetime of the reservoir.

These results enable us to identify the cause of these large variations in breakthroughs when the wells are positioned at different locations within the reservoir. In order to get a deep insight of the influence of connectivity and thermal recharge, a couple of examples are portrayed to explain the concept of connectivity and the concept of thermal recharge in the next chapter.

6

Concept of connectivity and thermal recharge

6.1 Concept of connectivity

In order to illustrate the concept of connectivity, the same coarse model was used. But this time two doublet locations were arbitrarily chosen to perform simulations runs. The two doublets were named D1 and D2 and their location is shown in the *Figure 6.1.*
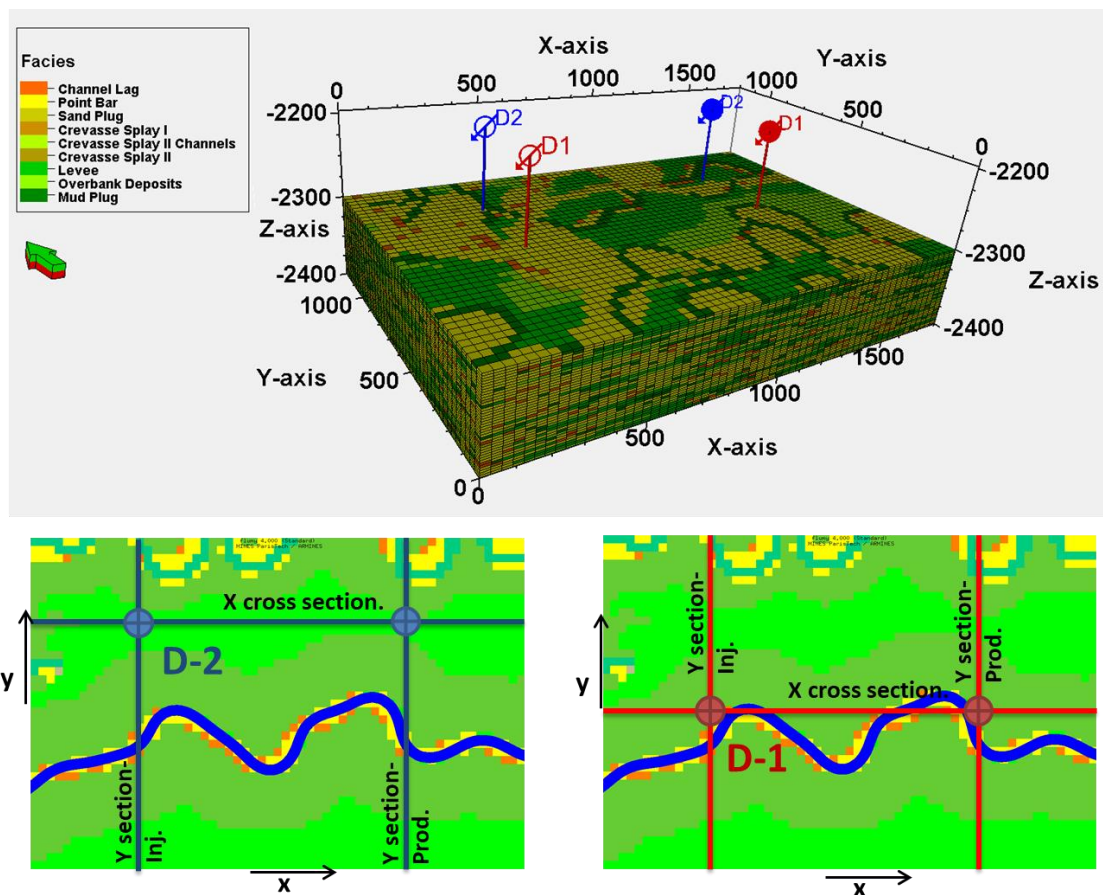
Figure 6.1: top: 3D view of the doublets placed. Bottom figure: top view of the two doublet locations and their cross sections

.

In order to predict the behavior of the breakthrough times for both these doublets, let's first look into the cross sections of both these doublet locations.

Y-Cross section at injector and producer locations
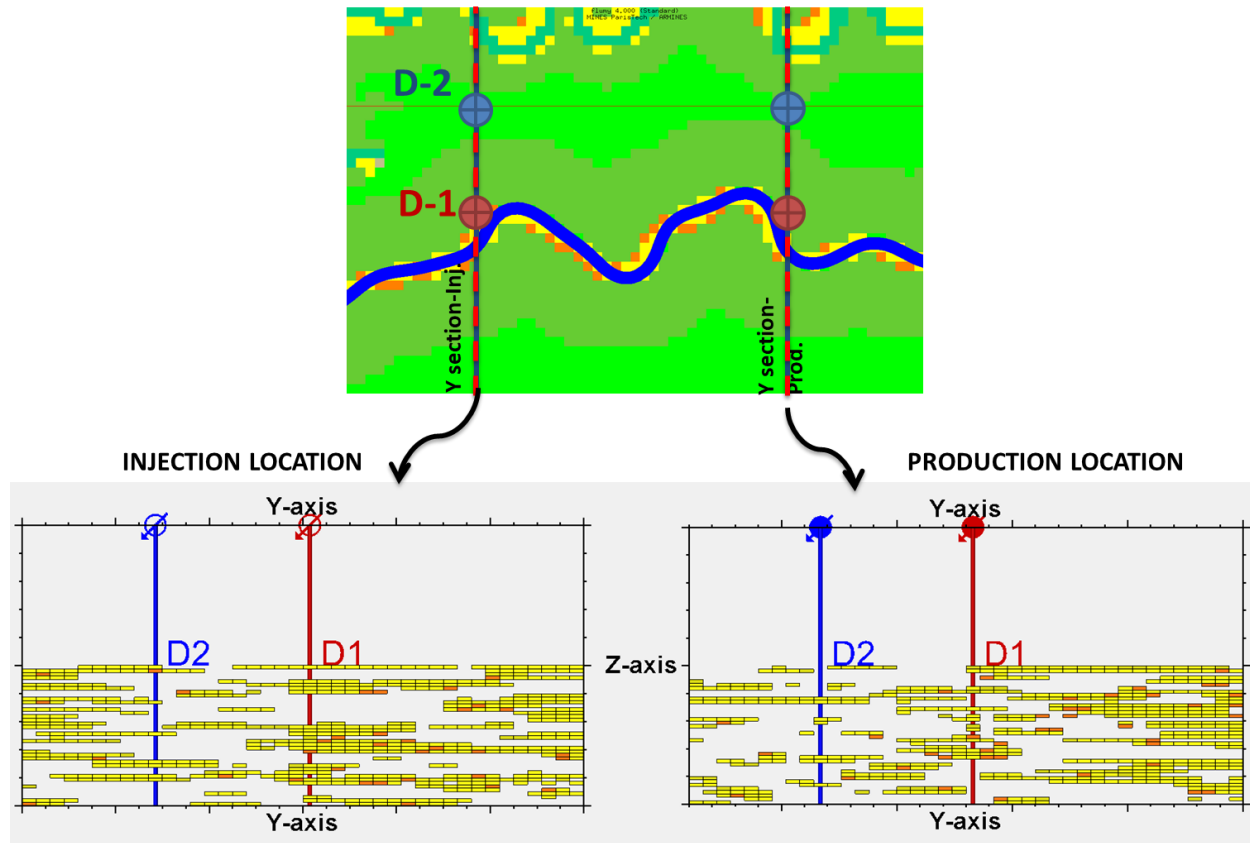
Figure 6.2: illustration of well connectivity with sandy layers along the injection and production locations of the two doublets D1 and D2.

In the above figure, only the sand layers are represented along the cross-section. This is because sands are highly permeable regions and the water flows through them easily. In both of these cross sections, D1 seems to penetrate through more sand bodies. This means that, during injection of water, D1 would allow the flow of water into several layers while D2 is bounded mostly by shale deposits and would have only a few layers through which the injection rates are high. To prove this the injection well performances of the doublets were plotted. The results seem to go in line with our hypothesis.

.
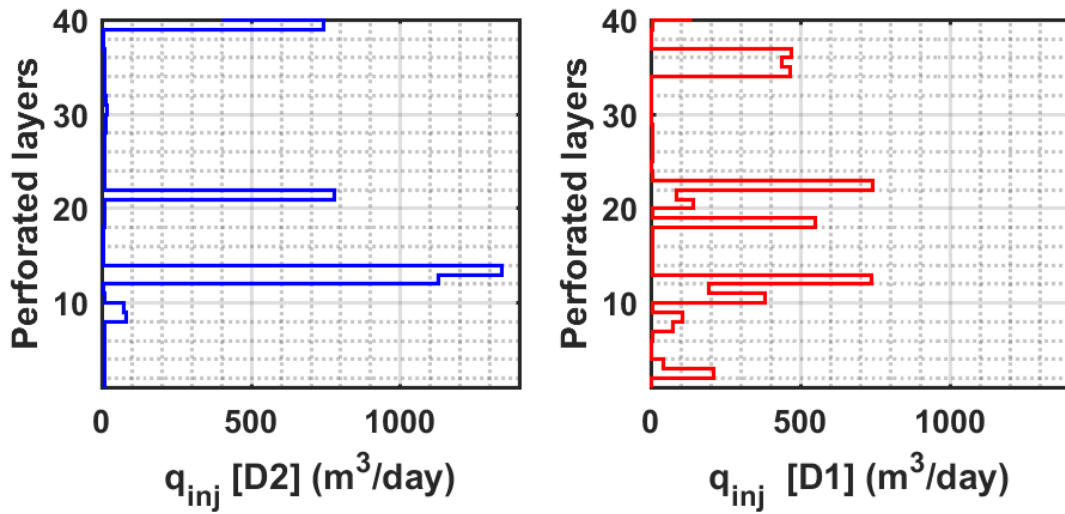
Figure 6.3: Illustration of poor connectivity with the sand layers in injection well location of D1 compared to that of D2.

Once it was understood that the doublets D1 has a better connectivity with the sand a layer along the injection well, it becomes essential to understand the connectivity between the injection and production wells. The straight line between injector and producer would be the shortest distance from the injected water to reach the producers. Hence a connectivity analysis was made between the injectors and producers of each doublet.

X-Cross section between injector and producer
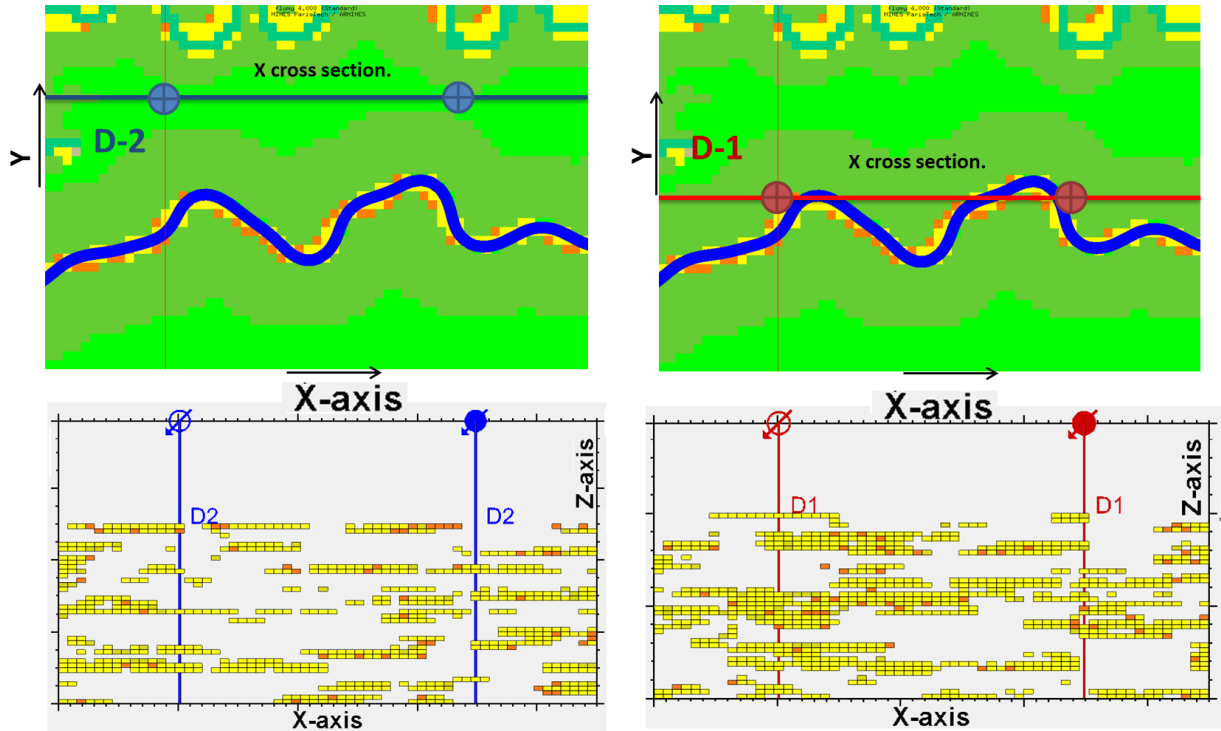
Figure 6.4: Connectivity analysis between injector and producer for doublets D1 and D2.

From *Figure 6.4* one can infer that there is very poor connectivity between the injector and producer of doublet D2 when compared to that of D1. These results provide evidence that water, injected through well D2, would never take the shortest route. Instead, due to large hindrance from the shale bodies, water would travel through longer flow paths before reaching the producer. Furthermore, due to the hindrance of several shale bodies, the fluid would have a reduced velocity as it flows through the reservoir, thus allowing it for a longer thermal recharge. The concept of thermal recharge will be explained in the upcoming section.

On the other hand, there seems to be a good connectivity between the injector and producer for doublet D2 (in the middles sections as seen in *Figure 6.4*). This means that some portions of the fluid, injected in the doublet D1, would travel through these short paths and reach the producer quickly, thus giving an early breakthrough.

From the injection well performance curves, layer 13 showed high injection rates for both the doublets (D1 and D2) and also the connectivity along the X and Y cross section seems reasonable hence a z slice of this layer is displayed in *Figure 6.5* in order to provide a better understanding of the overall connectivity.
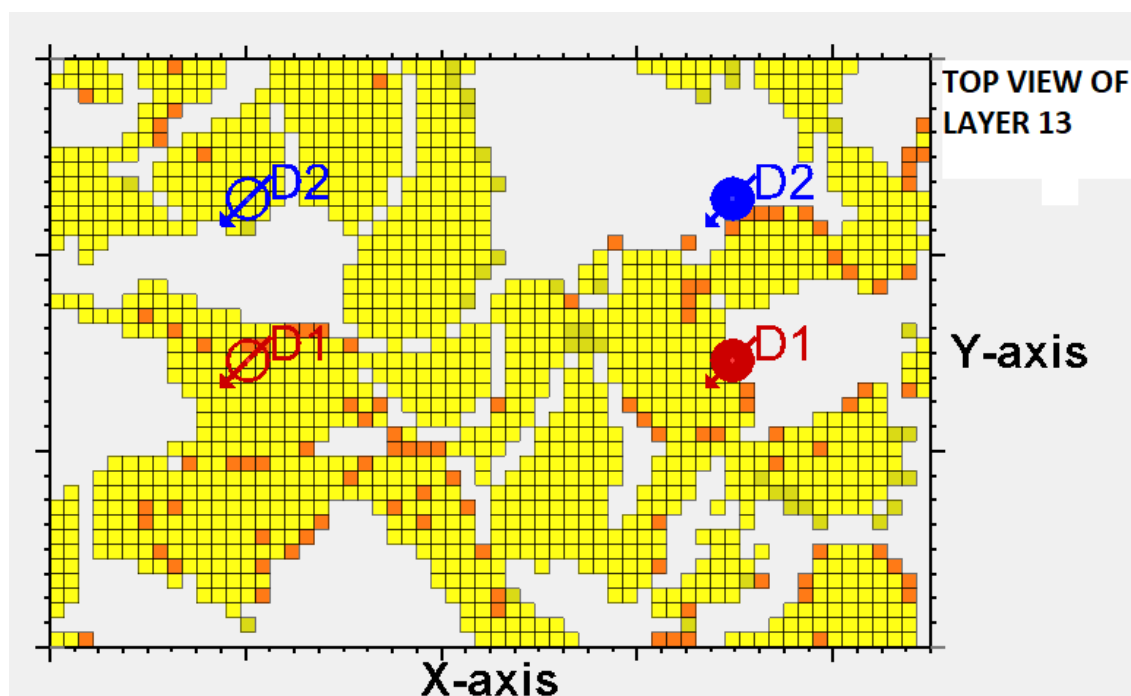
Figure 6.5: Z slice of layer 13 for both doublets D1 and D2

From the Z slice, it can be observed that although the doublet D2 has high injection rates in this layer, they lose connectivity within the reservoir quite quickly which means that, for the flow to reach from the injector to the producer they would have to travel a long tortuous path when compared to doublets D1. Since D1 shows a good connectivity and would not require the flow to travel a tortuous path to reach the producers. With all this evidence, one can easily predict that the thermal breakthrough would be earlier for doublet D1 compared to doublet D2. To finally see if our interpretations hold, streamlines and thermal breakthrough were plotted as seen in *Figure 6.6*.

If we now compare the streamlines of D2 with the Z slice in **Figure 6.6**, it's clearly evident that most of the injected water seems to flow through in the areas were the sand bodies are accumulated and, due to poor connectivity, most of the flow is hindered. That explains why the fluid travels more tortuous paths to reach the production well resulting in a delayed breakthrough.

To sum it up, the injection wells in the doublet D2 has poor connectivity with sand bodies compared to D1. This reduces its probability to have better connectivity between the injection and production. On scrutinizing the connectivity between the injection and production wells of the two doublets, it could be inferred that at doublet D1 had a worse connectivity than D2. Due to these connectivity issues, the flow paths take longer distances with lower velocities. This results in a much greater thermal recharge and thereby influencing a delayed breakthrough. So far, only the concept of connectivity and its influence on the flow path has been explained in detail. In the upcoming section, an attempt to explain the concept of thermal recharge will be made.
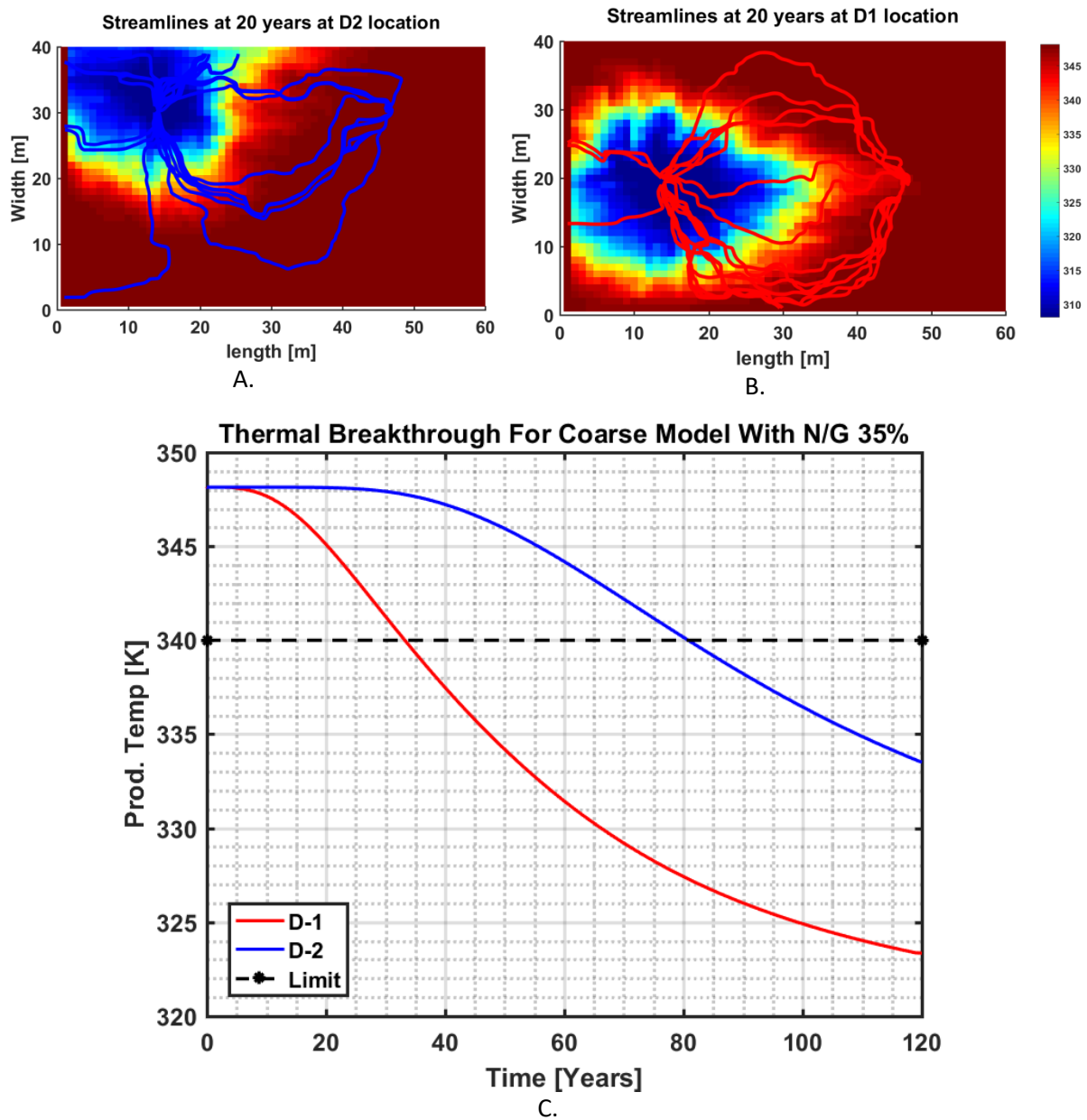
Figure 6.6: A,B are top views of the streamlined plot for wells D2 and D1 respectively. C represents the corresponding thermal breakthrough plots for both.

6.2   Concept of thermal Recharge

The concept of thermal recharge can be better explained with the help of a hypothetical 2D homogenous model. In the 2D model, we assume the first case to have a single channel between the doublets, while in the second case we assume that the well encounters two channels before the flow reaches the production well. The doublets were assumed to be at the same location for both the cases. (Note that this model is just a demo model and hence contributions of sand bodies from point bar and other geological depositions are ignored for simplicity and to explain the idea of the thermal recharge.)
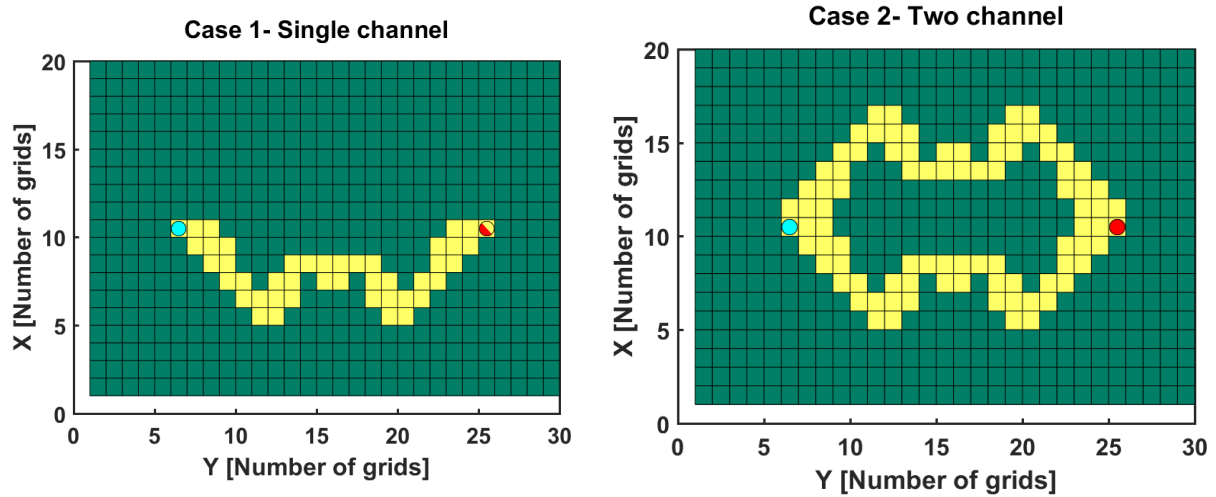
Figure 6.7: Illustration of the 2D model with (left) well encountering a single channel, (right) well encountering two channels.

All the thermal and fluid properties used in the model were kept the same for both the models and the injection and production rates were also maintained at a constant rate of 5m^3/day for both the cases. On running the simulation for both cases for 120 years the thermal breakthrough curves were obtained as shown in **Figure 6.8**. It can be observed that case 1 has an earlier breakthrough compared to case 2. As mentioned previously, connectivity does play a vital role in the way the breakthrough curves behave. However, the concept of thermal recharge also does go hand in hand with the concept of connectivity.
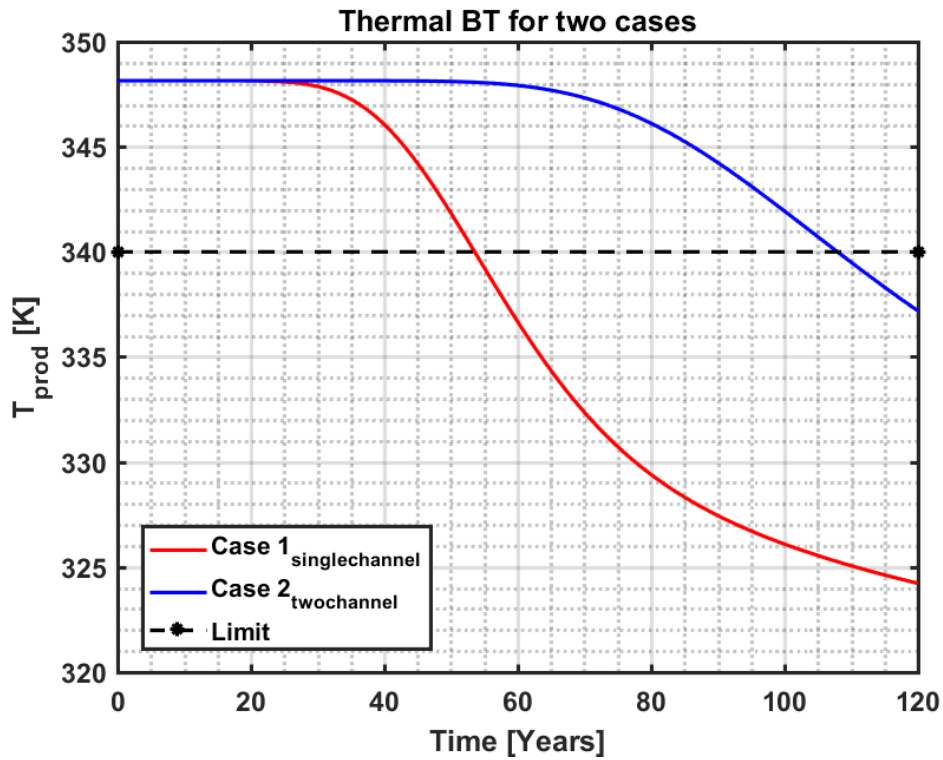
Figure 6.8: Thermal breakthrough comparison for Case 1 and Case 2

To portray the concept of thermal recharge pressure profiles along the reservoir were plotted for the two cases (*Figure 6.9*) followed by the streamlines for the two cases to take a closer look at the velocity of the fluids at various locations.(see *Figure 6.10*) .
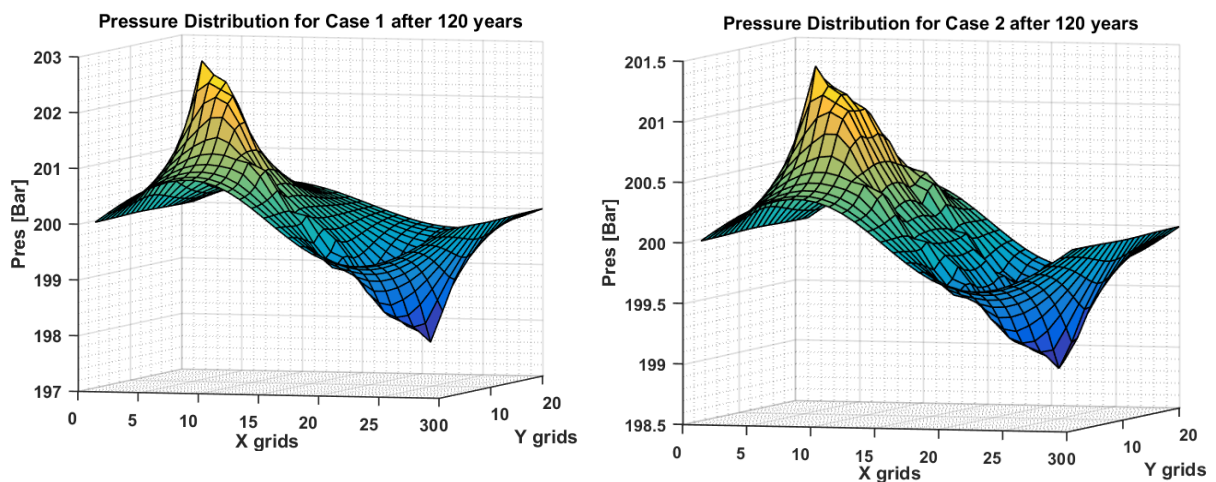
Figure 6.9: Pressure distribution along the reservoir for Case 1 and Case 2

The differential pressure for case 1 was almost twice that of case 2. A greater differential pressure would cause fluids to flow with a higher velocity. It was observed that the velocity at which the fluid flows for case 2 is much lower compared to the velocity at which the fluid flows for case 1. This is because at similar injection rates, the fluid branches into two channels in case 2, as a result of which the pressure along the grids of the reservoir would behave differently. (***Figure 6.10*** B). This in turn affects the velocity of the fluid flow. ***Figure 6.10*** also represents the thermal front of the fluid after 120 years. We can observe that the temperature drop at the production well for Case 1 is a lot more compared to the temperature drop for Case 2. One plausible reason for this is that as fluid travels with lower velocities, it has more time to recharge before it reaches the producers. This, therefore, results in a delay in the breakthrough of the cold water plume as observed in ***Figure 6.10 B.***

A.

B.
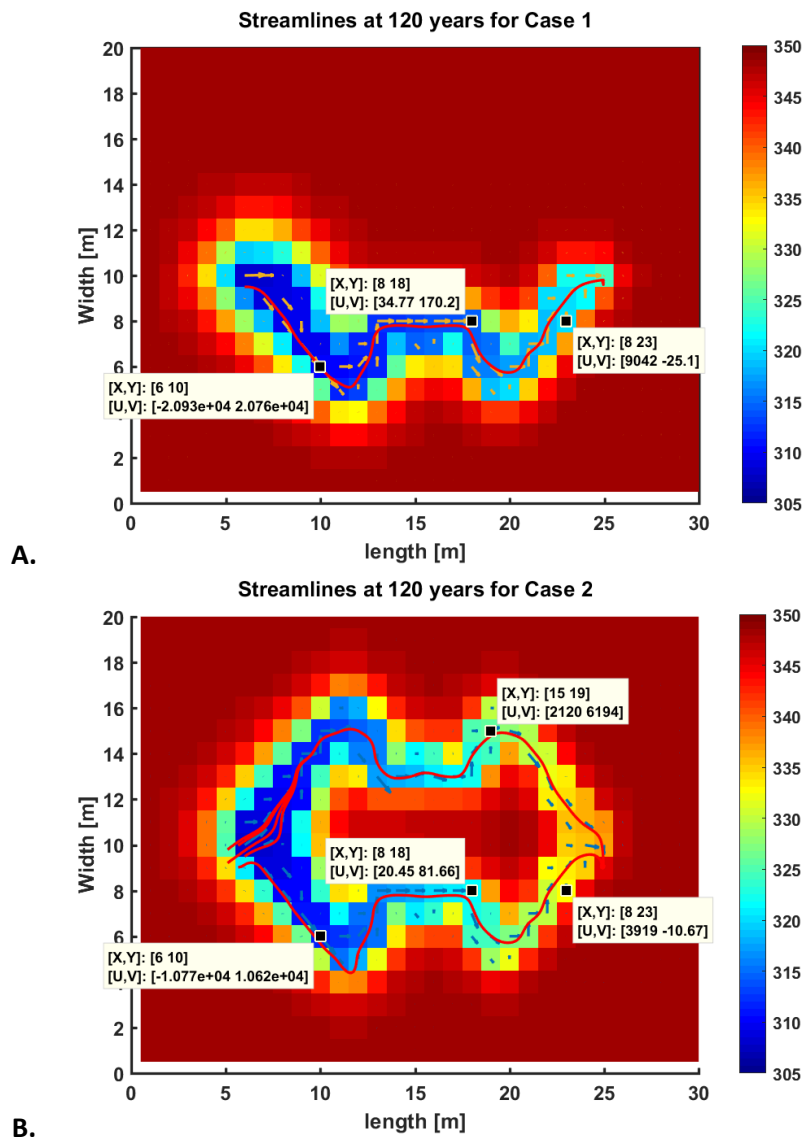
Figure 6.10: Streamline plots for the two cases and the velocities(U, V) at the various data points(X,Y). The velocities are not in SI units and were used to represent the variation in magnitudes.

6.3   Flumy modelling for narrow sand bodies

All the models generated so far over the course of this work consisted of wider sand bodies. This was done in order to improve the connectivity along the channel deposits. From the results obtained so far, one can easily predict that narrow sand bodies would not resolve the issue of large variations in breakthrough time. However, a new set of the model with N/G 35% (same N/G as the base case) was generated and the simulations were run in order to eliminate the ambiguity of the expected results. To run the simulation, nine neighboring coordinates roughly at the center of the model were chosen and the results of the same are illustrated in *Figure 6.11.* The visualization of the model can be found in the appendix

A1. *7.*

Base case- Wide Channel bodies [Years]	
Spread	28

Narrow Channel Bodies [years]	
Spread	54.5
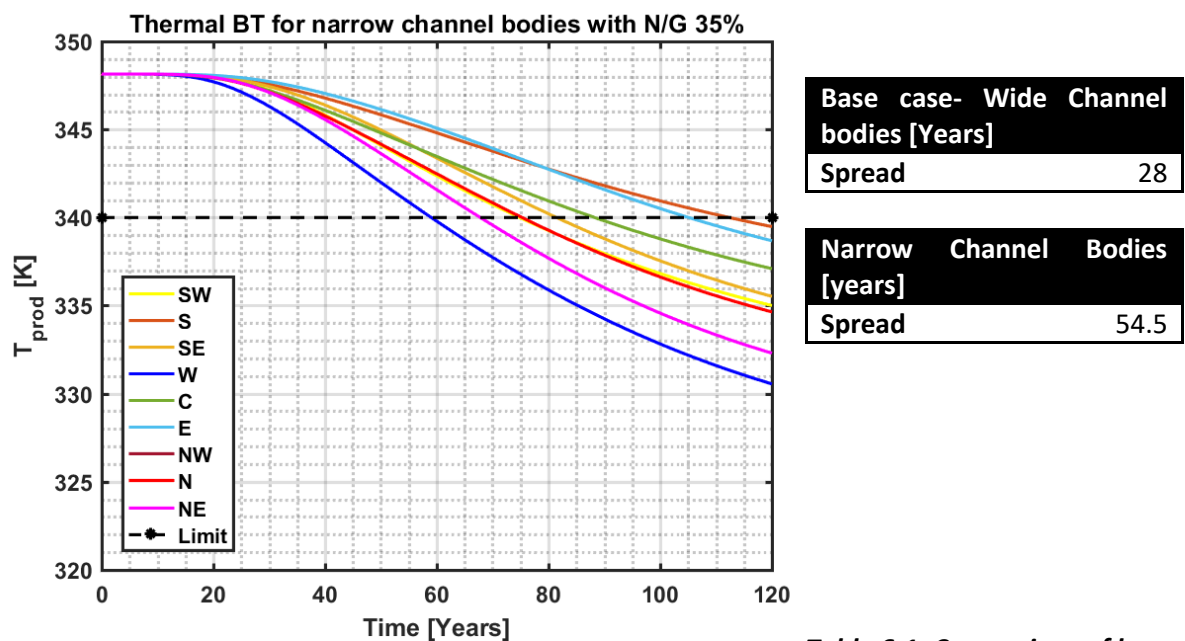
Figure 6.11: Plot shows the breakthrough curves for nine coordinates in a model consisting of narrow channel bodies.

Table 6-1: Comparison of base case with the simulation results narrow channel bodies

Needless to say, a more delayed breakthrough was expected due to poor connectivity between the sands. Furthermore, on scrutinizing the results, it can be observed that the spread between the two extreme breakthrough curves is greater. It seems evident that in order to create narrow channel bodies, the frequency of avulsions are increased, which means that the flow creates an entirely new path quite frequently. Hence, the connectivity between the channel bodies is lost and more importantly the chances of the well to encounter a completely different channel are high. This further supports our reasoning that the huge variation in the breakthrough is primarily because of the heterogeneity in which the channels are deposited. There could, however, be other possible explanations.

6.4 Thermal Breakthrough for Finer Model

The best way to compare results of the fine and coarse set of the model is to have the deposition sequence exactly the same in both of them. This would mean that there would be a better connectivity between the sand bodies deposited in fine scale model and hence could much likely reduce the spread in the breakthrough curves. However, Flumy restricts its users from generating the same set of the models with fine and coarse grids and hence such a comparison couldn't be replicated in this report. Nevertheless, an attempt in its visualization has been made and demonstrated as a figure in the appendix *A1. 6*.

In a broader sense, a fine scale model was generated that provides the same N/G as the coarse scale with the same input parameters as the coarse scale models. We still observe a large variation in breakthrough time although the relocated doublets are now even closer to each other. Needless to say, it's all about the connectivity of the sand bodies along the grid cells of the reservoir. There may be instances that even though the relocated well penetrates the same channel, over the length of the reservoir it would have branched to several other channels due to local avulsions. This would lead to an entirely different flow path which would then be influenced by a different thermal recharge. On these grounds, we can argue that irrespective of the scale of the model, there would still be indications of variation in the lifetime of the reservoir when the doublets are relocated. Furthermore, all the above-mentioned parameters were tested on both coarse and fine models with similar results.
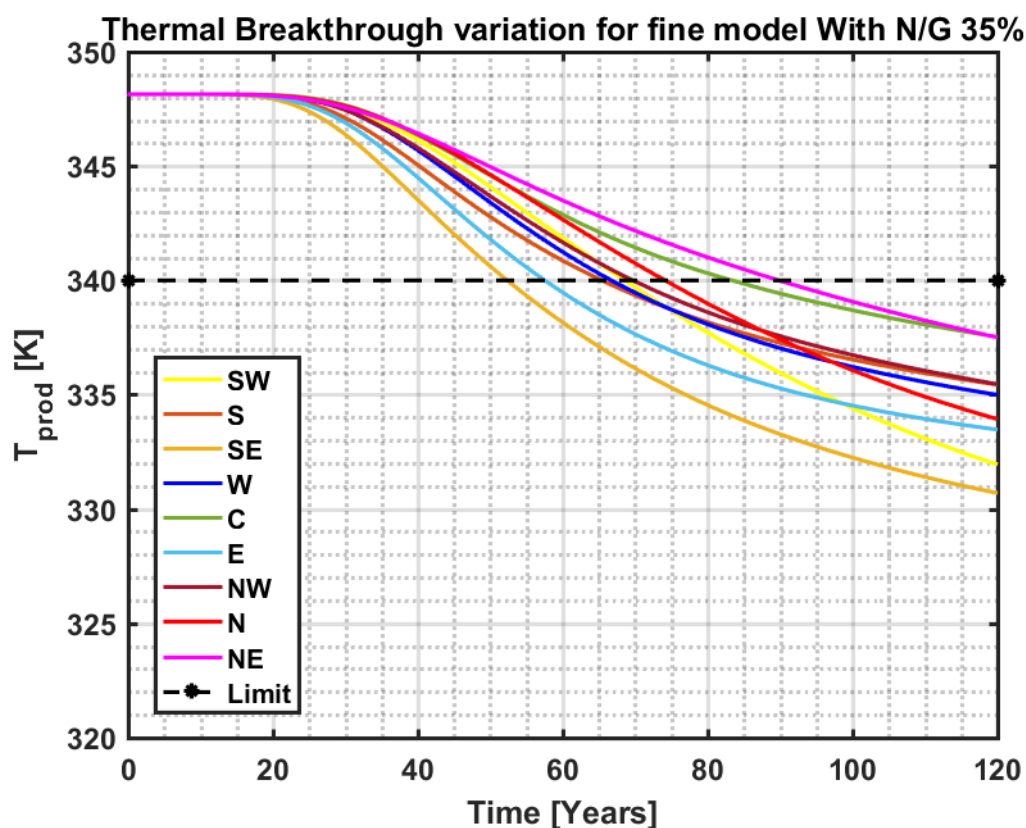
Figure 6.12: fine model with N/G 35% observed to have a spread of 37 years in reservoir lifetime between the two extreme

7

Upscaling Strategy

7.1 Various Upscaling Strategies to implement in a fine scale model

Upscaling is a method of generating a coarse scale model that closely resembles the properties that are present in its fine scale model. A successfully upscaled model is the one that is able to reproduce the same flow pattern as the fine scale model. However, the idea behind upscaling in this report is to analyze the breakthrough variations between the fine and coarse grid models. Two sets of models were created in the fine grid with grid sizes as shown in *Figure 7.1*. The models used in both the types were similar. The porosity of both the models was upscaled using volumetric averaging. For permeability, different schemes of upscaling were applied. This involved several combinations of arithmetic, harmonic and geometric upscaling.

TYPE 1: 3x3 UPSCALING   TYPE 2: 3x3x3 UPSCALING

FINE SCALE MODEL [180x120x40] TO COARSE SCALE [60x40x40]   *FINE SCALE MODEL [180x120x120] TO COARSE SCALE [60x40x40]*
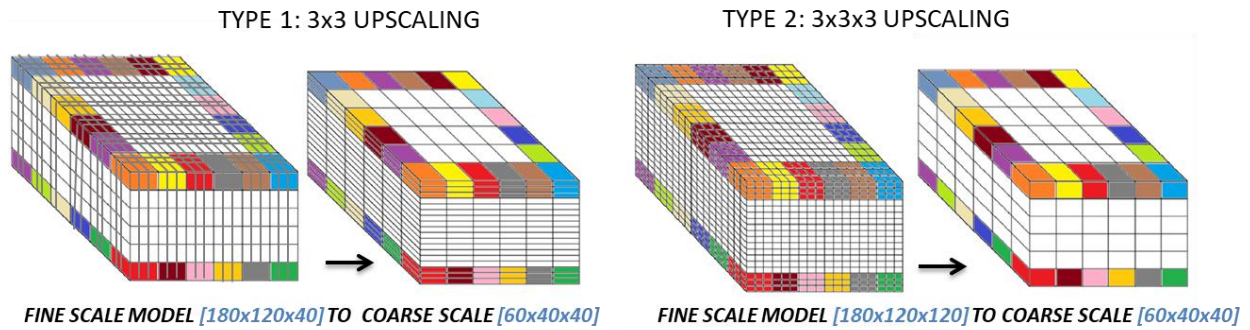
Figure 7.1: The two types of fine models upscaled.

Different averaging techniques

The most typical methods for permeability [k] upscaling are arithmetic, harmonic and geometric averaging. The equations used for arithmetic, geometric and harmonic averaging are as follows:

Arithmetic Mean [A]
$$A = \frac{1}{n}\sum_{i=1}^{n} k_i = \frac{k_1 + k_2 + \cdots + k_n}{n}$$

Geometric Mean[G]
$$G = \left[\prod_{i=1}^{n} k_i\right]^{\frac{1}{n}} = \sqrt[n]{k_1 k_2 \dots k_n}$$

Harmonic Mean[H]
$$H = \frac{n}{\sum_{i=1}^{n}\frac{1}{k}} = \frac{n}{\left[\frac{1}{k_1} + \frac{1}{k_2} + \cdots \frac{1}{k_n}\right]}$$

Ensembles of models were generated for coarse grids using several combinations of averaging techniques as shown in the workflow for upscaling permeability.
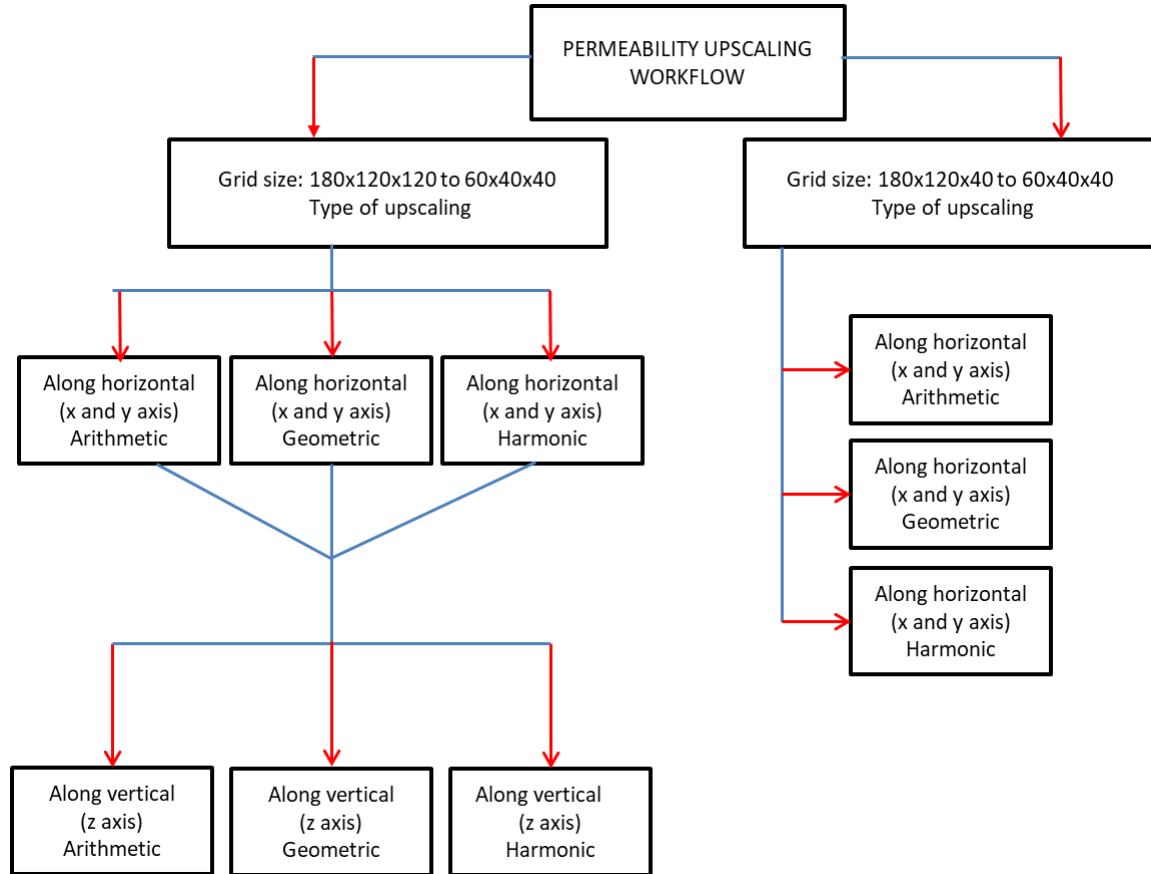
7.2   Discussion

From the results obtained there seems to be no compelling reason as to why one upscaling approach was better than the other. However, among the various upscaling schemes, it could be observed that geometric upscaling was a reasonable approach to upscale type 1 models (i.e. upscaling the coordinates along the x and y-axis).This result has been illustrated in **Figure 7.2 A,** where the doublets located at the center and west have been upscaled. Nevertheless, it was observed to give less effective upscaled model when the wells were located in the NW **Figure 7.2 B**. The results for harmonic and arithmetic upscaling for the same model with well locations west and center are available in the appendix **A1. 8**.

For models of type 2, it was observed that the best results after upscaling were obtained when the arithmetic averaging of the permeabilities were done along the horizontal and harmonic averaging was implemented along the vertical (**Figure 7.2 C)** However the consistency in these results was also questionable since they varied differently at the different well locations (**Figure 7.2 D)**. Other alternatives like global upscaling flow-based approach can be used, for a better accuracy and consistency in results. This approach is well explained in (47).
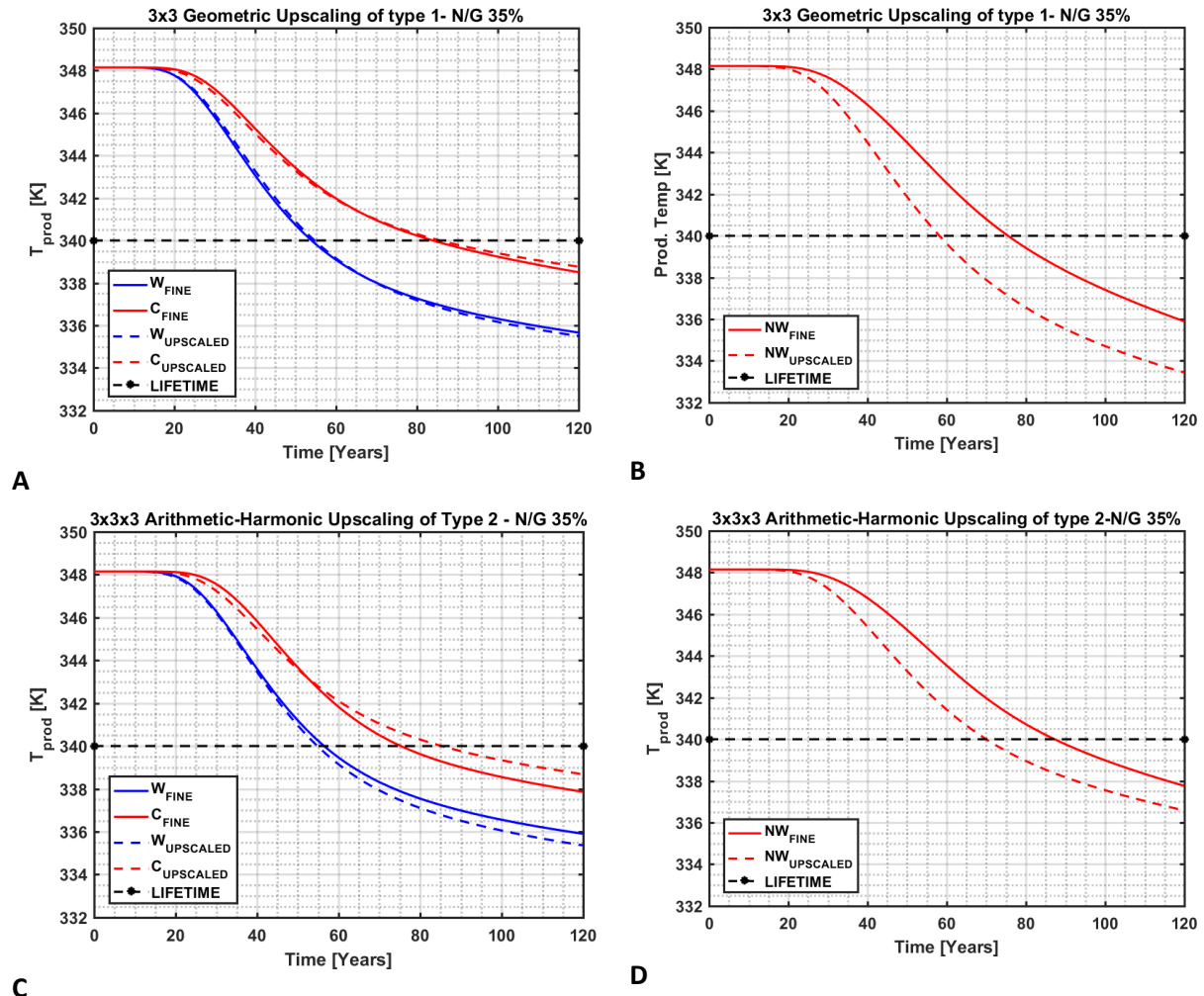
Figure 7.2: A. shows the upscaled results were quite accurate using the geometric upscaling technique; however, this approach didn't seem to yeild the same result for all well locations. Figure B shows huge variations when the wells are located at NW. C and D. shows the upscaled results for Arithmetic-Harmonic averaging of a 3 x 3 x 3 model
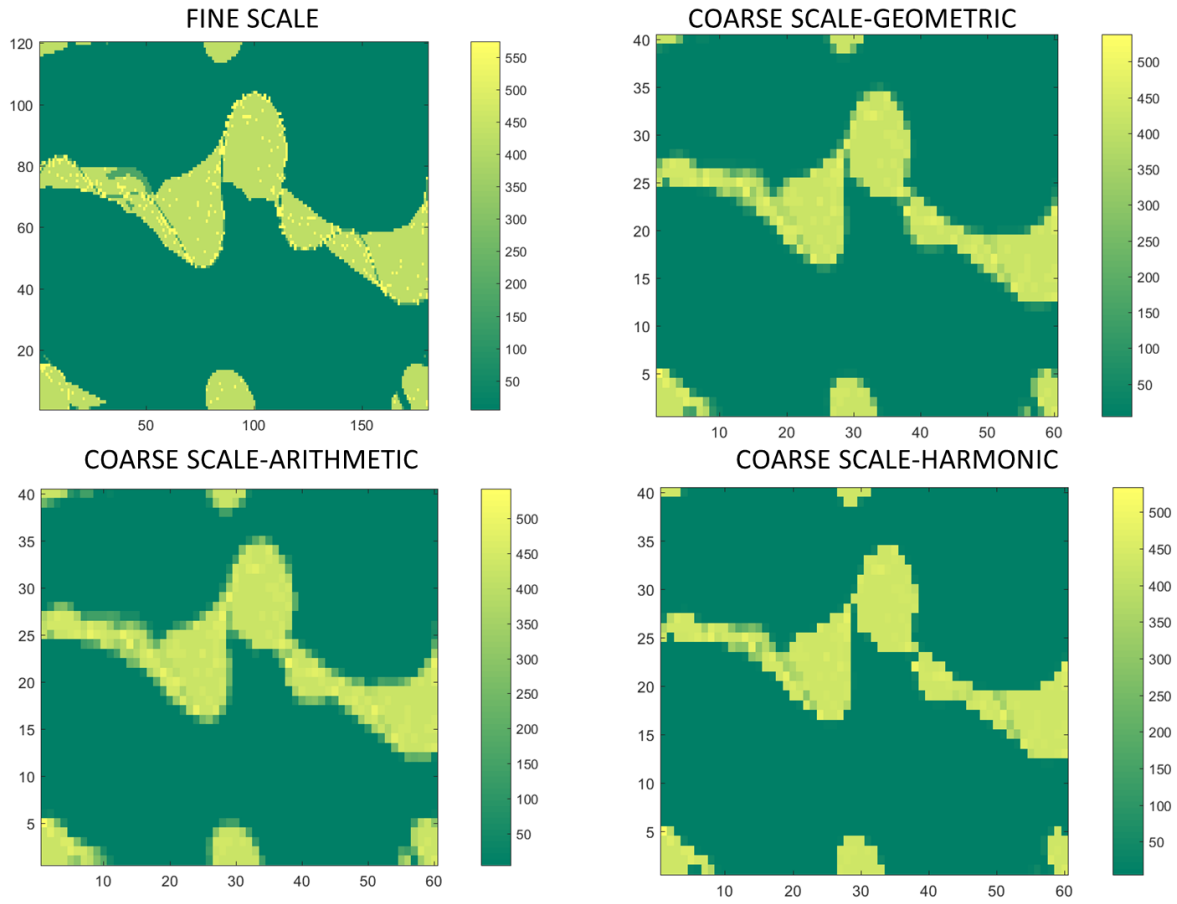
Figure 7.3: z slice of a permeability map(mD) of one of the layers in the 3D model picked for comparison of fine scale model with different upscaling techniques

From the above figure, it is quite evident that the upscaling strategies implemented in this report only introduced a loss of details within the sand bodies of each channel deposition; while preserving the geological architecture in which the channels deposited. What this meant is that the upscaling of fine to coarse grid might have caused subtle variation in the way in which the fluid flows from the injection well to the producers, thus resulting in slight variation in the upscaled results. However, on scrutinizing the plots in *Figure 7.3* it is apparent that even after upscaling the model, a large variation in the breakthrough times, for wells at different locations was observed. These results provide confirmatory evidence that the variation in breakthrough is vastly influenced by the heterogeneity in the geological deposition of channels.

8

Conclusion and Future Recommendations

The main target of this study was to investigate the reasons for a large variation/spread in the breakthrough curves at different well locations of a geothermal doublet. Based on the sensitivity analysis done for each parameter individually, it was found that they don't contribute to these variations. On comparing the fine and coarse scale models having the same N/G, it could be observed that the spread still persists. This means that, despite having a better connectivity along the sand bodies for fine scale models, the variations were still evident.

To identify the variation in the breakthrough curves on models with higher N/G, the breakthrough curves for a coarse and fine model each having N/G of 65% were examined (the plots can be found in the appendix *A1. 9*). It was observed that the spread in the breakthrough was still present. From this we conclude that the increase in connectivity of sand bodies also doesn't solve the issue. In order to check if the heterogeneity within the sand bodies played a vital role, the sand bodies were made completely homogenous. The results still indicated significant variation in the breakthrough.

Finally, on scrutinizing the well performances, along with the produced streamlines from each doublet location and looking into the cross sections of the generated model, it was evident that the cause of these large variations in thermal breakthrough was because of the heterogeneity in the way the channels are geologically deposited. It was observed that just by relocating the well to its nearest grid block, the injected cold water encounters an entirely different pathway. This resulted in a completely new streamline distribution compared to the distribution at the prior doublet location. The new flow path would therefore either travel a much shorter distance or a much greater distance than the flow path observed in the neighboring grid cell. The variation in flow paths, in turn, affects the way in which the cold front is thermally recharged along the reservoir, thereby having a completely different breakthrough time when compared to that of its neighboring doublet locations.

Since the major contributing factor for the large variations was due to the heterogeneity, the question now boils down to how realistic were the models generated from Flumy? The fidelity of the geological deposition, modeled by Flumy, remains questionable since it creates fluvial models purely based on the preset behavioral rule for the input parameters. One way to check on the geological deposition is to perform tests on models generated by more sophisticated process-based modeling software such as Delft3D.

Another point to check is the way the porosities and permeabilities are distributed. This study initially focuses on distributing them using a beta distribution method based on the data sets obtained from core plugs. It was later, however, accounted for, by generated models that honored the geological depositions (results of this are attached to the appendix under section. Since heterogeneity within the sand bodies was less influential compared to the depositional heterogeneity of the channels themselves, a more detailed analysis of the property distributions wasn't taken into account.

Finally, several upscaling strategies were implemented in an attempt to create a coarse scale model that accurately represents the breakthrough times of the fine scale models alongside understanding the actual reasons for any occurred differences. It was observed that certain upscaling strategies did provide quite accurate results for particular doublet locations. A more detailed approach for upscaling techniques such as global upscaling could be considered since it controls the flow by matching the fluxes of the fine and upscaled models along the interfaces. The literature (47) best describes the approach for global upscaling techniques.

A1. 1 Simplifying large number of facies into only sands and shales

A.

B.
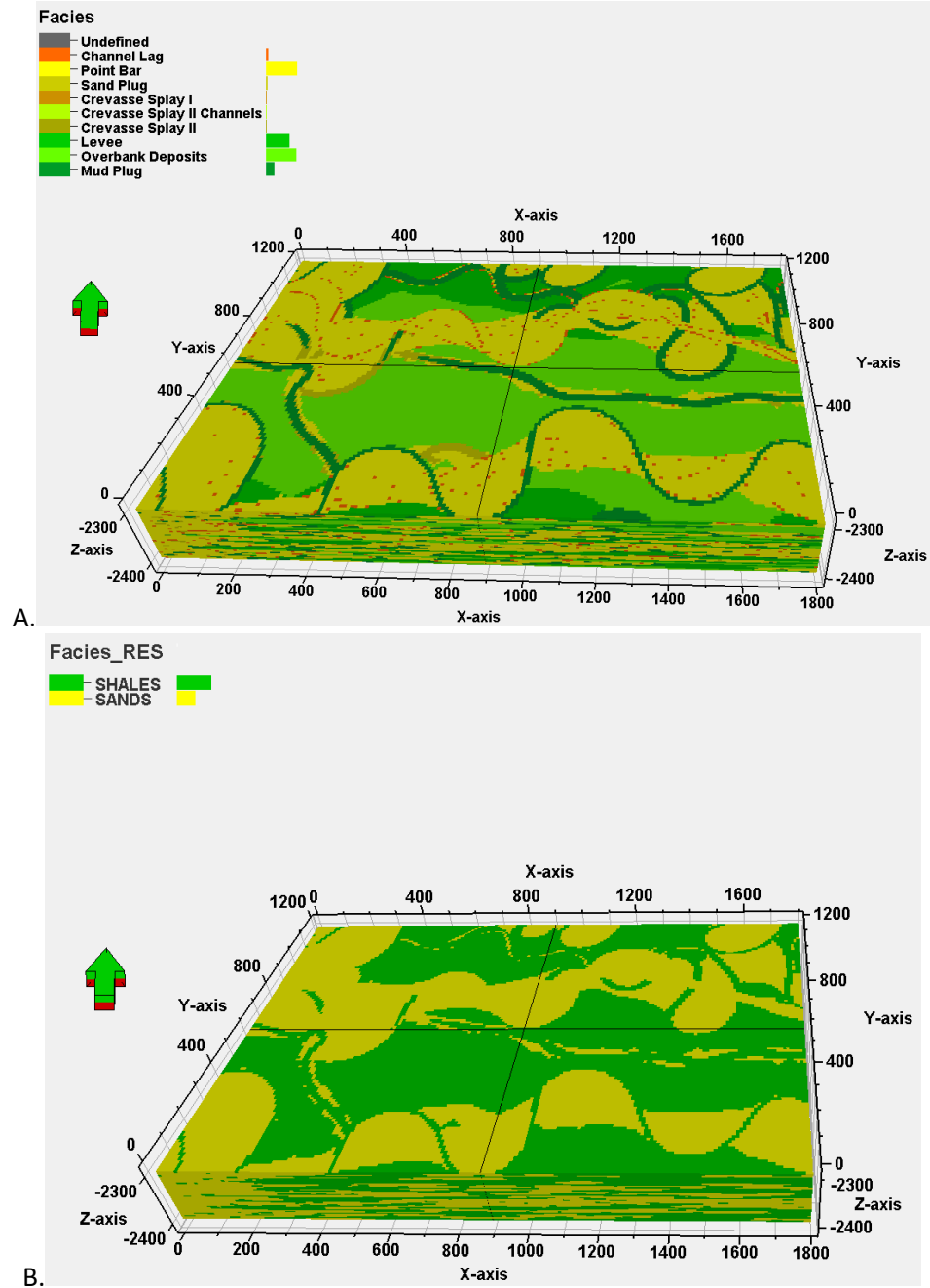
FigureA. 1 : A Fine scale model visualization from all the facies to B) only sands and shales

APPENDIX

A1. 2 Results and Discussion

Verification of modified model with original model:

| Parameters	ORIGINAL MODEL Value	TEST MODEL Value
Reservoir Dimension	2km x 1km x 50m	1.8km x 1.2km x 100m
Number of grids with data points	100 x 50 x 20	100 x 50 x20
Grid Size	20m x 20m x 2.5m	18m x 24m x 5m
Reservoir Volume	$1e^8$ m^3	$2.16e^8$ m^3
Injection and Production rates	2400 m^3/day	5184 m^3/day

Table: Simulation parameter comparison between the original and test model

Since the original model consisted of 100 x 50 x 20 data points, the only way to modify the reservoir dimension was by changing the grid size to 18m x 24m x5m. This provides dimensions of the reservoir model used in our study (i.e. 1.8km x 1.2kn x 100m). Please note that the reservoir is now twice as thick resulting in almost twice the volume compared to the original model. To account for this injection and production rates were initially increased to $q = 5184m^3/day$.
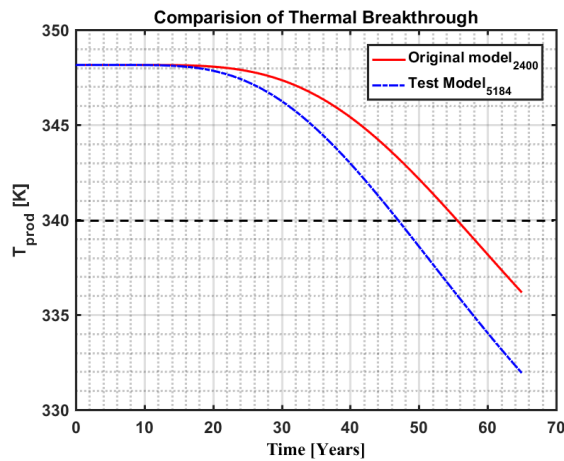
Figure A.2: Production Temperature of original and test model at injection rates 5184 m3/day
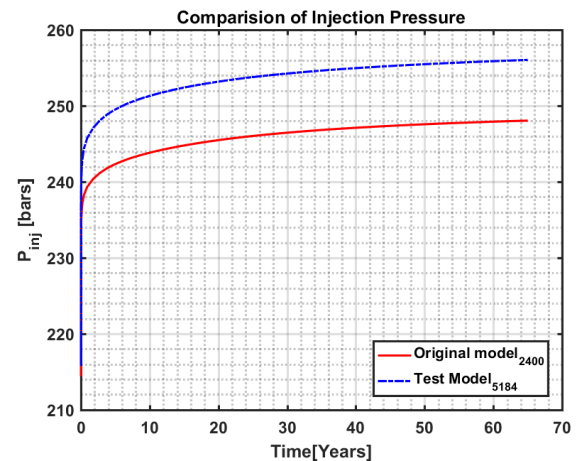
Figure A.3: Injection pressure of original and test model at injection rates 5184 m3/day

On comparing the test model with the original model we observe that the prior model has an early breakthrough **Figure A.2.** This is because an increase in thickness would result in an increase in depth of the model. These further results in an increase in the injection pressure in order to maintain a constant flow rate of 5184 m^3/day, as observed in **Figure A.3**. As the pressure increases the velocity with which the fluid flows also increases, thereby resulting in an early breakthrough. In an attempt to compensate for it, several flow rates were tested and it was observed that with an injection and production rate of 4800 m^3/day provided the breakthrough that replicates the original model and hence an injection and production rate of 4800 m^3/day was chosen. On logical grounds, there is no compelling reason to argue that the test model having rates of 5184 m^3/day is inaccurate. However, injection rates of 4800 m^3/day were chosen to enable a good match between the test and the original model, as seen in **FigureA. 4.**
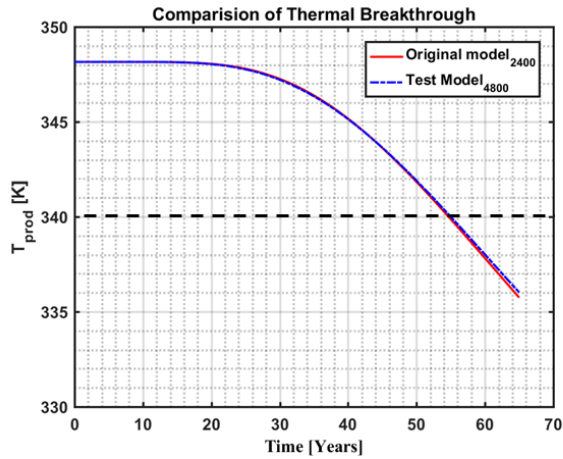
FigureA. 4: Thermal Breakthrough of original and test model at injection rates 4800 m3/day
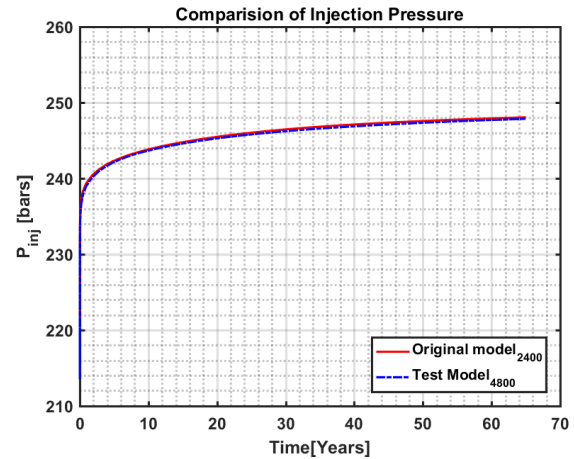
FigureA. 5: Injection pressure of original and test model at injection rates 4800 m3/day

A1. 3 Sensitivity of over and under burden layers for the model with reduced thickness and a flow rate of 4800 m^3/day
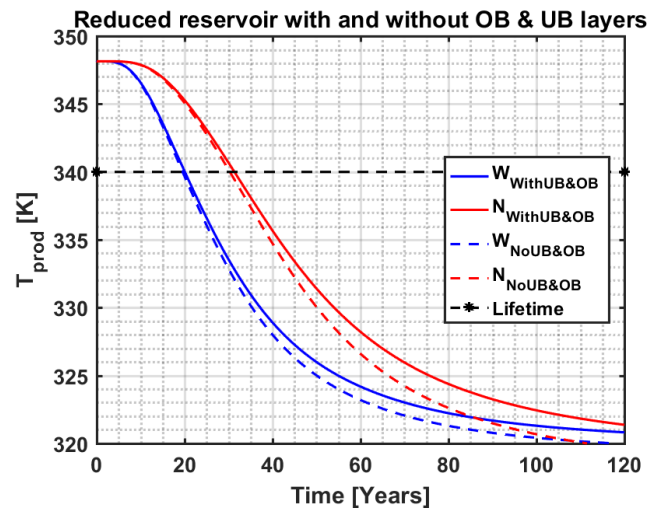
FigureA. 6: Reduced thickness model with and without UB and OB layers and flow rate of 4800m3/day

The above figures indicate that the breakthrough curves are not deeply influenced by the presence of over and under burden layers.

A1. 4 Well Performance and its permeability relationship for wells located in the West.
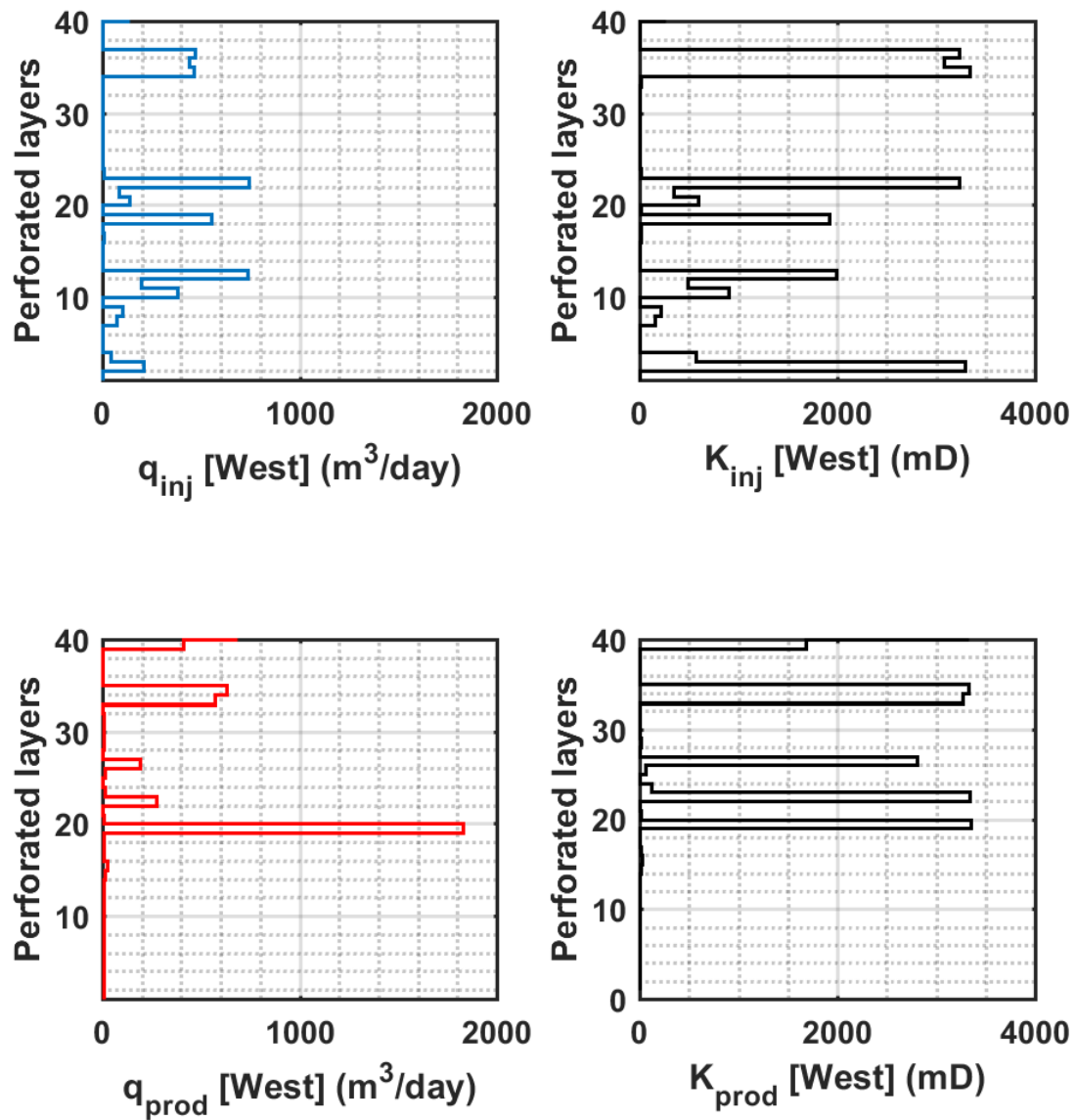
FigureA. 7: Production profiles compared with perm for doublet located at West

A1. 5 detailed data set of the injection rates and permeability correlation for both the well locations

North-Time 60years			West-Time 60years		
Perf. Layer (No.)	Inj. Rates (m3/day)	Perm Inj (mD)	Perf. Layer (No.)	Inj. Rates (m3/day)	Perm Inj (mD)
40	13	15	40	137	261
39	4	5	39	2	5
38	4	5	38	2	5
37	3	5	37	1	5
36	3	5	36	468	3228
35	129	217	35	437	3080
34	3	6	34	462	3334
33	905	3358	33	1	7
32	2	5	32	1	5
31	2	5	31	2	5
30	2	5	30	2	5
29	2	5	29	2	5
28	2	5	28	2	5
27	2	5	27	2	5
26	2	5	26	2	5
25	2	5	25	2	5
24	2	5	24	2	5
23	93	358	23	3	10
22	2	5	22	741	3226
21	630	1746	21	85	346
20	2	5	20	138	596
19	561	2281	19	3	8
18	2	7	18	550	1919
17	694	2856	17	3	6
16	1	5	16	5	10
15	2	5	15	2	5
14	2	5	14	2	5
13	2	5	13	2	5
12	3	9	12	735	1990
11	2	8	11	193	484
10	618	3356	10	379	900
9	492	3068	9	2	5
8	249	1685	8	102	217
7	350	2612	7	73	157
6	1	5	6	2	5
5	2	5	5	2	5
4	3	5	4	1	5
3	3	5	3	39	569
2	3	5	2	210	3285
1	3	5	1	1	5

Well injection rates and associated permeability values for wells located in North and west

A1. 6 Concept of connectivity and thermal recharge: *Ideal way to compare fine and coarse scale model*

ACTUAL FLOW PATH

COARSE SCALE MODEL

FINE SCALE MODEL
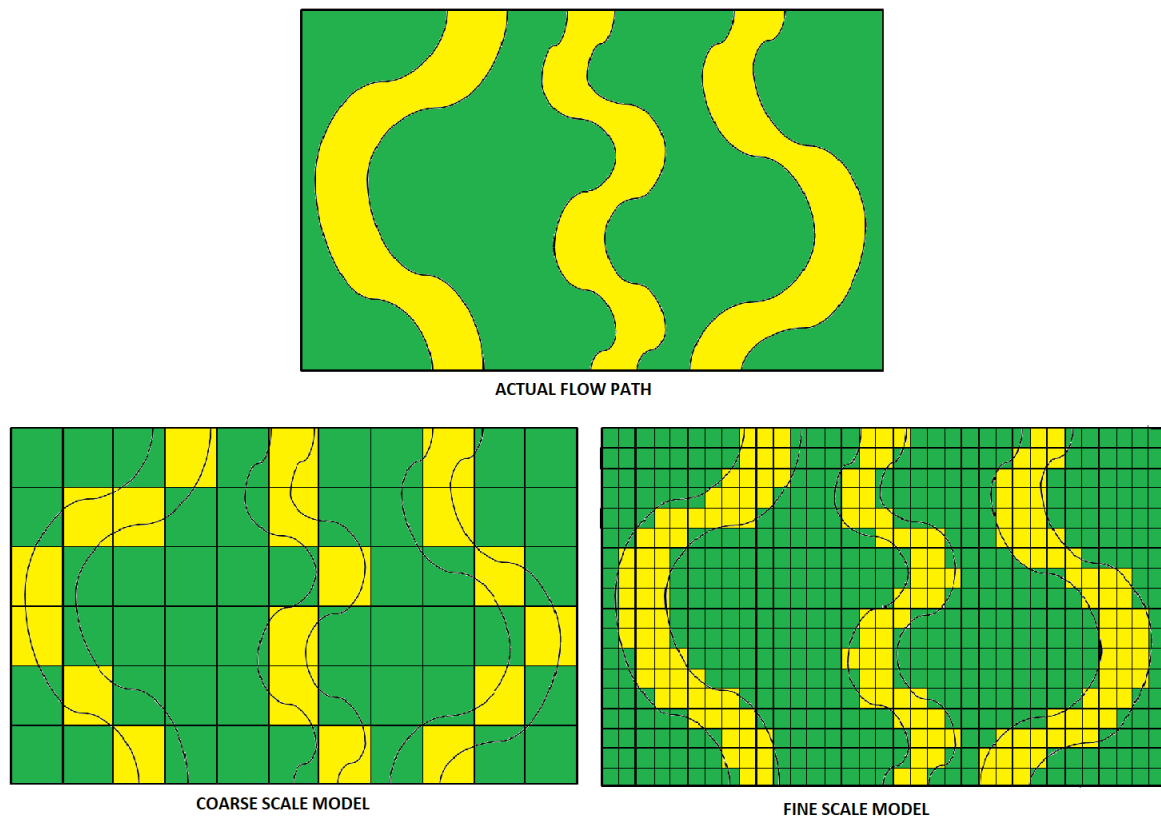
FigureA. 8: Flumy restricts its users from creating the same set of models for fine and coarse scales.

A1. 7: Visualization of Narrow channel bodies
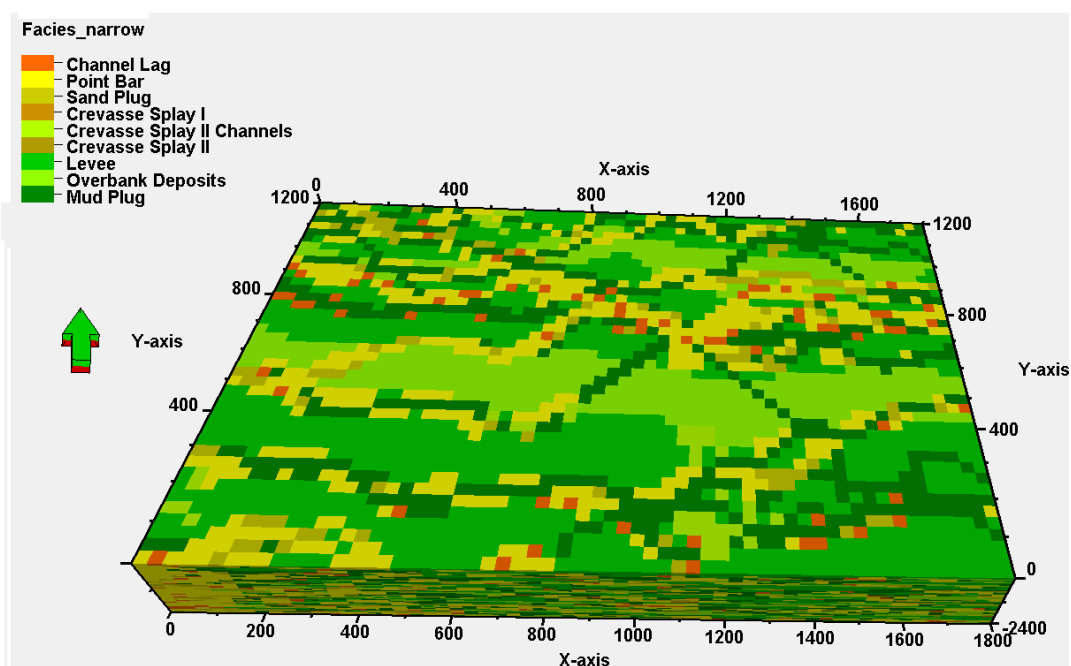
A1. 8 Upscaling Strategy (Discussion)
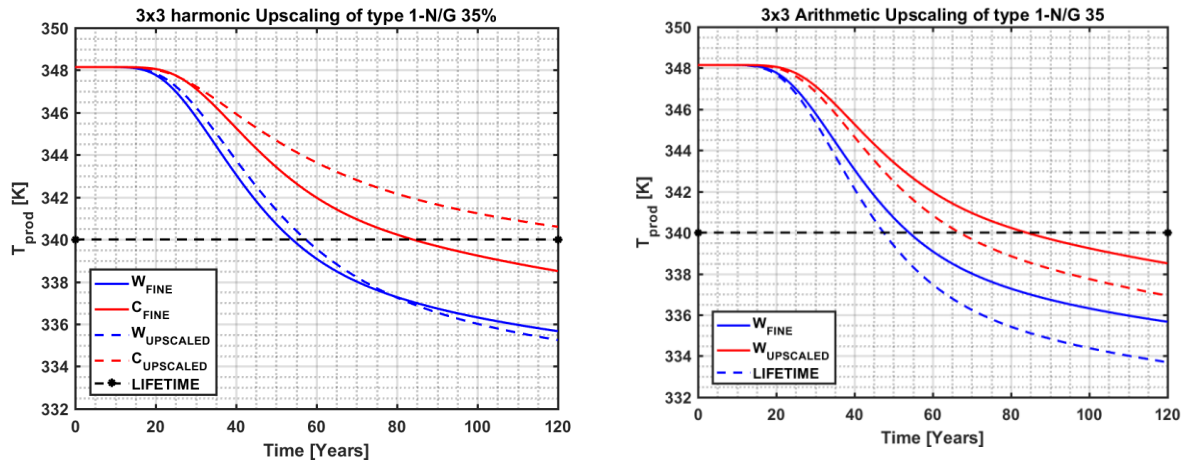
FigureA. 9: from left to right, harmonic and arithmetic averaging for type 1 model (3 x 3) upscaling

A1. 9 Thermal Breakthrough plots for fine and coarse models having N/G 65%
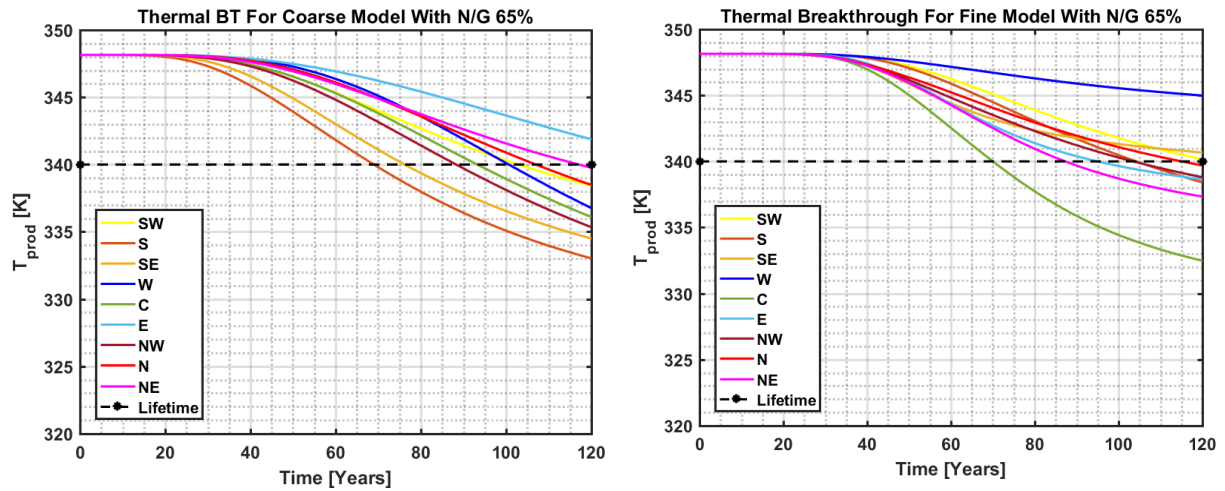
FigureA. 10: : Thermal BT for coarse and fine models with N/G 65% respectively

A1. 10 Dynamic model honoring geological deposition

So far, the models that were generated by Flumy were distinguished into sands and shales depending on the type of facies. The sand plugs, point bars, and channel lags were considered as sand bodies. They were populated with porosities in a random beta distribution fashion. This method of populating porosities is not representative of the spatial distribution of geological properties. Geostatistical and neural networks can be used as forecasting strategies of geological characteristics. (46) These techniques are considered to be very detailed and time-consuming and hence the application of such strategies lies beyond the scope of this thesis. However in order to honor the geological deposition, three sets of permeability values were assigned for sand plugs, point bars and channel lags correspondingly. The porosity values were then back-calculated using Eq. *3-1* and assigned. This way the model would have a more realistic flow path.

A. Flumy Facies Deposition (1-9)   B. Assuming Sands(1,2,3) and Shales(0)

C. Beta Distribution of Permeability (mD)

D. Geological Distribution of Permeability (mD)
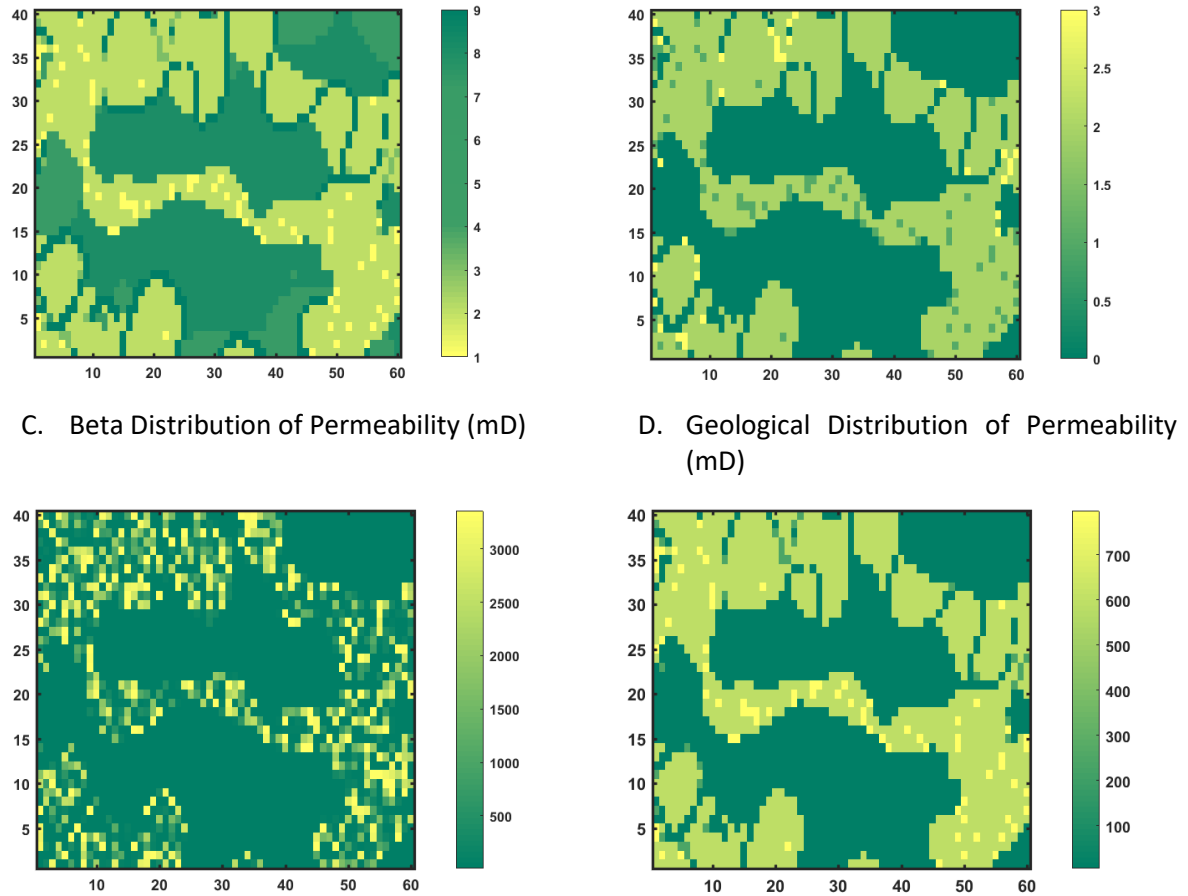
FigureA. 11 Permeability distribution in D seems to have a reasonable match with that of Flumy depositions

In **FigureA. 11,** a single layer of the 3D model was chosen for representation, 'A' represents the Flumy distribution of facies from 1-9, 'B' represents the model being generalized to sands (1-3) and shales (4-9 considered as 0 in the figure), 'C' represents the permeability distribution in the sand bodies using beta correlation. 'D' represents the distributions of permeability's honoring the geology. It's clearly evident that the distribution used while honoring the geological depositions (figure D) best represents the way in which Flumy generates the models (figure A).

Once the model honoring the geological depositions were created, the simulations were run at the very same doublet location as that of the Base case and the two results were analyzed. It can be observed that although there are variations in the breakthrough time between the two models the spread in the breakthrough is still evident, even in the model that honors the geological distributions.What we can infer from this is that the heterogeneity with the sand body isn't the reason for this huge spread between the breakthrough times, instead, it's the heterogeneity in the way in which the channels themselves deposit that cause these huge variations. A slight relocation of the wells from its original position would introduce an entirely new flow path for the fluids to travel, thereby resulting in a completely different behavior of the thermal breakthrough.

Thermal breakthrough for beta and geological distribution
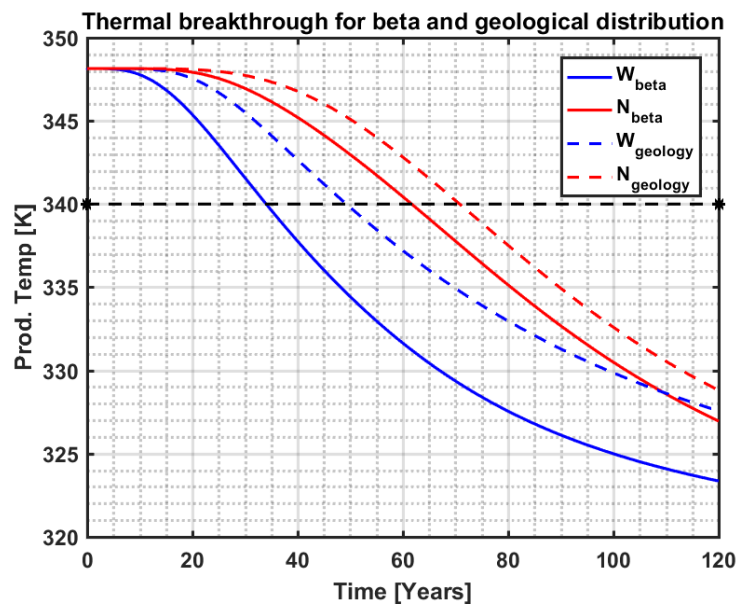
Base case– beta distribution [Permeability - mD]	
Sandstone	6-3500
Shale	5

Honoring Geology [Permeability –mD]	
Sand	245-800
shale	5

Base case [Years]	
Spread	28

Ignoring OB UB model [Years]	
Spread	21.5

FigureA. 12: Plot shows the variation in the BT trajectories from the base case with the model that honours the geology.

Comparison of the base case with the model that honours the geology

BIBLIOGRAPHY

1. *Global geothermal energy summit 2017 Retrieved from http://www.wplgroup.com/aci/even/global-geothermal-energy-summit/.* Amsterdam : s.n., 2017.

2. **Okandan, Ender.** *Geothermal Reservoir Engineering.* s.l. : Kluwer Academic Publishers, 1988.

3. **Saeid, S. Hicks, M. .** *Experimental and Numerical Study of Heat Flow under Low-Enthalpy Hydrothermal Conditions.* 2015.

4. *ROLE AND MANAGEMENT OF GEOTHERMAL REINJECTION.* **Axelsson, Gudni.** Santa Tecla, El Salvador : UNU-GTP and LaGeo, March, 2012.

5. *On the connectivity anisotropy in fluvial Hot Sedimentary Aquifers and its influence on geothermal doublet performance.* **Cees J.L.Willems, Hamidreza M.Nick, Marinus E.Donselaar, Gert JanWeltje, David F.Bruhn.** s.l. : Geothermics, 2017, Vol. 65.

6. *Effects of Density and Viscosity in Modeling Heat as a Groundwater Tracer.* **Zheng, Rui Ma and Chunmiao.** s.l. : Ground Water;48(3):380-9, 2010.

7. *Uncertainty analysis of thermo-hydro-mechanical coupled processes in heterogeneous porous media.* **Norihiro Watanabe, Wenqing Wang ,Christopher I. McDermott, Takeo Taniguchi, Olaf Kolditz.** s.l. : Comput Mech, 45:263–280, 2010.

8. *The geothermal project Den Haag: 3D numerical models for temperature prediction and reservoir simulation.* **Darius Mottaghya, Renate Pechniga, Christian Vogt.** s.l. : Geothermics 40(3) 199–210, 2010.

9. *Determination of optimum parameters of doublet system in a horizontally fractured geothermal reservoir.* **Thushan Chandrasiri Ekneligoda, Ki-Bok Min.** s.l. : Renewable Energy ,152-160, 2014, Vol. 65.

10. *Modeling contribution to risk assessment of thermal production power for geothermal reservoirs.* **Christian Vogt a, Katja Iwanowski-Strahser, Gabriele Marquart,Juliane Arnold, Darius Mottaghy, Renate Pechnig, Daniel Gnjezda, Christoph Clauser.** s.l. : Renewable Energy, 230-241, 2013, Vol. 53.

11. *An efficient computational model for deep low-enthalpy geothermal systems.* **Sanaz Saeid, Rafid Al-Khoury, Frans Barends.** s.l. : Computers & Geosciences, 400–409, 2013, Vol. 51.

12. *Numerical simulation of geothermal reservoirs for the sustainable design of energy plants: A review.* **Alessandro Franco, Maurizio Vaccaro.** s.l. : Renewable and Sustainable Energy Reviews 987–1002, 2014, Vol. 30.

13. *Lifetime optimization of low enthalpy geothermal doublets.* **J.P. Sauty, A.C. Gringarten, P.A. Landel, A. Menjoz.** s.l. : Advances in European geothermal research, Springer, Netherlands , pp. 706-719, 1980.

14. *Sensitivity analysis of low-temperature geothermal reservoirs: effect of reservoir parameters on the direct use of geothermal energy: Geothermal Resources Council Transactions.* **Madhur G. Bedre, Brian J. Anderson.** s.l. : Geothermal Resources Council 2012 annual meeting, 2010.

15. *Deep 3D thermal modelling for the city of Berlin (Germany).* **J. Sippel, S. Fuchs, M. Cacace, A. Braatz, O. Kastner, E. Huenges, et al.** s.l. : Environ Earth Sci, 70 , pp. 3545-3566, 2013, Vol. 8.

16. *A Geothermal Reservoir Simulator with AD-GPRS.* **Zhi Yang Wong, Roland Horne, Denis Voskov.** Melbourne, Australia : Proceedings World Geothermal Congress 2015 , 2015.

17. *A prototype design model for deep low-enthalpy hydrothermal systems.* **SanazSaeid, RafidAl-Khoury, Hamidreza M, Nick, Michael A.Hicks.** s.l. : Renewable Energy, 2015, Vol. 77.

18. *Operator-based Linearization for Modeling of Low-enthalpy Geothermal Processes.* **Mark Khait, Denis Voskov.** Stanford, California : Workshop on Geothermal Reservoir Engineering, 2016.

19. *Reservoir Geology and Geothermal Potential of the Delft Sandstone Member in the West.* **Marinus E. Donselaar, Remco M. Groenenberg, Douglas T. Gilding.** Melbourne, Australia : World Geothermal Congress 2015, 2015.

20. **Vondrak, A.G.** *(Bio-) stratigraphic correlation of geothermal aquifers in the West Netherlands Basin.* s.l. : Panterra Geoconsultants, 2016.

21. **WILLEMS, Cees.** *Doublet deployment strategies for geothermal Hot Sedimentary Aquifer exploitation.* s.l. : Ph.D Thesis, 2017.

22. **Wiggers, C.J.I.** *The Delft Sandstone in the West Netherlands Basin.* Delft : s.n., 2009.

23. *Influence of fluvial sandstone architecture on geothermal energy production.* **Cees J. L. Willems, Hamidreza M. Nick, Gert Jan Weltje,Donselaar, David. F. Bruhn.** Melbourne, Australia : World Geothermal Congress , 2015. 19-25.

24. *Tectonostratigraphy of the Nieuwerkerk Formation (Delfland subgroup), West Netherlands Basin.* **Jeremiah, Bryan DeVault and Jason.** 10, s.l. : AAPG Bulletin,, 2002, Vol. 86.

25. **Theo E. Wong, Dick A. J. Batjes.** *Geology of the Netherlands .* s.l. : Edita-the Publishing House of the Royal , 2008.

26. **Van Adrichem Boogaert, H. & Kouwe, W.** *Stratigraphic nomenclature of the Netherlands.* Haarlem : RDG and NOGEPA, 1993-1997.

27. *Fluvial sequence stratigraphy of Lower Cretaceous geothermal aquifers derived from palynological cutting analysis.* **Willems, C.J.L., Vondrak, A.,Munsterman, D.K., Donselaar, M.E., Mijnlieff.** s.l. : Unlocking the Energy Elephant: A SedHeat Workshop.

28. *Object-based modelling of avulsion-generated sandbody distributions and connectivity in a fluvial reservoir analogue of low to moderate net-to-gross ratio.* **Carlos A. Villamizar, Gary J. Hampson, Yvette S. Flood and Peter J. R. Fitch.** s.l. : Geological Society of London, 2015, Vol. 21. no. 4 249-270.

BIBLIOGRAPHY

29. *A three-dimensional numerical model of sediment transport, erosion and deposition within a network of channel belts, floodplain and hill slope: extrinsic and intrinsic controls on floodplain dynamics and alluvial architecture.* **Derek Karssenberg, John S. Bridge.** 6, s.l. : Sedimentology, 2008, Vol. 55. 1717–1745.

30. *IMPACT OF FLUVIAL SEDIMENTARY HETEROGENEITIES ON HEAT TRANSFER AT A GEOTHERMAL DOUBLET SCALE.* **Lopez, Virginie Hamm and Simon.** Stanford, California : Thirty-Seventh Workshop on Geothermal Reservoir Engineering, 2012. SGP-TR-194.

31. **David S. G. Thomas, Andrew S.** *The Dictionary of Physical Geography, Third Edition.* s.l. : Blackwell Publishing Ltd., 2000.

32. **Thonon, Ivo.** *Deposition of sediment and associated heavy metals on floodplains.* s.l. : Netherlands Geographical Studies, 2006.

33. **Lev Eppelbaum, Izzy Kutasov, Arkady Pilchin.** *Applied Geothermics.* s.l. : Springer Science & Business, 2014. 100-107.

34. *Geothermal Reservoir Simulation 1.Mathematical models for liquid- and vapour-dominated hydrothermal systems.* **Charkes R Faust, James W. Mercer.** Virginia : Water Resource research, 1979.

35. sourced from https://opentextbc.ca/chemistry/chapter/10-4-phase-diagrams/.

36. **Gries, Sebastian.** *System-AMG Approaches for Industrial Fully and Adaptive Implicit Oil Reservoir Simulations.* 2016.

37. **Denis Voskov, Yifan Zhou.** *AD-GPRS Stanford University's Automatic Differentiation based General Purpose Research Simulator user manual, website: http://pangea.stanford.edu/researchgroups/supri-b/.*

38. **Wong, Zhi Yang.** *A Geothermal Reservoir Simulator in AD-GPRS.* Stanford, California : s.n., June 2015.

39. *A New Approach for Residual and Jacobian Array Construction in Reservoir Simulators.* **K.T. Lim, D.J. Schiozer, Khalid Aziz.** 04, s.l. : Society of Petroleum Engineers, July 1995, Vol. 7.

40. *A Theoretical Analysis of Waterflooding Networks.* **Muskat, M. and Wyckoff.** 01, s.l. : Society of Petroleum Engineers, 1934, Vol. 107.

41. *Miscible WAG Simulations using streamlines.* **Marco R. Thiele, Rod P Batycky, L.Kent Thomas.** Germany : European conference on the mathematics of oil recovery, 2002.

42. [book auth.] Sourced from http://petrowiki.org/Streamline_simulation#cite_note-r10-10.

43. *Streamline-based simulation of solute transport.* **Martha J. Crane, Martin J. Blunt.** s.l. : WATER RESOURCES RESEARCH,, 1999, Vol. 35.

44. *Streamline Simulation.* **Thiele, Marco R.** Austri : 6th International Forum on Reservoir Simulation, 2001.

45. *The relation between well spacing and Net Present Value in fluvial Hot Sedimentary Aquifer geothermal doublets; a West Netherlands Basin case study.* **Willems, C.J.L., et al., et al.** Stanford, California : 41st Workshop on Geothermal Reservoir Engineering, 2016.

46. *3D Geological Modeling of Subsurface for Drilling Purposes Using Neural Networks and Fuzzy Logic.* **Alvaro Talavera, Vivian Marchesi,Débora Pilotto,Marcos Fonseca Alcure.** Goiania, Brazil : Rock Mechanics for Natural Resources and Infrastructure, 2014.

47. *A coupled local-global upscaling approach for simulating flow in highly heterogeneous formations.* **Y.Chen, L.J.Durlofsky, M.Gerritsen, X.H.Wen.** s.l. : Advances in water resource, 2003.